Towards Optimization of Tuned Mass Dampers in Suspended Bridges by Accounting for Non-Linear Behaviour

Auteur : Zeoli, Juliette
Promoteur(s) : Denoël, Vincent
Faculté : Faculté des Sciences appliquées
Diplôme : Master en ingénieur civil des constructions, à finalité spécialisée en "civil engineering"
Année académique : 2024-2025
URI/URL : http://hdl.handle.net/2268.2/23197

Master thesis presented in fulfillment of the requirements for the degree of Master in Civil Engineering

Towards Optimization of Tuned Mass Dampers in Suspended Bridges by Accounting for Non-Linear Behaviour

ZEOLI Juliette

Academic supervisor: Vincent Denoël
Jury members: Nenad Bijelić, Vincent de Ville de Goyet & François Rigo

Université de Liège - Faculty of Applied Sciences
Academic year 2024-2025

Contents

Abstract

This master thesis investigates the dynamic behaviour of suspended pedestrian bridges, with a focus on the non-linearities resulting from the quadratic dependency of cables stiffness to displacement, using the Victor-Neels bridge as a case study. A detailed numerical model was developed in the software `Finelg`, and was validated by an experimental campaign involving pedestrian induced vibrations. The results from the modal identification using COV-SSI method and the tension measurement in hangers provided meaningful information to refine the numerical model to replicate the real-life behaviour of the bridge as closely as possible.

Non-linear dynamic analyses, performed with sine sweep of varying amplitude, revealed a significant increase in structural stiffness beyond a certain excitation threshold, resulting in reduced displacement amplitude compared to the linear predictions as well as a frequency shift in the resonant frequency peak. Even though a linear analysis is conservative, it can lead to excessive displacement estimations, potentially resulting in unnecessary Tuned Mass Damper (TMD) installations or structural oversizing.

This work investigates the effectiveness of linear TMDs in linear and non-linear analyses. While TMDs tuned to the frequency resulting from the modal analysis were effective, their efficiency was increased by taking into account the frequency shift from the non-linear dynamic analyses. The results also showed that a comparable damping efficiency could be achieved with a lower-mass TMD, offering interesting perspective in terms of possible optimization. Other perspectives include the implementation of a non-linear TMD with an exponential damping force depending on the speed, to enhance performance to reduce the amplitudes of the peak response.

Keywords. Suspended footbridge, Non-linearity, Tuned Mass Damper, Finelg.

Acknowledgements

I would like to thank all the people who helped me make this work a reality.

First, I wish to express my sincere gratitude to my supervisor, Vincent Denoël for his guidance and time. I also thank François Rigo, Sébastien Hoffait and all the staff of V_2i for their warm welcome during the whole semester. I am especially grateful to François Rigo for his availability and insightful advice.

I would like to thank the members of the jury for taking the time to read and evaluate this thesis and more particularly, I would like to warmly thank Nenad Bijelić for giving me the opportunity to go further in this work with a PhD and Vincent de Ville de Goyet his valuable feedback, advice, and interest in my work.

I also wish to thank Greisch for letting me use their software. I am extremely grateful to Romain Bodson for all the time taken to help me with `Finelg` and to answer all my questions and to Mr. De Ville and Duchêne for their constructive feedback on my work.

I would like to express my gratitude to Lorenz Cornelissen from *Cornelissen + partners* for his availably and interest in my work and for providing me with the drawings and detailed information on the bridge.

Finally, I am especially thankful to my family and friends for their unwavering support and encouragement throughout this 5-year journey. Their enthusiasm and help during the experimental campaign meant a great deal to me. I am more grateful than words can express.

Acronyms

COV-SSI method Covariance-driven Stochastic Subspace Iteration method.

DOF Degree of freedom.

FE Finite Element.

FRF Frequency Response Function.

FT Fourier Transform.

MDOFs Multiple-Degree of Freedom System.

OSS Open-Spiral Strand.

PSD Power Spectral Density.

SDOFs Single-Degree of Freedom System.

SETRA Service d'Etude Technique des Routes et Autoroutes.

SLS Serviceability Limit State.

TMD Tuned Mass Damper.

1 Introduction

Progress in materials science and construction techniques has significantly expanded the possibilities in bridge engineering, enabling the design and realization of increasingly ambitious and complex structures. In the last fifty years, bridge construction has reached unprecedented lengths, largely due to the development of suspension bridges. Whereas earlier designs often solely relied on static analyses to assess the structural behaviour, history has shown that dynamic effects must not be overlooked. Infamous examples include the collapse of the Tacoma Narrows Bridge in the United States due to aeroelastic flutter (the wind matches the resonant frequency of the bridge and reinforces the vibrations), the excessive lateral vibrations observed during the inauguration of the Millennium Bridge in London caused by the synchronization of pedestrians and the wind-induced vibrations encountered during the construction of the Alconétar Bridge in Spain, causing early fatigue damages.

Nowadays, with the rise of long-spanned suspended bridges (Figure 1.1 (a)) and Himalayan footbridges for pedestrians (Figure 1.1 (b)), there is a clear tendency towards more flexible and lighter structures that are more prone to vibration. This typology is gaining popularity because it enables the crossing of large spans while maintaining a light, elegant appearance that integrates with the surrounding environment. Himalayan footbridges, in particular, are favoured for spanning large valleys or bodies of water in areas where nature is the main attraction and environmental integration is essential.

(a) Çanakkale Bridge, Türkiye: the longest suspended bridge in the world, with a span of 2023 m.

(b) Himalayan footbridge of the Drac, France, with a span of 220 m.

Figure 1.1: Example of two types of suspended bridges with a flexible structure.

Suspended bridges are distinct from other bridge types—such as arch bridges, beam bridges, and cable-stayed bridges—due to their main suspension cables. While most bridge types exhibit a linear behaviour under self-weight or loading, suspended bridges tend to behave non-linearly. This non-linear behaviour is the result of two important factors. First, the main suspension cables are not taut. They can naturally deform under their self-weight into a catenary, and into a parabola under external loads. The deformed shape is often a combination of both. As a reminder, the equation of a catenary is defined as:

$$y_c = a \cdot \cosh\left(\frac{x}{a}\right) = \frac{a}{2} \cdot \left(e^{x/a} + e^{-x/a}\right) \tag{1.1}$$

This equation, like the parabolic equation, is far from linear and results in a fundamentally different and more complex structural response. Second, all cables exhibit nonlinearity, particularly due to their tension-only behaviour. The cables do not resist compressive forces and only develop stiffness once tension is established. Furthermore, that stiffness is not constant: it evolves with the amount of tension in the cable. The more taut the cable, the larger its stiffness, introducing another non-linear behaviour in the system: when a load is imposed on a catenary-shaped cable, it deflects, and its stiffness increases progressively, slowing down the deflection process — a self-stiffening effect that characterizes non-linear structural behaviour.

In contrast, the cables in a cable-stayed bridge are taut, overall straight, and sag is avoided. They are directly connected to the deck of the bridge and pylon, resulting in small displacements under loading and almost no geometric non-linearity, as represented in Figure 1.2. The large initial stiffness and small displacements prevent extensive stiffness variation and facilitate a linear force-displacement relationship.

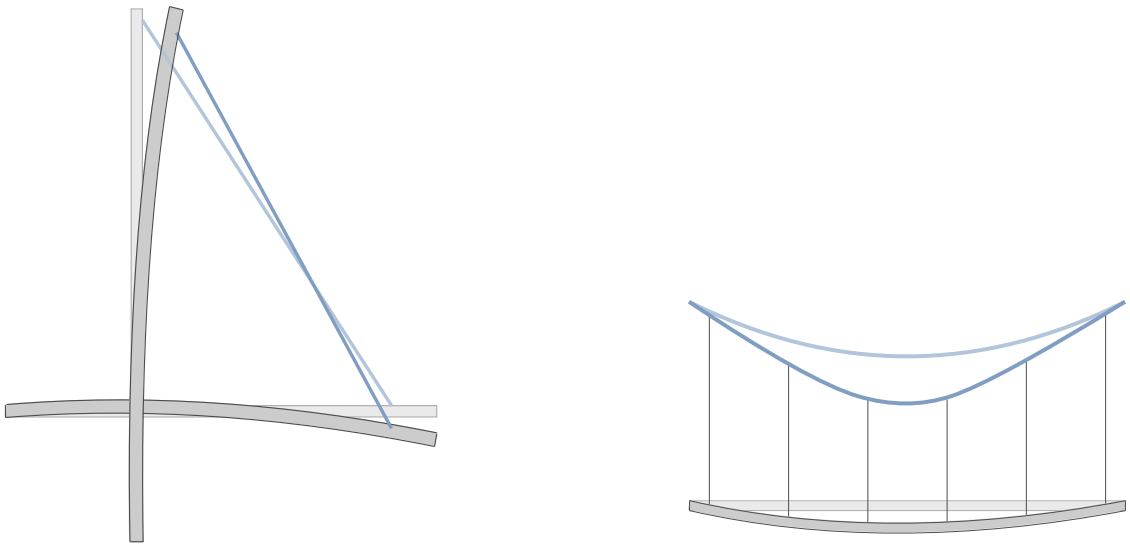

(a) Schematic of the deformation of the cable in a cable-stayed bridge.

(b) Schematic of the deformation of the suspension cable in a suspended bridge.

Figure 1.2: Schematic of the deformation of a cable when taut in a cable-stayed bridge and of a cable with initial deformation in a suspended bridge.

While stiffness variation can often be neglected under small displacements, especially in the case of low-amplitude dynamic loading, it becomes significant when larger forces are involved. Those forces induce larger displacements, especially near resonant frequencies. The dynamic response may be amplified, and the resulting stiffness variations can no longer be ignored. This highlights the importance of accounting for non-linear effects in the dynamic analysis of flexible suspended structures, especially under conditions where large vibrations may occur.

In addition to modifying the force–displacement relationship, non-linearities also significantly influence the dynamic characteristics of suspended structures, including their eigenfrequencies and mode shapes. Unlike linear systems, where these properties are fixed and independent of loading magnitude, non-linear systems exhibit a load-dependent stiffness, causing the natural frequencies to shift as the tension in the structure changes, for example under deformations due to self-weight. As a result, eigenfrequencies may increase or decrease depending on the specific deformation state, and mode shapes can also evolve. Moreover, the Frequency Response Function (FRF) of a non-linear system differs from the classical shape of a linear one. With a linear structure, the FRF exhibits sharp, well-defined resonance peaks at discrete

natural frequencies, as represented in Figure 1.3 (a). In contrast, a non-linear system often shows that the resonant frequency identified linearly is not the most amplified frequency, as there is a tendency towards broader and shifted resonance peaks showing that a range of frequencies, rather than a discrete frequency, can respond at high amplitude. This effect can be observed in Figure 1.3 (b).

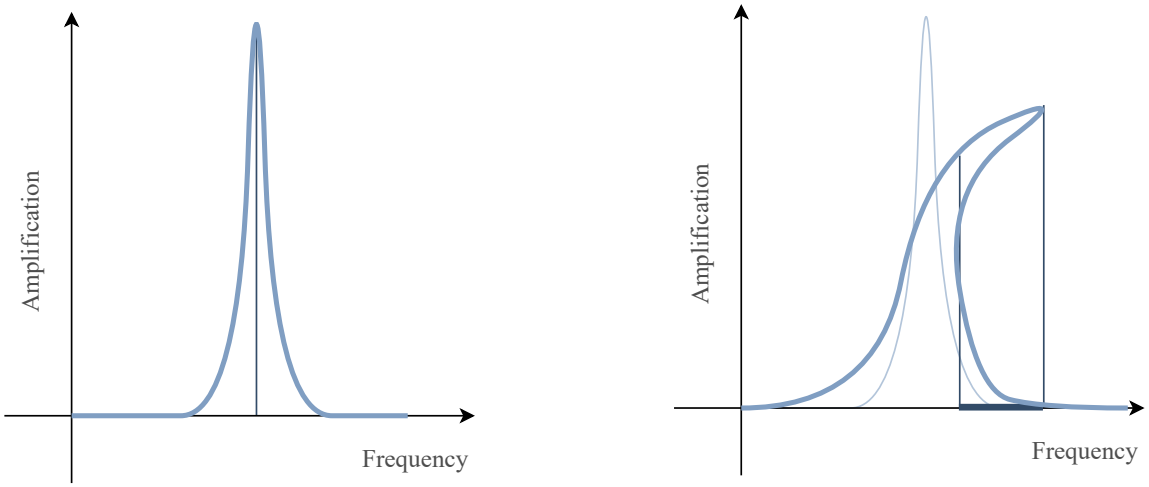

(a) Schematic of the shape of a linear FRF.

(b) Schematic of shape of a non-linear FRF.

Figure 1.3: Schematic representation the difference of shape and amplification between a linear and non linear frequency response function.

The variation of stiffness due to the amplitude of the force causes the system dynamic properties to evolve during oscillation. Consequently, the response amplitude does not scale linearly with the applied force. For example, doubling the excitation force does not simply double the amplitude of the response. Instead, amplification is non-linear, with lower amplification factors than the linear ones. The relation between force and displacement is impacted, as represented in Figure 1.4. These phenomena become

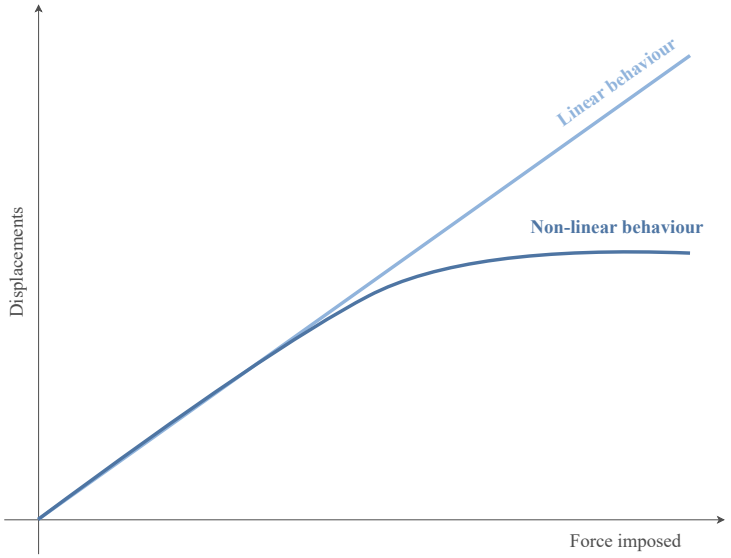

Figure 1.4: Schematic of the force-displacement relation for linear and non-linear structures.

particularly critical near resonant conditions, where even small variations in structural stiffness—caused by dynamic displacements—can either shift the system away from resonance or amplify the response in

unpredictable ways. In such contexts, non-linear effects can significantly alter the dynamic performance of slender structures like suspension bridges, especially under varying amplitude excitations. This thesis investigates the impact of these non-linearities on the dynamic behaviour of suspended footbridges. To this end, an existing suspended footbridge was selected as a case study, providing a realistic basis for both numerical and experimental analysis. A detailed finite element model of the bridge was developed using the software `Finelg`, incorporating its geometry, boundary conditions, and material properties as closely as possible.

The model was then validated through an experimental campaign conducted on the actual structure. This validation involved comparing the modal characteristics—such as natural frequencies, damping ratios, and mode shapes—of the numerical model with those measured in situ, ensuring that the simulation accurately reflects the bridge's real-life dynamic behaviour. Following the validation, the numerical model was used to perform a series of dynamic simulations, where the bridge was excited at varying force amplitudes. The objective of these simulations was to reconstruct the system's FRFs and to identify and quantify the non-linear dynamic effects arising at different excitation levels. This approach enables a deeper understanding of the role that structural non-linearities play in the overall dynamic response of suspended footbridges, especially under resonant or near-resonant conditions. Finally, the study evaluates the performance of the installed damping devices, passive tuned mass dampers. A particular focus will be brought on their efficiency in reducing vibrations and accelerations of the deck. The effect of non-linearities (frequency shift, ...) will be studied, as well as the influence of the damper-to-structure mass ratio. This analysis aims to assess the effectiveness of linear passive control strategies in reducing dynamic amplification in non-linear conditions.

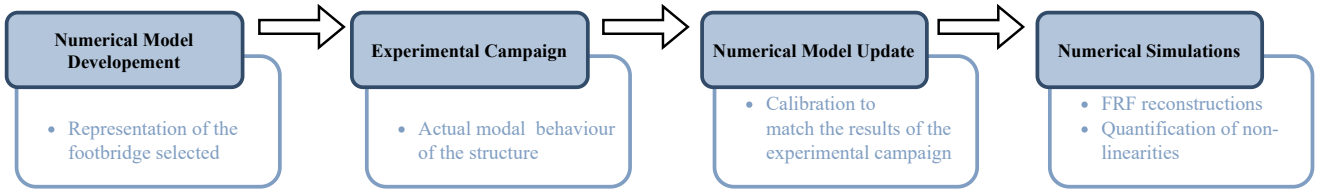

Figure 1.5: Process of the work.

2 Theoretical Background

2.1 Single Degree of Freedom Systems

Any mechanical system or structural component can be described in terms of mass, stiffness and damping. A Single-Degree of Freedom System (SDOFs) can be represented by a mass connected to a spring, where the spring represents the stiffness K of the system. To understand the motion of this system, it is assumed that movement occurs in only one direction (vertically, as represented in Figure 2.1). The free response is studied, i.e. the response in absence of external force, neglecting both the effect of gravity and the air resistance. An acceleration a_0 is given to the mass. The spring follows, at all times, the movement of the mass. The displacement of the system can be represented by an equation of motion. It is determined by using Newton's second law $F = m \cdot a$, the only force in the system being the restoring force of the spring, $F = -K \cdot x$ (from Hooke's Law).

$$M \cdot \ddot{x}(t) + K \cdot x(t) = P_0(t) = 0 \tag{2.1}$$

with $P_0(t)$, the eventual external forces applied to the system. As a free launch is studied here, $P_0(t) = 0$. This equation is an ordinary differential equation (ODE), where the form of the solution is assumed to be of the type: $x = C \cdot e^{r \cdot t}$, where C and r are constants.

$$\ddot{x}(t) + \frac{K}{M} \cdot x(t) = 0 \tag{2.2}$$

$$\ddot{x}(t) + \omega^2 \cdot x(t) = 0 \tag{2.3}$$

$$x = C \cdot e^{r \cdot t} : r^2 \cdot C \cdot e^{r \cdot t} + \omega^2 \cdot C \cdot e^{r \cdot t} = 0 \tag{2.4}$$

$$r^2 + \omega^2 = 0 \tag{2.5}$$

$$r = \pm\omega \cdot i \implies x = C \cdot e^{i \cdot \omega \cdot t} \tag{2.6}$$

The solution to that equation, in the case of a free response ($P_0(t) = 0$), is equal to its homogeneous solution. The exponential form of the solution can be represented by Euler's formula, or a sum between a sine and a cosine wave. Two of the three initial conditions are chosen to determine the constants: $\ddot{x}(0) = a_0$ & $\dot{x}(0) = 0$. The derivation of the expression of x enables to get $\ddot{x}(t)$ & $\dot{x}(t)$:

$$\ddot{x}(t) = -C_1 \cdot \omega^2 \cdot cos(\omega \cdot t) - C_2 \cdot \omega^2 \cdot sin(\omega \cdot t) \tag{2.7}$$

$$\dot{x}(t) = -C_1 \cdot \omega \cdot sin(\omega \cdot t) + C_2 \cdot \omega \cdot cos(\omega \cdot t) \tag{2.8}$$

$$\Rightarrow C_1 = -\frac{a_0}{\omega^2} \;\&\; C_2 = 0 \tag{2.9}$$

$$x(t) = -\frac{a_0}{\omega^2} \cdot \cos(\omega \cdot t) \tag{2.10}$$

Equation (2.10) states that the mass-spring system can be represented by a cosine wave, with an angular frequency ω equal to $\sqrt{K/M}$. This means that the stiffness impacts the period of the vibration of the system as well as its displacements. A stiff spring induces fast, low-amplitude displacements, whereas a loose spring triggers larger, slower displacements.

As the energy of the vibrations is not dissipated by any internal or external means, the displacement amplitude shall remain constant for an infinite amount of time. Of course, this is not representative of real-life motion where structures and materials dissipate energy in several ways (friction, thermal dissipation, ...), leading to amplitude-decreasing motion. This effect can be modelled by adding a positive damping element to equation (2.1): the dashpot. This expresses the damping of the system (C) or its dimensionless version, the damping ratio that will be explained later.

Without a dashpot to resist the spring displacement, the motion would continue indefinitely. Such a system is called undamped. In contrast, a damped system includes a dashpot, as illustrated in Figure 2.1(a). The displacement responses of systems with and without a dashpot are compared in Figure 2.1 (b). The damping effect is directly linked to the speed of motion of the system. When picturing a dashpot filled with liquid, the force needed to compress the fluid is smaller when pushing gently than when pushing all at once at a high speed. The equation of motion is thus modified, as well as the free response.

$$M \cdot \ddot{x}(t) + C \cdot \dot{x}(t) + K \cdot x(t) = P_0(t) = 0 \tag{2.11}$$

$$\frac{M}{M} \cdot \ddot{x}(t) + \frac{C}{M} \cdot \dot{x}(t) + \frac{K}{M} \cdot x(t) = \frac{P_0(t)}{M} = 0 \tag{2.12}$$

$$\ddot{x}(t) + 2 \cdot \xi \cdot \omega \cdot \dot{x}(t) + \omega^2 \cdot x(t) = \frac{P_0(t)}{M} = 0 \tag{2.13}$$

$$x(t) = -\frac{a_0}{\omega^2} \cdot \cos(\omega_d \cdot t) \cdot e^{-\xi \cdot \omega \cdot t} \tag{2.14}$$

With ω_d, the damped angular frequency, i.e. $\omega_d = \omega \cdot \sqrt{1 - \xi^2}$. As in civil engineering, ξ is comprised between 0.3 and 3 % at best, the damped angular frequency and the system angular frequency are often considered equal ($\omega_d \simeq \omega$). The equation of motion is still represented by a cosine, but now restricted by a **decreasing exponential**, as represented in Figure 2.1 (b).

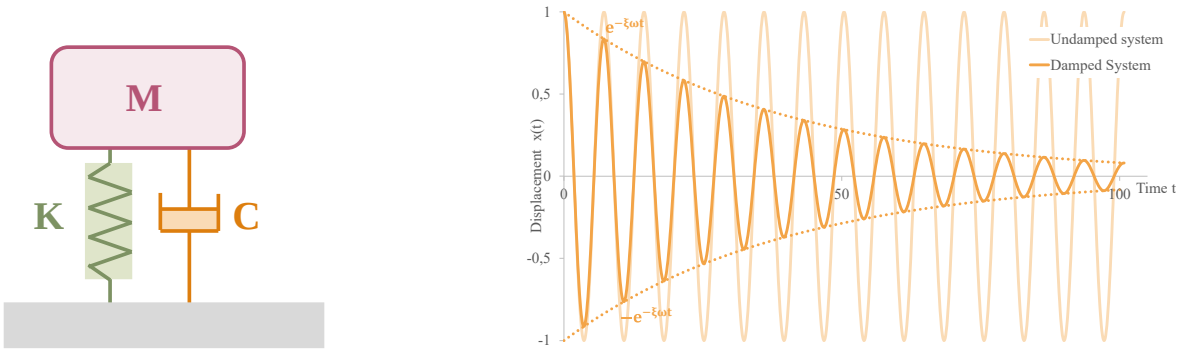

(a) Schematic representation of a damped system with a mass, a spring and a dashpot.

(b) Free displacement in time of a structure with damping (orange) and without damping (light orange).

Figure 2.1: Theoretical representation and behaviour of a damped structure.

An underdamped system, as represented in Figure 2.1, is damped by a dashpot represented by a viscosity that gradually reduces the amplitude of displacement until the mass returns to its initial position

again. The viscosity is computed through a damping coefficient c, that allows the structure to stabilize itself when triggered by a force or acceleration. The larger the damping ratio, the faster the system returns to its initial position. An overdamped system will prevent the system from vibrating at all, while a critically damped system possesses the exact amount of damping needed to cancel the effect of vibrations, as shown in Figure 2.2 (a). The damping is often expressed by a damping ratio, ξ, that is equal to the ratio of the damping coefficient of the structure and the critical damping coefficient, or by an estimation based on the free response of the structure:

$$\xi_{system} = \frac{c_{system}}{c_{critical}} \tag{2.15}$$

thus:

- Underdamped system: $\frac{c_{system}}{c_{critical}} < 1$
- Critically damped system: $\frac{c_{system}}{c_{critical}} = 1$
- Overdamped system: $\frac{c_{system}}{c_{critical}} > 1$

Damping values are typically positive. However, in rare cases, they become negative and contribute to the amplification of structural responses. This happens in some phenomena, such as aeroelastic flutter, the phenomenon that led to the collapse of the Tacoma Bridge. This phenomenon arises from an aeroelastic coupling between aerodynamic forces and the eigenmodes of the structure. The wind speed increases,the torsional frequency decreases while the vertical (bending) frequency increases. However, for a critical wind speed, both frequencies are equal and result in an amplification of the motion and dynamic instability. In civil engineering, the damping ratios are considered small (often between 1 and 2 %). This means that most structures are considered underdamped (light orange behaviour in Figure 2.2 (a)), and thus, prone to vibrating.

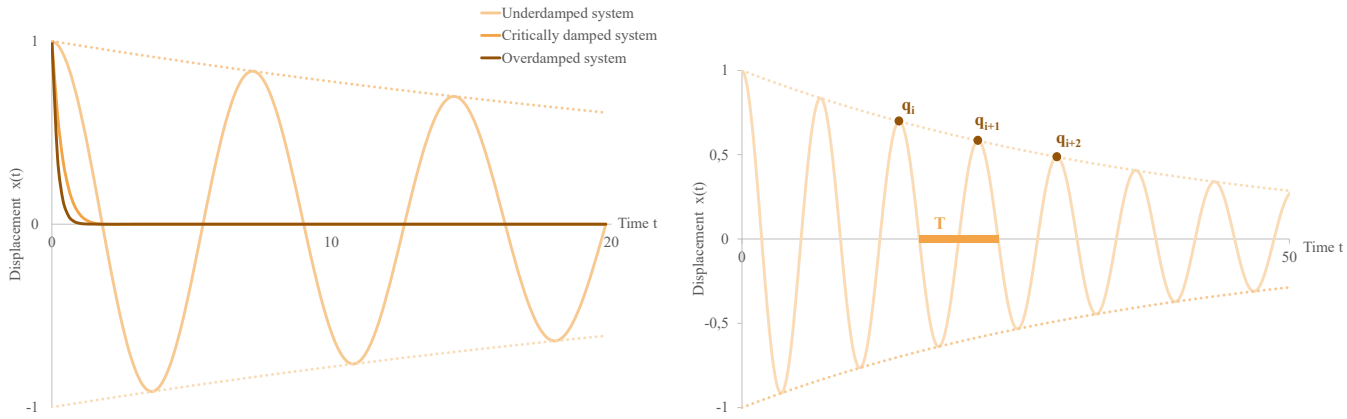

(a) Schematic representation of the increase of the damping coefficient on the displacement on a structure.

(b) Schematic representation of the logarithmic decrement method.

Figure 2.2: Theoretical representation and behaviour of a structure with varying damping ratios and representation of the computation of the logarithmic decrement method.

The free response decreases following an exponential envelope (i.e. $e^{-\xi \cdot \omega \cdot t}$). It is thus possible to compute the damping ratio of the structure based solely on that envelope. The decreasing exponential suggests that the displacement theoretically never reaches 0. However, with the logarithmic decrement method, it is possible to compute the time at which the response of the system is considered negligible

with respect to the initial displacement. The main variables of the method are schematically represented in Figure 2.2 (b).

$$for\ \xi\ = << :\ \xi = \frac{\ln(q_i)}{\ln(q_{i+n})} \cdot \frac{1}{2 \cdot \pi \cdot n} \tag{2.16}$$

$$\&\ t_R = \frac{T}{2 \cdot \xi} = \frac{\pi}{\omega \cdot \xi} \tag{2.17}$$

This equation can also be used to compute the time of settlement, t_R, i.e. the time taken by a structure excited by a harmonic loading to reach its full displacement amplitude. This specific time period is a transient frame where the effects of the excitation aren't fully developed.

Damping can be aerodynamic, structural, or external.

- **Aerodynamic**: activated by friction between the structure and air
- **Structural**: depending on the type of material or joint (ex: a bolted joint dissipates more energy than a welded joint)
- **External**: additional damping supplied by an another system, such as a Tuned Mass Damper (TMD).

2.2 Multiple Degree of Freedom System

Discrete system

A Multiple-Degree of Freedom System (MDOFs) can be discrete or continuous. A discrete system has a limited number of Degree of freedom (DOF), whereas a continuous system has an infinite number of DOF and must be discretized. A good example of a discrete system is a SDOF, damped by TMD.

A TMD is a device characterised by its mass M* (often 10 % of the mass of the structure that needs to be damped), a spring K* and a dashpot C*. It is used to damp the vibrations of a structure when they induce large displacements or accelerations and are likely to damage it or cause discomfort to the users.

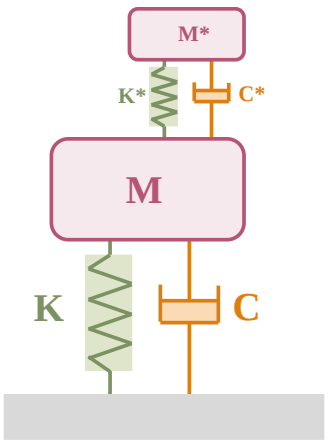

(a) Schematic representation of a system damped by a TMD.

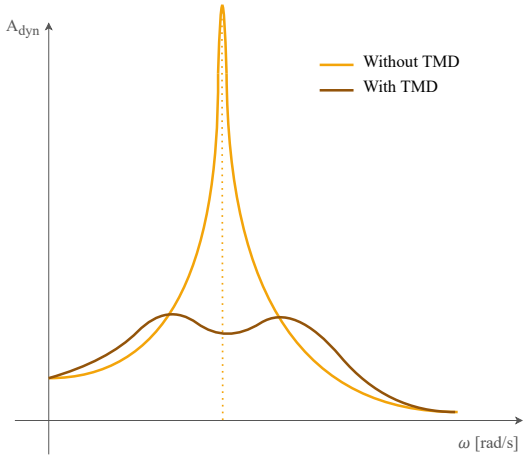

(b) Dynamic amplification of the structure: in orange - without TMD & in dark orange - with TMD.

Figure 2.3: Theoretical representation and behaviour of a damped structure.

The TMD is designed to have the same eigenfrequency as the structure, i.e. for a SDOF system, $\omega = \sqrt{K/M} = \sqrt{K^*/M^*}$. It splits the resonance frequency peak of the frequency into two separate peaks

with a significantly reduced dynamic amplification. Adding a TMD amounts to adding a degree of freedom to the structure with an opposing displacement, resulting in a new configuration of amplification around the targeted frequency. Figure 2.3 represents the effect of the TMD.

The equation of motion for a SDOF system can be transposed to a MDOF system using mass, stiffness and damping matrices instead of single values. The matrices are defined based on the number n of DOF (n x n) and the interaction of each DOF with the others. For example, for a 3-DOF system, as represented in Figure 2.4, the equation of motion for a mass-spring system can be written into matrices, summing up the interaction at the interfaces between the masses m_1, m_2 and m_3 for each translation x_1, x_2 and x_3.

$$\mathbf{M} \cdot \underline{\ddot{x}}(t) + \mathbf{K} \cdot \underline{x}(t) = \underline{p}(t) \tag{2.18}$$

$$\begin{pmatrix} m_1 & 0 & 0 \\ 0 & m_2 & 0 \\ 0 & 0 & m_3 \end{pmatrix} \cdot \begin{pmatrix} \ddot{x}_1 \\ \ddot{x}_2 \\ \ddot{x}_3 \end{pmatrix} \begin{pmatrix} k_1 + k_2 & -k_2 & 0 \\ -k_2 & k_2 + k_3 & -k_3 \\ 0 & -k_3 & k_3 \end{pmatrix} \begin{pmatrix} x_1 \\ x_2 \\ x_3 \end{pmatrix} = \begin{pmatrix} p_1 \\ p_2 \\ p_3 \end{pmatrix} \tag{2.19}$$

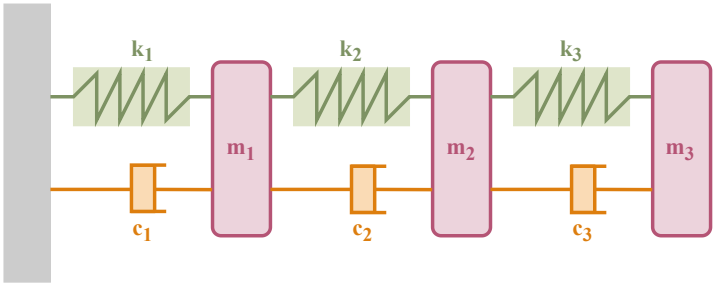

Figure 2.4: Schematic representation of a 3-DOF discrete system.

This equation can be used to compute the eigenfrequencies matrix ($\mathbf{\Omega}$) and eigenvectors matrix ($\mathbf{\Phi}$). It is then possible to take action to avoid triggering these critical modes or, if unavoidable, to reduce their impact on the structure, with the help of a TMD, for example. From the equation (2.18), with $\underline{p}(t) = \underline{0}$, the solution can be assumed in the form: $\underline{x}(t) = \phi \cdot e^{i \cdot \omega \cdot t}$, where ϕ is the mode shape vector, or eigenvector.

$$\underline{x}(t) = \phi \cdot e^{i \cdot \omega \cdot t} \tag{2.20}$$

$$\underline{\ddot{x}}(t) = -\omega^2 \cdot \phi \cdot e^{i \cdot \omega \cdot t} \tag{2.21}$$

$$\mathbf{M} \cdot \left(\omega^2 \cdot \phi \cdot e^{i \cdot \omega \cdot t}\right) + \mathbf{K} \cdot \left(\phi \cdot e^{i \cdot \omega \cdot t}\right) = \underline{0} \tag{2.22}$$

$$\left(\mathbf{K} - \omega^2 \cdot \mathbf{M}\right) \cdot \phi = \underline{0} \tag{2.23}$$

$$\det(\mathbf{K} - \omega^2 \cdot \mathbf{M}) = 0 \tag{2.24}$$

with ω^2, the vector of the squared eigenfrequencies and ϕ, the matrix of eigenmodes. To better understand the behaviour of the structure, damping can be added to the equation of motion in the same way as the other matrices seen previously. Nevertheless, determining the damping of a structure is complex, and often impossible without experimental testing. The matrix of damping can be replaced by a combination of the mass and the stiffness matrices, called the *proportional damping* matrix or *Rayleigh damping* matrix, as represented in Figure 2.5.

$$\mathbf{M} \cdot \ddot{\underline{x}}(t) + \mathbf{C} \cdot \dot{\underline{x}}(t) + \mathbf{K} \cdot \underline{x}(t) = \underline{p}(t) \tag{2.25}$$

$$\text{where} \quad \mathbf{C} = \alpha \cdot \mathbf{M} + \beta \cdot \mathbf{K} \tag{2.26}$$

$$\xi_i = \frac{C_{i,i}}{2 \cdot M_{i,i} \cdot \omega_i} = \frac{\alpha \cdot M_{i,i} + \beta \cdot K_{i,i}}{2 \cdot M_{i,i} \cdot \omega_i} \tag{2.27}$$

$$\Rightarrow \xi_i = \frac{\alpha}{2 \cdot \omega_i} + \frac{\beta \cdot \omega_i}{2} \tag{2.28}$$

As equation (2.28) shows, each frequency has its own combination of α and β. To simplify the calculations, two eigenfrequencies of the system are usually chosen. The fundamental frequency (deformation following a half sine wave), and the highest frequency considered. Based on those, the coefficients are defined with the assumption that $\xi_i = \xi_j$, a hypothesis often used in civil engineering, as the frequency range of interest is relatively narrow and the damping ratios are assumed to be similar across modes.

$$\begin{cases} \xi_i = \frac{\alpha}{2 \cdot \omega_i} + \frac{\beta \cdot \omega_i}{2} \\ \xi_j = \frac{\alpha}{2 \cdot \omega_j} + \frac{\beta \cdot \omega_j}{2} \end{cases} \Rightarrow \begin{cases} \alpha = \frac{2 \cdot \omega_i \cdot \omega_j}{\omega_i^2 - \omega_j^2} \cdot (\xi_j \cdot \omega_i + \xi_i \cdot \omega_j) = \frac{2 \cdot \omega_i \cdot \omega_j}{\omega_i^2 - \omega_j^2} \cdot \xi_i \cdot (\omega_i + \omega_j) \\ \beta = \frac{2 \cdot \omega_i \cdot \omega_j}{\omega_i^2 - \omega_j^2} \cdot (\frac{\xi_i}{\omega_j} - \frac{\xi_j}{\omega_i}) = \frac{2 \cdot \omega_i \cdot \omega_j}{\omega_i^2 - \omega_j^2} \cdot \xi_i \cdot (\frac{1}{\omega_j} - \frac{1}{\omega_i}) \end{cases} \tag{2.29}$$

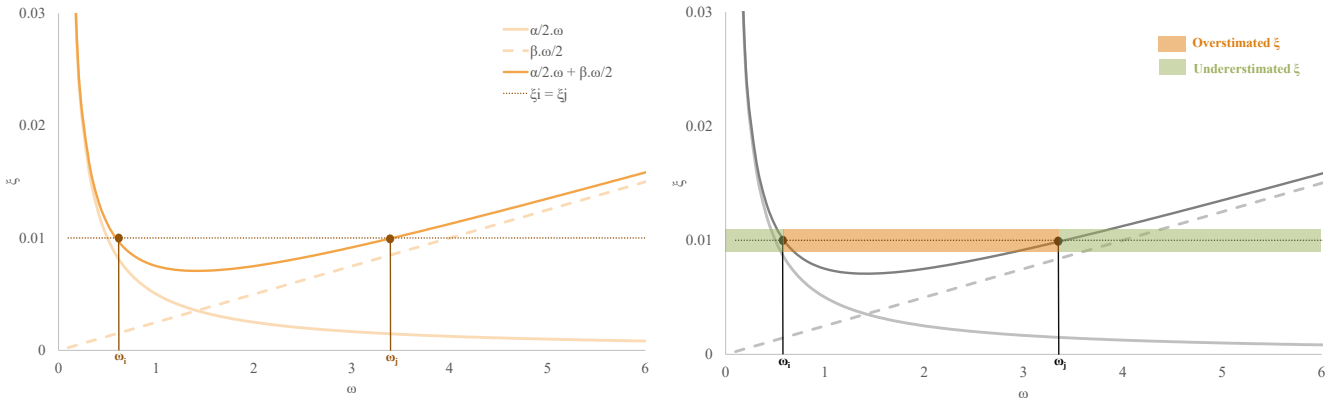

Figure 2.5: Theoretical representation of the Rayleigh damping function.

As seen in Figure 2.5, this combination of mass and stiffness matrix overestimates the damping in the range of frequencies studied. However, as the damping is difficult to quantify, it is possible to assume that some damping means are not taken into account and thus, the damping can be safely approximated by using Rayleigh's method. This method is proven to be accurate while greatly simplifying the equation system as well as the computations.

Continuous system

In real life, most of the systems are continuous and possess an infinity of DOFs. The equation of movement is not written in matrix form anymore. They have to be re-written in continuous form. By doing the shear equilibrium of an element of a clamped beam, free to deform in only one direction, only taking stiffness and mass into account (see Figure 2.6): With μ, the linear mass and EI, the bending stiffness of the beam:

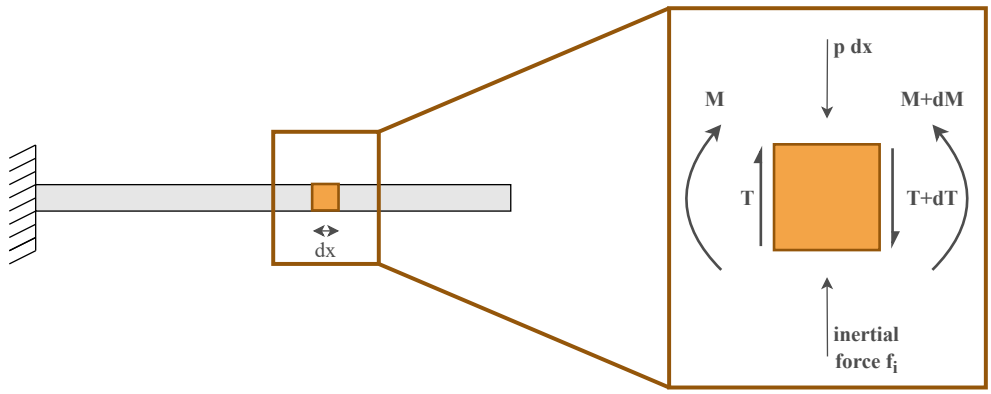

Figure 2.6: Example of a continuous system with an infinity of degrees of freedom.

$$\sum F = f_i \cdot dx + T + dT = T + p \cdot dx \tag{2.30}$$

$$f_i \cdot dx + dT = p(x,t) \cdot dx \tag{2.31}$$

$$\text{with:} \quad f_i = \mu \cdot \frac{\partial v(x,t)}{\partial t} \tag{2.32}$$

$$\sum M_{around\ CG} : M + dM = T \cdot \frac{dx}{2} + T \cdot \frac{dx}{2} + M \tag{2.33}$$

$$\Rightarrow T = \frac{dM}{dx} \rightarrow T = \frac{\partial M}{\partial x} = \frac{\partial}{\partial x} \cdot \left(-EI \cdot \frac{\partial^2 v}{\partial x^2} \right) \tag{2.34}$$

$$\mu \cdot \frac{\partial v(x,t)}{\partial t} + \frac{\partial^2}{\partial x^2} \cdot \left(-EI \cdot \frac{\partial^2 v(x,t)}{\partial x^2} \right) = p(x,t) \tag{2.35}$$

The analytical resolution of that equation is only possible for simple systems. Most of the real-life systems are complex to compute because they have an infinite number of DOFs. Simplification and discretisation are thus needed, with the help of approximations or numerical methods. The finite element method (FEM) disaggregates complex, continuous systems with an infinite number of DOFs into several discrete elements with a defined number of DOFS. The equation becomes matrix-based again, as seen before with discrete MDOFs system.

$$\mu \cdot \frac{\partial v(x,t)}{\partial t} + \frac{\partial^2}{\partial x^2} \cdot \left(-EI \cdot \frac{\partial^2 v(x,t)}{\partial x^2} \right) = p(x,t) \tag{2.36}$$

$$\Rightarrow \mathbf{M}\underline{\ddot{x}}(t) + \mathbf{K}\underline{x}(t) + \underline{p}(t) \tag{2.37}$$

$\mathbf{M} \cdot \underline{\ddot{x}}(t)$ represents the inertial forces, while $\mathbf{K} \cdot \underline{x}(t)$ represents the internal forces. This can be represented in a finite element base, which is the baseline of the finite element method software used to build the numerical model of this thesis.

Internal forces

$$\mathbf{K} \cdot \underline{x}(t) + \underline{p}(t) \tag{2.38}$$

$$\text{with} \quad K_{i,j} = \int_0^\ell \Psi_i''(x) \cdot EI \cdot \Psi_j''(x)\, dx \tag{2.39}$$

$$p_i = \int_0^\ell p_i \cdot \Psi_i\, dx \tag{2.40}$$

with $K_{i,j}$, the reaction at DOF i, for a unit displacement imposed at DOF j, while all other DOF are blocked, and p_i, the energetically equivalent force applied at DOF i. Ψ_i represents the **interpolation function**, which can be described as the evolution of the deformation resulting at a DOF i for a unit displacement or rotation. The most common interpolation function in structural analysis is a Hermite polynomial, a polynomial of degree 3. Those polynomials vary based on the triggered DOF and on the support conditions of each element. They are represented in Figure 2.7.

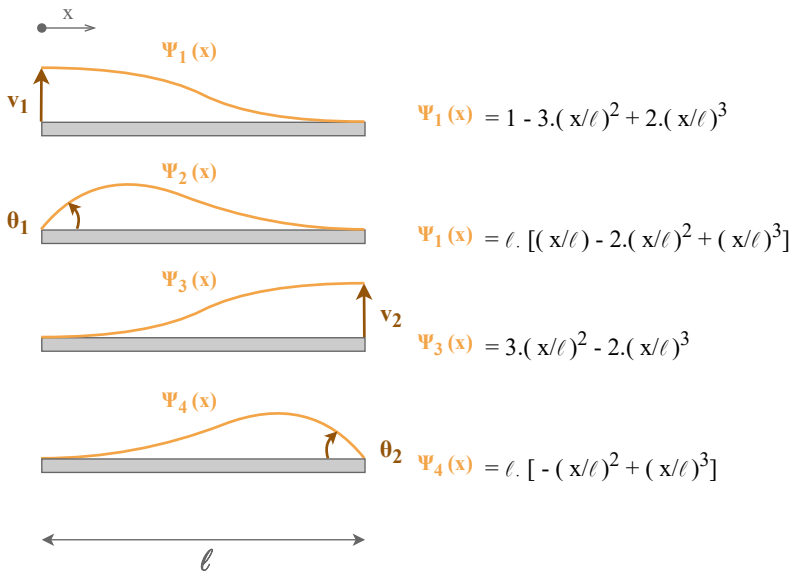

Figure 2.7: Interpolation functions based on the triggered DOF: Hermite polynomials.

Usually, as seen in Figure 2.7 above, there are 2 DOFs defined per node: one translation and one rotation. For a beam of length ℓ, the stiffness matrix is a 4x4 symmetrical matrix:

$$\mathbf{F}_{internal} = \mathbf{K}_e \cdot \underline{x}_e = \frac{EI}{\ell^3} \cdot \begin{bmatrix} 12 & 6\ell & -12 & 6\ell \\ 6\ell & 4\ell^2 & -6\ell & 2\ell^2 \\ -12 & -6\ell & 12 & 2\ell^2 \\ 6\ell & 2\ell^2 & 2\ell^2 & 4\ell^2 \end{bmatrix} \cdot \begin{bmatrix} v_1 \\ \theta_1 \\ v_2 \\ \theta_2 \end{bmatrix} \tag{2.41}$$

This matrix can be defined for each node of the system. Then, all the stiffness matrices are assembled together and form the full stiffness matrix of the system. For example, in Figure 2.8, for a linear beam, that can only translate in one direction:

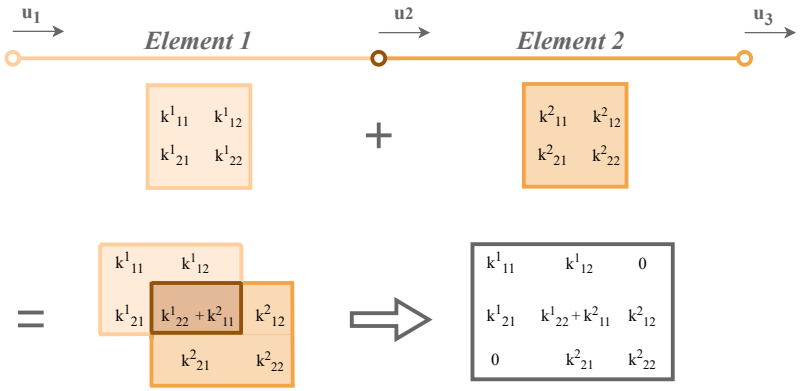

Figure 2.8: Example of an assembly of matrices in the case of a beam in translation composed of two elements.

Inertial forces

The mass-matrix has to be built in order to define the inertial forces. Two options can be considered:

1. The consistent mass matrix:
   The mass is considered to be spread evenly over the whole length of the element, so that the **M** matrix is defined in the same way as the stiffness matrix and takes into account the interaction between the DOF.

$$\mathbf{F}_{inertial} = \mathbf{M}_e \cdot \underline{\ddot{x}}_e = \int_0^\ell f_i(x,t) \cdot \Psi_i(x) dx \tag{2.42}$$

   with f_i, the inertial force per unit of length defined according to the second derivative of the deformed shape and μ, the mass per unit of length, i.e.:

$$f_i = \mu \cdot \ddot{v}(x,t) \tag{2.43}$$

$$F_i = \mu \cdot \int_0^\ell \left(\Psi_1(x) \cdot \ddot{v}_1 + \Psi_2(x) \cdot \ddot{\theta}_1 + \Psi_3(x) \cdot \ddot{v}_2 + \Psi_4(x) \cdot \ddot{\theta}_2 \right) \cdot \Psi_i \, dx \tag{2.44}$$

$$\tag{2.45}$$

   this leads to the mass matrix:

$$\mathbf{M} = \int_0^\ell \mu \cdot \Psi_i(x) \cdot \Psi_j(x) \, dx \tag{2.46}$$

   The interpolation functions Ψ_i and Ψ_j are the same as for the stiffness matrix (Hermite polynomials). For a beam of length ℓ, The final mass matrix is a 4x4 symmetrical matrix:

$$\mathbf{F}_{inertial} = \mathbf{M}_e \cdot \underline{\ddot{x}}_e = \frac{\mu \cdot \ell}{420} \cdot \begin{bmatrix} 156 & 22\ell & 54 & -13\ell \\ 22\ell & 4\ell^2 & 13\ell & -2\ell^2 \\ 54 & 13\ell & 156 & -22\ell \\ -13\ell & -3\ell^2 & -22\ell & 4\ell^2 \end{bmatrix} \cdot \begin{bmatrix} \ddot{v}_1 \\ \ddot{\theta}_1 \\ \ddot{v}_2 \\ \ddot{\theta}_2 \end{bmatrix} \tag{2.47}$$

2. Lumped mass model:
   The mass is considered lumped, meaning it's concentrated at both ends of the beams. The interpolation functions are not polynomials anymore, but constant as represented in Figure 2.9. As no interaction is considered between the DOFs, the mass matrix is greatly simplified and becomes:

$$\mathbf{M}_{e,lumped} = \begin{bmatrix} \mu\frac{\ell}{2} & 0 & 0 & 0 \\ 0 & 0 & 0 & 0 \\ 0 & 0 & \mu\frac{\ell}{2} & 0 \\ 0 & 0 & 0 & 0 \end{bmatrix} \tag{2.48}$$

   Such a matrix is interesting in terms of computation time and simplicity of calculation. However, the approximations are quite important. To minimize the error in a Finite Element (FE) model, the number of elements has to be increased. The choice of model is a trade-off between accuracy and ease of computation. For a model computed by hand, a lumped mass model is preferred, whereas for a FE software as the one used in this thesis, the consistent mass matrix will usually be favoured.

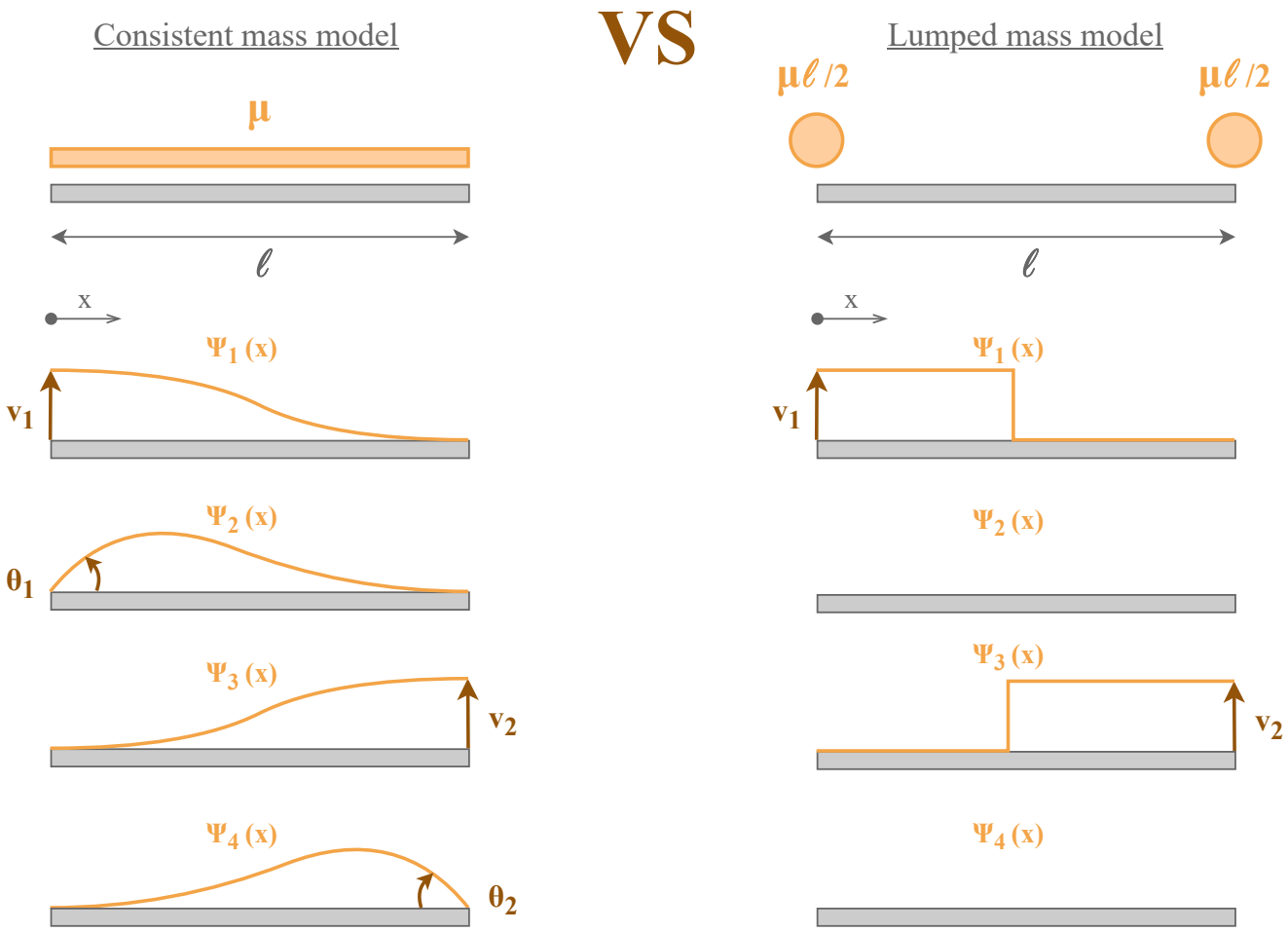

Figure 2.9: Consistent versus lumped mass model, with μ, the linear mass, and Ψ, the interpolation functions.

Damping forces

The damping forces can be taken into account to represent the real structure. The matrix is often constructed by taking a combination of the mass and stiffness, following Rayleigh damping matrix (see Figure 2.5), with the possibility of adding extra-damping at a specific node, if connected to a TMD. The damping forces are defined as follows:

$$\mathbf{F}_d = \int_0^\ell f_d(x,t) \cdot \Psi_i(x)\, dx \tag{2.49}$$

$$\mathbf{F}_d = \int_0^\ell c(x) \cdot \left(\Psi_1(x) \cdot \dot{v}_1 + \Psi_2(x) \cdot \dot{\theta}_1 + \Psi_3(x) \cdot \dot{v}_2 + \Psi_4(x) \cdot \dot{\theta}_2\right) \cdot \Psi_i\, dx \tag{2.50}$$

$$\tag{2.51}$$

The expression of the damping force is similar to those of the inertial and internal forces. This similarity allows to express $c(x)$ as a combination of the mass and rigidity, as seen before in Rayleigh damping, simplifying the expression of the equation of motion, as well as the computations. Once the matrices are built, the equation of motion has to be solved for each time step of the resolution.

2.3 Time Step Resolution: Newmark Method

The program selected for this thesis, `Finelg`, developed by *Greisch*, uses the Newmark method to solve the equation of motion of the system. This method is an implicit integration method, meaning it requires several iterations inside a time step to solve the equation of motion in that time step. The method is based on the estimation of the derivative of the system to solve the equation of motion:

$$\text{if } f(y,t) = \frac{dy}{dt} \tag{2.52}$$

$$y_{t+\Delta t} = f(y_{t+\Delta t}, y_t, y_{t-\Delta t}) \tag{2.53}$$

As the displacement y at $t + \Delta t$ depends on itself, an iterative process is necessary to find the solution of the equation of motion at that time step. The method used is based on an approximation of the **integral**, as represented in Figure 2.10.

$$y_{t+\Delta_t} = \int_0^{t+\Delta t} f(y,t)\, dt = y_t + \frac{f(y_{t+\Delta t}, t+\Delta_t) + f(y_t, t)}{2} \cdot \Delta t \tag{2.54}$$

The equation to solve is the equation of motion, where the displacement x(t) is unknown. It is possible to

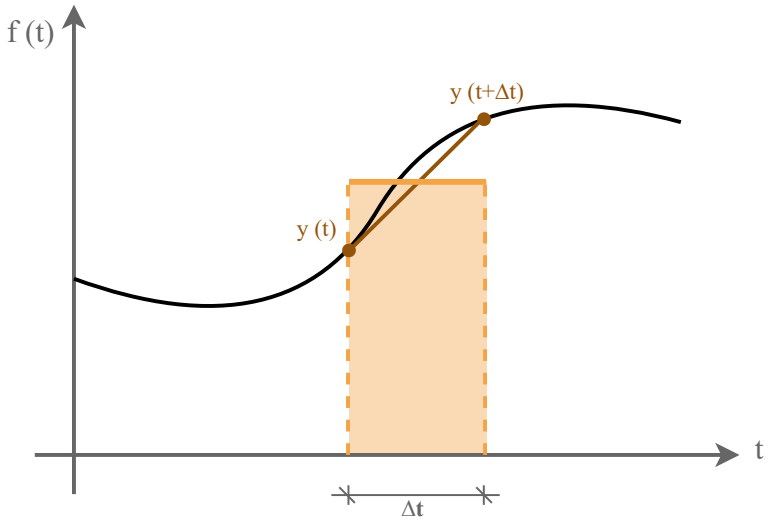

Figure 2.10: Representation of the linear approximation of the integral used in Newmark method.

particularize the general equation as:

$$m \cdot \ddot{x}(t) + c \cdot \dot{x}(t) + k \cdot x(t) = p(t) \tag{2.55}$$

The displacement and speed can be approximated by:

$$\dot{x}_{t+\Delta t} = \dot{x}_t + \int_t^{t+\Delta_t} \ddot{x}(t)\, dt \tag{2.56}$$

$$x_{t+\Delta t} = x_t + \int_t^{t+\Delta_t} \dot{x}(t)\, dt \tag{2.57}$$

Assuming the values in t are all known and that acceleration is constant between t and $t + \Delta t$ (see Figure 2.10):

$$\forall\, \tau \in [0\,;\, \Delta t]\ :\ \ddot{x}(t+\tau) = \frac{\ddot{x}_t + \ddot{x}_{t+\Delta t}}{2} \tag{2.58}$$

As $\ddot{x}_{t+\Delta t}$ is unknown:

$$\dot{x}(t+\tau) = \dot{x}_t + \frac{\ddot{x}_t + \ddot{x}_{t+\Delta t}}{2} \cdot \tau \tag{2.59}$$

$$x(t+\tau) = x_t + \dot{x}_t \cdot \tau + \frac{\ddot{x}_t + \ddot{x}_{t+\Delta t}}{2} \cdot \frac{\tau^2}{2} \tag{2.60}$$

$$\tag{2.61}$$

At the end of the time step: $\tau = \Delta t$:

$$\dot{x}_{t+\Delta t} = \dot{x}_t + \frac{\ddot{x}_t + \ddot{x}_{t+\Delta t}}{2} \cdot \Delta t \tag{2.62}$$

$$x_{t+\Delta t} = x_t + \dot{x}_t \cdot \Delta t + \frac{\ddot{x}_t + \ddot{x}_{t+\Delta t}}{4} \cdot \Delta t^2 \tag{2.63}$$

Generalized:

$$\dot{x}_{t+\Delta t} = \dot{x}_t + [(1-\delta) \cdot \ddot{x}_t + \delta \cdot \ddot{x}_{t+\Delta t}] \cdot \Delta t \tag{2.64}$$

$$x_{t+\Delta t} = x_t + \dot{x}_t \cdot \Delta t + \left[\left(\frac{1}{2} - \alpha\right) \cdot \ddot{x}_t + \alpha \cdot \ddot{x}_{t+\Delta t}\right] \cdot \Delta t^2 \tag{2.65}$$

Most of the time, the parameters used are $\alpha = 1/4$ and $\delta = 1/2$, changing the generalized expression back into equations (2.62) and (2.63). The variation the parameters influences the stability and dissipation conditions of the algorithm.

Combined with the equation of motion at time $t + \Delta t$

$$m \cdot \ddot{x}_{t+\Delta t} + c \cdot \dot{x}_{t+\Delta t} + k \cdot x_{t+\Delta t} = p_{t+\Delta t} \tag{2.66}$$

This method is renowned to be very stable provided that certain conditions are met. The stability of the Newmark is studied for an undamped free response. It is possible to express the response as:

$$x_{t+\Delta t} = \mathbf{A} \cdot x_t = \mathbf{A}^2 \cdot x_{t-\Delta t} = \cdots = \mathbf{A}^{n+1} \cdot x_0 \tag{2.67}$$

$$\text{With } \mathbf{A}\text{, the spectral decomposition matrix : } \mathbf{A} = \mathbf{P}\Lambda\mathbf{P}^-1 \tag{2.68}$$

$$\text{Allowing to compute } \mathbf{A}^n = \mathbf{P}\Lambda^n\mathbf{P}^-1 \tag{2.69}$$

$$\tag{2.70}$$

$\mathbf{A}^n$ is bounded providing the spectral radius $|\Lambda_i|$ does not exceed 1: $max|\Lambda_i| \leq 1$. If unbounded, $\mathbf{A}^n \rightarrow \infty$ and amplifies the perturbations. Oppositely, if $\mathbf{A}^n \rightarrow 0$, the pertubations are damped. In Newmark method, the computation of $\mathbf{A}$ depends on α,δ and a parameter $\beta = \omega \cdot \Delta t$. Figure 2.11 illustrates the different types of stability based on the value given to parameters α and δ of the Newmark equations as well as the β factor:

- Unconditionally stable: the system is stable no matter the value given to β, thus, no matter the time step. The spectral radius is equal to 1
- Conditionally stable: above a given value of β, the system becomes unstable and starts diverging. Numerical damping is induced in the model. The spectral radius is smaller than 1

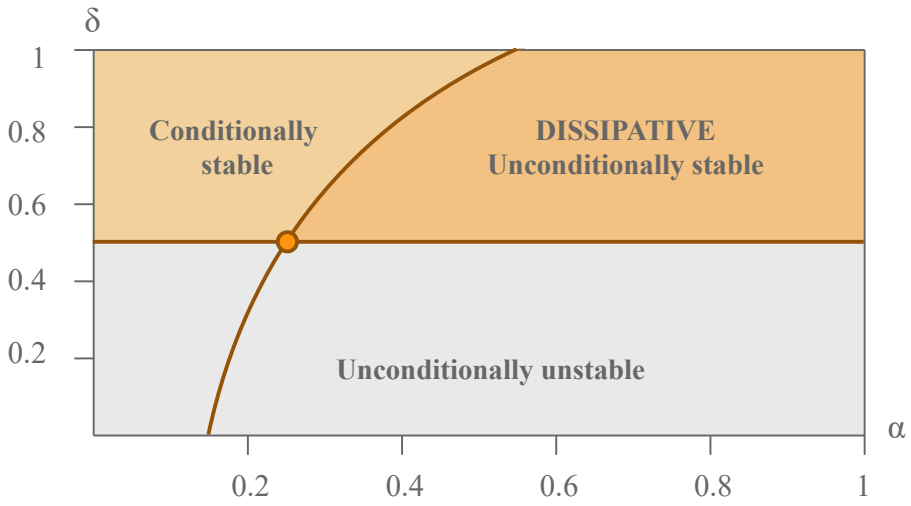

Figure 2.11: Stability based on the values of α and δ for Newmark method.

- Unconditionally unstable: no matter the value given to β, the system will never converge, due to the value given to parameters α and δ. The spectral radius is bigger than 1

The stability of the computations depends not only on the parameters α and δ, but also on the size of the time step. If the time step is too large, it may lead to numerical issues such as period elongation or aliasing.

Period Elongation:

Period elongation is a numerical artifact caused by the type of loading and the level of damping. It causes a stretching of the numerical period of the system, which results in less reliable solutions. The time step is too large to capture rapid oscillations, and the period of the system appears longer than its real period. This can lead to lags behind the true motion and accumulation of the error over the time of simulation. For example, for a free response, Figure 2.12 shows the percentage of elongation based on the ratio between Δt and T. It is possible to see that to remain within a range of 1 % of elongation, the ratio between the time step Δt and the period of the function should be inferior to 0.02.

$$\frac{\Delta t}{T} = 0.05 \Rightarrow \Delta t = 0.05 \cdot T = \frac{T}{20} \tag{2.71}$$

Aliasing: [1]

Aliasing is the misinterpretation of the period of the response signal when the number of computed points is not sufficient, as represented in Figure 2.13). To avoid aliasing, the number of points computed (sampling frequency) has to be bigger than twice the frequency of the function. This sampling frequency is called the Nyquist frequency.

$$f_{sampled} \geq 2 \cdot f_{function} \Rightarrow \Delta t = \frac{1}{2 \cdot f_{function}} \tag{2.72}$$

For example, for a sine wave with a period of 2 seconds (and a frequency of 0.5 Hz):

$$\Delta t = \frac{T}{20} = 0.1 \text{ s} \quad \& \quad \Delta t = \frac{1}{2 \cdot 0.5} = 1 \text{ s} \tag{2.73}$$

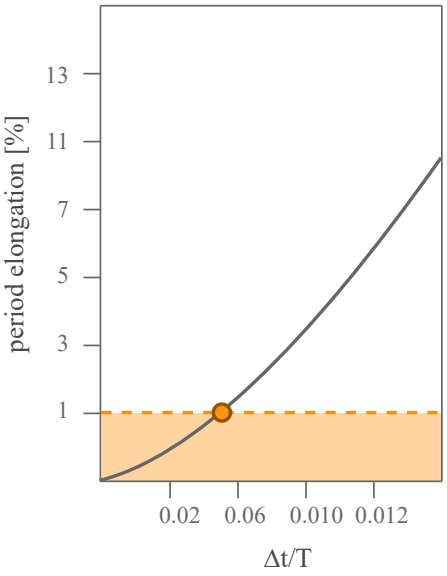

Figure 2.12: Period elongation based on the ratio between the time step Δt ans the period of the response.

The time step chosen will be the smallest of the two, i.e. 0.1 s.
NB: It is important to know that aliasing mistakes are more likely to happen in high frequencies, as the condition on the time step might take over the condition set by the period elongation. Those results are valid

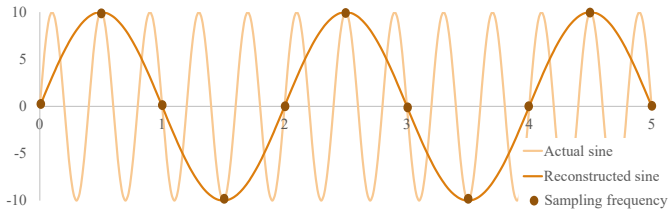

Figure 2.13: Example of an aliasing mistake: a sine with a period of 0.4 s is mistaken for a sine with a 2 s period, as the sampling frequency is too large ($\Delta t = 0.5$ s).

for a linear behaviour. As non-linearities are approached in this thesis, a second stability study based on the ratio between the time step and the period was conducted to quantify the impact of non-linearities on the accuracy of the results. However, these criteria already give a good basis for the study of the time step.

2.4 Non linear behaviour

When considering a structure with cables, non-linear effects have to be taken into account. Their behaviour is not linear anymore, necessitating a modification of the computation processes. For example, the deformation law of steel changes when considered from a linear or non-linear point of view. In linear analysis, the shape of the stress-strain relationship is often simplified into a bi-linear equation. To take into account the actual relationship, a different algorithm has to be used: the Newton-Raphson resolution method with forces in equilibrium. [2]

It consists of a set of iterative calculations that linearize portions of the constitutive law of the structure, which allows to compute a new stress state of the structure at each step. The equilibrium of the structure

has to be verified at all times by the principle of virtual work:

$$\underline{K_T} \cdot \underline{dp} = \underline{dP} \tag{2.74}$$

$$\int_V \left[dE_{k\ell} \cdot D_{ijk_i} \cdot \delta E_{ij} + S_{ij} \cdot d\delta E_{ij} \right] \, dV = \int_V \left[dF_i \cdot \delta U_i + F_i \cdot d\delta U_i \right] \, dV \tag{2.75}$$

With D_{ijk_i}, the tangent modulus, evolving at each step. Figure 2.14 gives an example of the computation of Γ_{n+1}, the configuration of the structure at $t = t_n + 1$ from Γ_n, the initial configuration of the structure at time $t = t_n$.

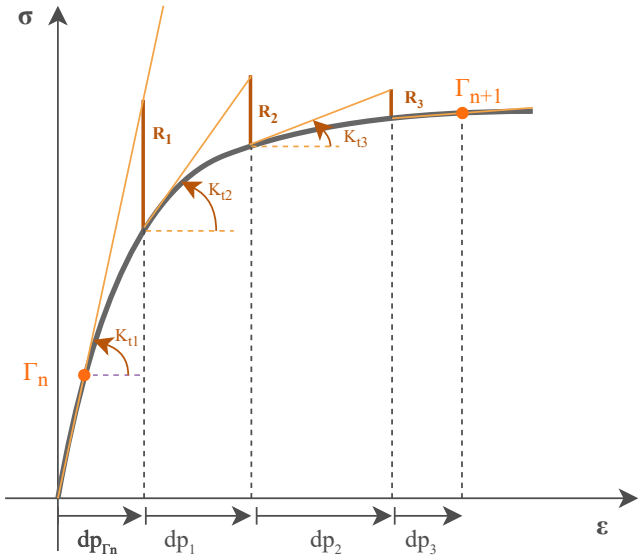

Figure 2.14: Conceptualisation of the Newton-Raphson Method for non-linear analysis.

With, for each increment:

$$\begin{cases} K_{t1} \cdot dp_1 = \underline{dP} \\ K_{t2} \cdot dp_2 = R_1 \\ K_{t3} \cdot dp_3 = R_2 \\ \vdots \end{cases} \Rightarrow dp_{\Gamma_{n+1}} = dp_{\Gamma_n} + dp_1 + dp_2 + dp_3 + \ldots \tag{2.76}$$

This method starts from the computation at a known point of the structure and computes the next step based on the tangent of the curve to this point. For the next step, the deviation between the value of the tangent in $p + dp_1$ and the value of the actual curve is computed. The iterations continue until equilibrium is reached, i.e. when the value of the tangent is equal to the value of the curve, thus, when $R_i = 0$. Reaching zero is close to impossible. To reduce computation time, a ratio R_i/R_1 has to be set, replacing the 0 value. A smaller value increases the accuracy but the computations will be more time-consuming. A trade-off has to be considered before the computations. For example, when R_1 is large, the ratio will be set at a low value, often around 10^{-6}, to avoid large R_i values. However, when the starting values are small, the ratio can be set lower, as the remaining R_i will be small as well, even with only a 10^{-3} ratio. In this work, it was noticed that the first steps of the structure induced larger values of R_i than the last. Thus, a different convergence criterion was set at the beginning and at the end of the time steps. When computing the response of a structure in time, the algorithm used is a combination of the Newmark method and the Newton-Raphson method: at each Newmark time step, the convergence of the structure is computed as well, with iterative Newton-Raphson steps in between.

3 Description of the structure

The suspended footbridge selected as a case study for this thesis is the Victor-Neels footbridge. It is located in the Eifel National Park, in North Rhine-Westphalia, Germany. The choice of this bridge has been made according to the following criteria: it had to be suspended, only accessible to soft mobility (pedestrians, bicycles, ...) and within a 2-hour drive of the university, to conduct the experimental campaign in a day. In addition, the bridge had to be accessible by car to easily transport the required machinery for the tests.

The footbridge is located in a valley and crosses the River Urft in a single span of **122.45 m**. Designing a suspended bridge with such a small span is highly unusual in civil engineering. As a matter of fact, as the technology to construct suspended bridges is quite complex and costly, they are often preferred for longer spans. The choice of that typology was probably also dictated by the desire to blend the bridge with the surrounding nature, as it is located in a national park. Suspended bridges reduce the amount of material and present a lighter aspect.

The footbridge was designed in 2009 by the German engineering office *Cornelissen + Partners*, and the vibration study was performed by the German engineering office *Ruscheweyeh Consults*. The drawings of the bridge and specificities regarding external damping means were provided by courtesy of *Cornelissen + Partners*.

A distinguishing feature of the studied footbridge is its single-pylon configuration, to which two main suspension cables are anchored. Vertical hangers, spaced at 3.95 m intervals, are attached along the length of these cables to support the deck, resulting in a total of 31 segments. Figure 3.1 gives an overview of the bridge.

Figure 3.1: Global view of the bridge.

The pylon, built in S355 steel, is approximately 20 m high with a wall thickness of 35 mm. It consists of two conical sections linked together by a cylindrical section. The cones have a diameter increasing from 35 cm at the top to 70 cm at the base, and the cylinder has a 70-mm diameter. The pylon is inclined at an angle of 17° to the vertical. As Figure 3.2 shows, its base is pinned, and a secondary set of two cables is connected to its top and anchored into the ground to counteract the forces from the main suspension cables. The anchorage is presented in Figure 3.3. To limit large vertical displacements of the deck, two additional stabilizing cables are attached to its sides. The entire bridge is built in steel, except for the aluminium surfacing plates.

Figure 3.2: Pinned support at the bottom of the pylon.

Figure 3.3: Anchorage of the back cables into the ground.

The deck structure comprises three longitudinal IPE 240 beams made of S235 steel. The two side beams are reinforced with angle profiles welded to their bottom flange. These angle profiles are used as rails for a mobile inspection device operating beneath the deck. These specific sections are visible in Figure 3.4. The deck is further stiffened by 32 cross-beams, corresponding to each set of hangers. Figure 3.4 shows that the longitudinal beams are not continuous along the whole span of the bridge, and are not rigidly connected together. They seem to behave as pinned-pinned beams supporting the decking, and then transferring the load of the deck to the cross-beams. These cross-beams connect the hangers from the main suspension cables to the deck and also serve as anchor points for the secondary bottom suspension cables, as represented in Figure 3.5. Each cross-beam is designed to enhance the pre-camber of the deck, that can be noticed in Figure 3.1. Structurally, the central part of each beam is an IPE 270, transitioning towards the sides into a reduced section similar to an IPE 210. Following the pre-camber, the beams at the extremities of the bridge have a section similar to the top section represented in Figure 3.6, while the middle beams have a section close to the bottom section represented in Figure 3.6. Sketches of the elevation of the bridge as well as its top view are represented in Figures 3.10 and 3.11.

Regarding the support conditions of the bridge, the deck and cables are identified as pinned support, as seen in Figure 3.3. A visit of the underdeck showed a pinned connection at both ends. A dilation joint must also be present, although it was not observed during the site visit. It is, however, presumed to be located at the end opposite the pylon, where the deck geometry is simpler and linear. The hypotheses on the support conditions are represented in Figures 3.7 and 3.8.

Ruscheweyeh Consults recommended the installation of two types of TMDs: a set of two TMDs for the vertical vibrations located at the centre of the bridge, and two sets of two TMDs located at a quarter and three quarters of the bridge for the torsional effects. They are highlighted in the top view of the bridge represented in Figure 3.9. Moreover, the set of vertical TMDs is positioned closer to the centre of the deck, whereas the sets of torsional TMDs are located further from the centre, to increase their efficiency.

Figure 3.4: Underdeck, with its main components: cross beams and longitudinal beams.

Figure 3.5: Link between the cross-beams and the secondary cables and the hangers.

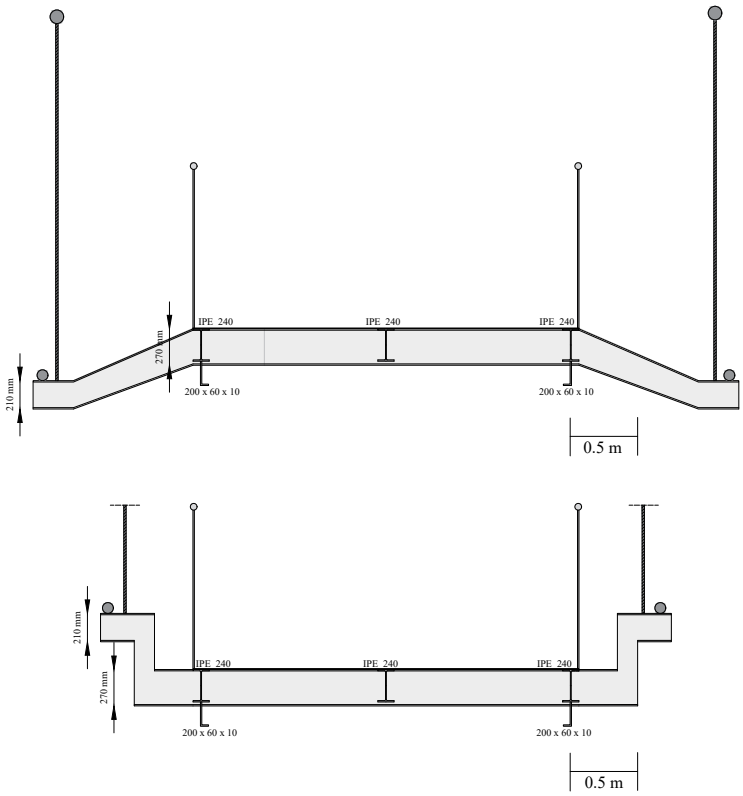

Figure 3.6: Representation of the two possible options for the cross section of the beams.

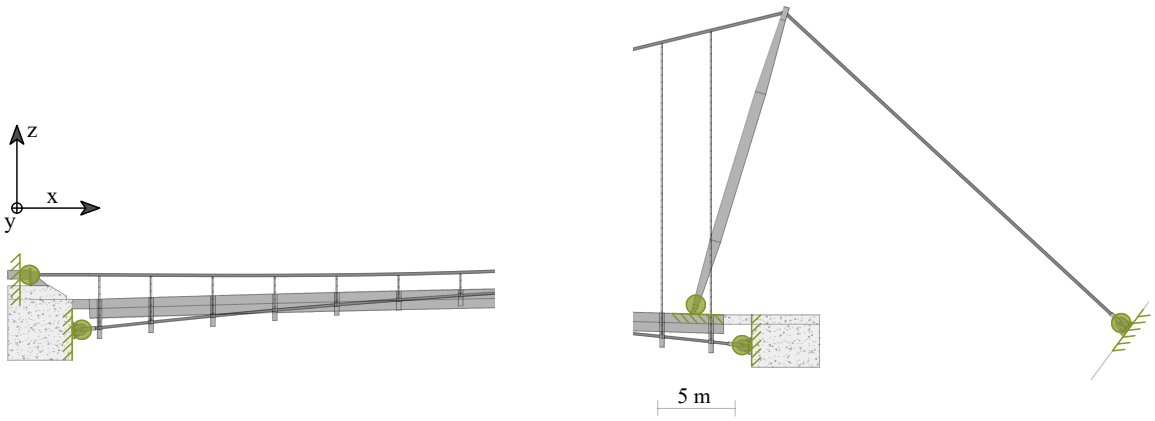

(a) Left side. (b) Right side (pylon side).

Figure 3.7: Representation of the support conditions for the cables and pylon: Green = free - Pink = blocked.

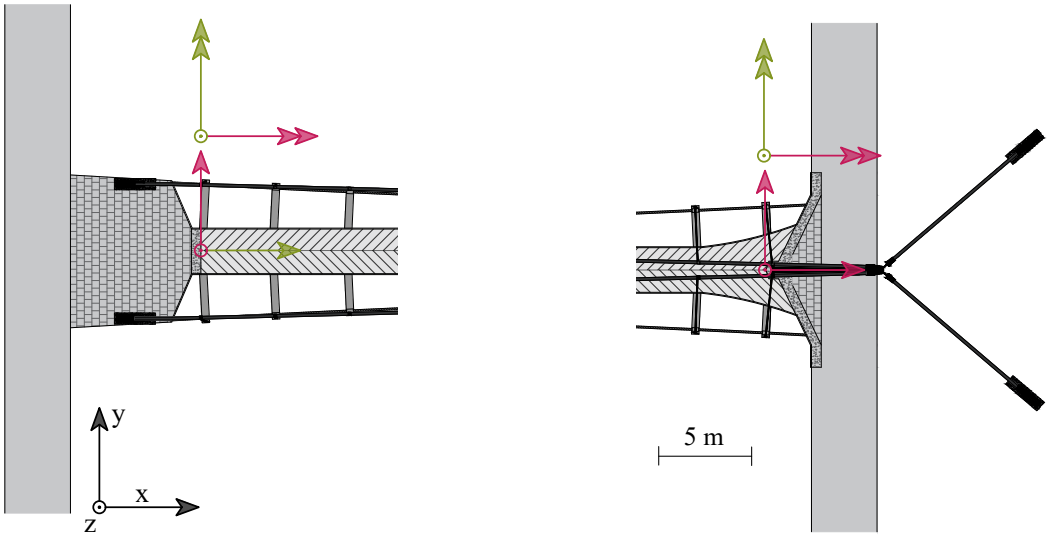

(a) Left side. (b) Right side (pylon side).

Figure 3.8: Representation of the support conditions for the deck: Green = free - Pink = blocked.

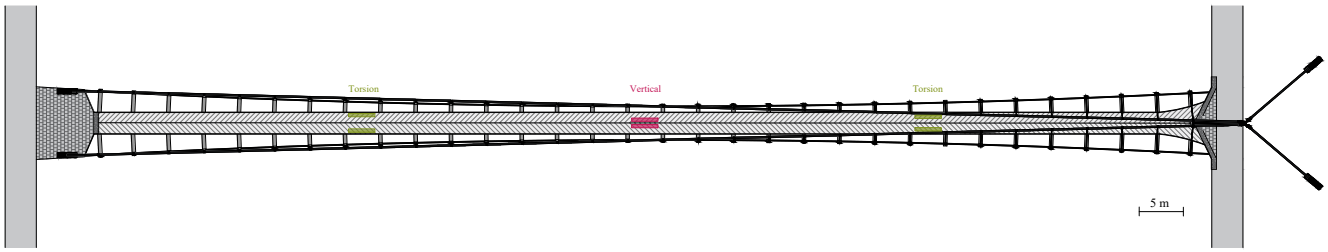

Figure 3.9: Position of the TMD on the bridge.

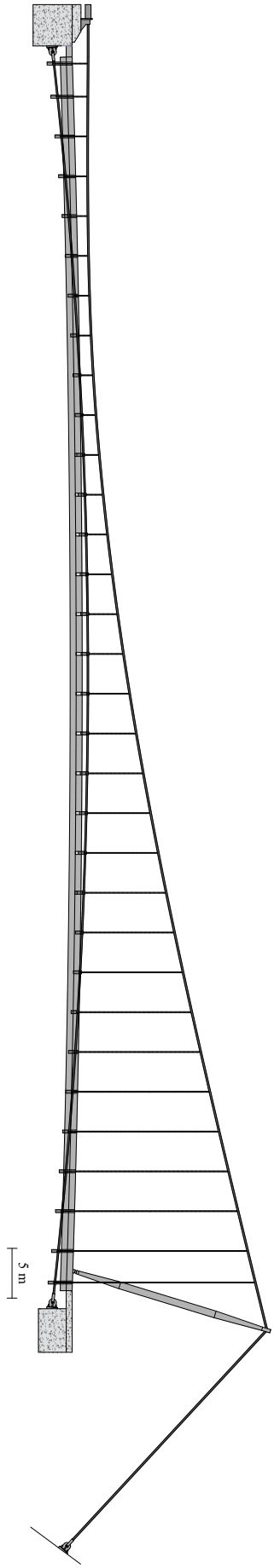

Figure 3.10: Representation of the elevation of the bridge.

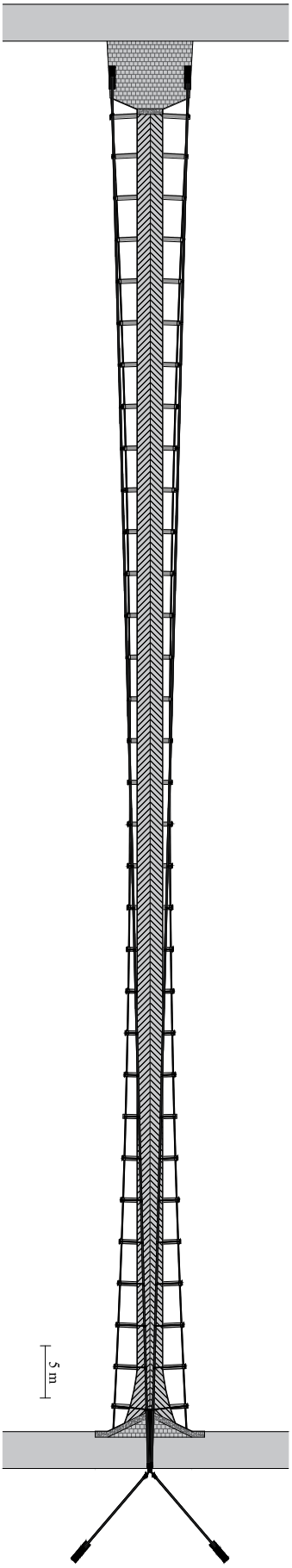

Figure 3.11: Representation of the top view of the bridge.

4 Experimental Approach

This chapter is divided into two subsections. The first section explores the main concepts of signal analysis, from signal classification to identification methods based on the data available. It illustrates the panels of techniques used to extract the information needed throughout this work (mode shape, eigenfrequencies, damping coefficient, ...), during the experimental analysis, as well as the numerical analysis. Then, the second section describes the experimental campaign, the process of the experimental testing on-site and the equipment used. The data collected is then analysed. The purpose of this campaign is to validate the numerical model. That is essential to rely on the results of the numerical model. To this end, the mode shapes and eigenfrequencies of several modes are computed, to have a basis of comparison with the modal analysis of the model. Moreover, the tension in a few hangers is measured as well, to estimate the tension distribution in the hangers of the bridge and adjust the numerical model to that distribution.

4.1 ToolBox

Signal Classification

The process used to analyse data from experimental campaigns depends on the excitation techniques performed on the studied structure. Several methods have been developed over the years in order to study any structural response and extract the needed information.

In order to identify the analysis technique to use, it is crucial to classify the type of input used to excite the structure. They can be divided into two groups: the deterministic signals, whose value can be computed at any given time, and the stochastic signals. The latter cannot be described by a single equation and are characterised by their stochastic values, such as mean, variance, ... Deterministic signals can again be divided into two subgroups: the periodic signals, that repeat themselves over time, and the transient signals, that are not periodic but can still be characterized by a single equation. Regarding the stochastic signals, they can be defined as stationary if their stochastic characteristics are independent of time. The signal classification is summed up in Figure 4.1.

- **Deterministic periodic signal**: Sine wave

$$s(t) = A \cdot \sin(\omega \cdot t + \phi) \tag{4.1}$$

  with A, the amplitude of the sine - ω the pulsation of the signal - ϕ, the initial phase of the signal

- **Deterministic transient signal**: Sine Sweep - A sine sweep is a sinusoidal signal with a frequency varying with time. It is used to sweep a given range of frequencies at an imposed angular speed. In this work, the sine sweep used are linear, their frequency evolves linearly with time but they can be

exponential as well.

$$s_{sw}(t) = A \cdot \sin(\omega_0 \cdot t + \frac{1}{2} \cdot \dot{\omega} \cdot t^2) \tag{4.2}$$

$$\dot{\omega} = 2 \cdot \pi \cdot \left(\frac{f_{final} - f_0}{T}\right) \tag{4.3}$$

with A, the amplitude of the function; ω_0, the initial pulsation of the signal; $\dot{\omega}$, the angular speed of the sweeping; f_{final}, the end frequency of the signal; f_0, the initial frequency of the signal and T, the amount of time to go from the first frequency to the last.
At each time step, it is possible to compute the instantaneous frequency of the sine by deriving the instantaneous phase $\phi(t)$:

$$\phi(t) = \omega_0 \cdot t + \frac{1}{2} \cdot \dot{\omega} \cdot t^2 \tag{4.4}$$

$$\phi'(t) = \omega(t) = \omega_0 + \dot{\omega} \cdot t \tag{4.5}$$

- Stochastic stationary signal: **Ambient excitation** - This type of signal is considered random, such as an excitation due to the wind. It can't be described with a simple equation.

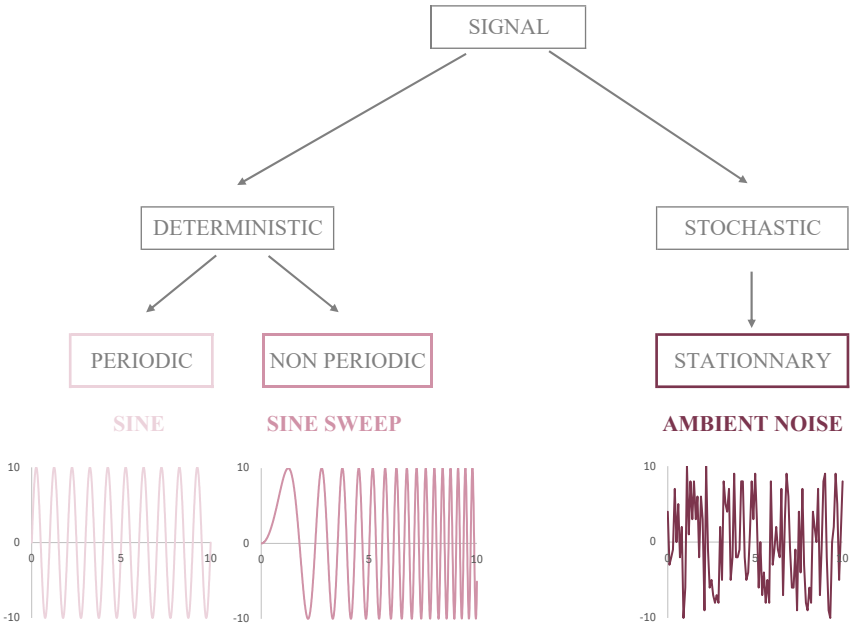

Figure 4.1: Signal classification.

Signal Analysis

The technique used to analyse the response of a structure depends on the available data. The method is generally more accurate when the excitation signal and the response signal are both available. When trying to identify the modal characteristics of a structure, the aim is to get both the input signal and the response of the structure, as this is the purest way to compute the eigenfrequencies and excitation levels. In all cases, the response signals can be studied in the same way with two of the most used formulae in signal analysis: the Fourier Transform (FT) and the Power Spectral Density (PSD). Those two methods

express signals that were originally a function of time in the frequency domain, and thus, extract the frequency content of said signals to estimate the resonant frequencies of the structure.

During the computation of the FT, the signal is broken down into the sine and cosine wave components. The amplitude of each periodic function is stored, illustrating which component contributes the most to the original signal. The concept of the FT is illustrated in Figure 4.2. When the FT is known, the PSD can be computed as well, as it is equal to the squared modulus of the FT, divided by the time of integration. The PSD represents the power of the signal, based on its frequency. It can be useful, for example, in the case of a signal clouded by noise: the PSD represents how powerful the noise is compared to the original signal. Examples of FT and PSD applied to the signal represented in Figure 4.2 can be found in Figure 4.3

For a signal f(t), with its FT $\hat{f}(\omega)$, and PSD $S(\omega)$:

$$\hat{f}(\omega) = FT(x) = \int_{-\infty}^{+\infty} f(t) \cdot e^{-i\cdot\omega\cdot t} dt \quad \Rightarrow \quad S(\omega) = \frac{|\hat{f}(\omega)|^2}{\Delta T} \tag{4.6}$$

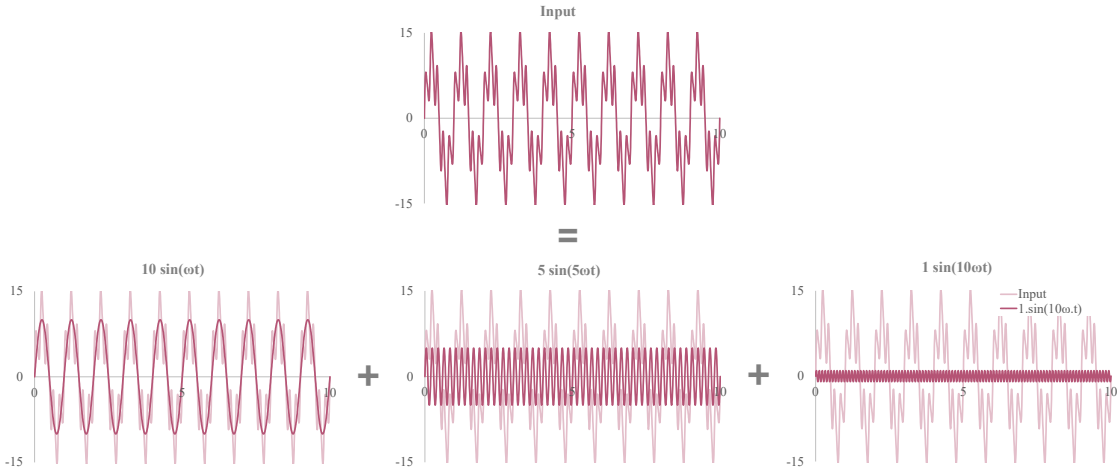

Figure 4.2: Representation of the concept of a Fourier Transform (FT).

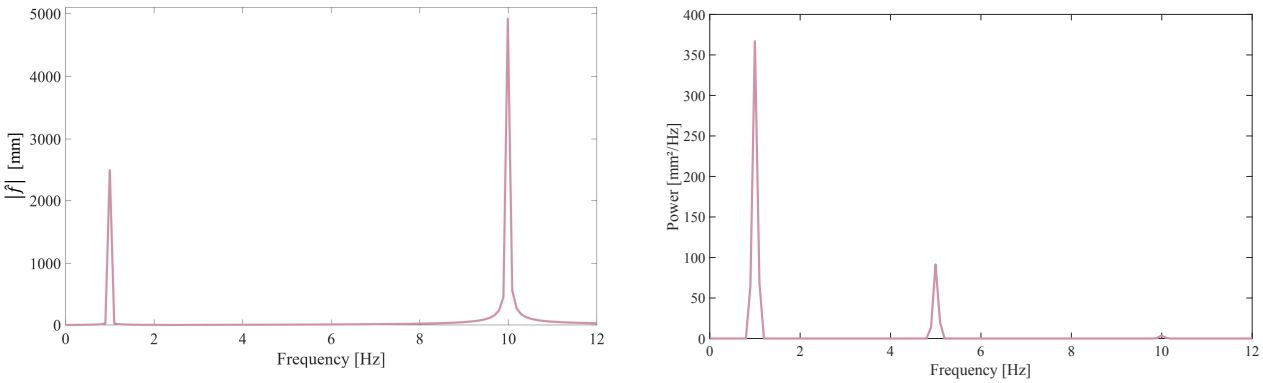

(a) Example of a FT applied to the signal represented in Figure 4.2.

(b) Example of a PSD applied to the signal represented in Figure 4.2.

Figure 4.3: Examples of FT and PSD, applied to the signal represented in Figure 4.2.

Deterministic signal

The deterministic signals can easily be processed, and used to compute useful data to understand the behaviour of the tested structure. The most interesting function to extract from a deterministic approach is the Frequency Response Function (FRF), $H(\omega)$:

$$H(\omega) = \frac{X(\omega)}{F(\omega)} \tag{4.7}$$

with $X(\omega)$, the response of the system in the frequency domain (FT of the output response) and $F(\omega)$, the input signal of the system in the frequency domain (FT of the input). The FRF links the input and output responses, and thus characterizes the response of a structure to any given input signal. For example, applying a sinusoidal signal with a frequency $f_{sine} = f_1$ on a structure whose eigenfrequency is equal to f_1 will result in a peak in the FRF at f_1. For all other sinusoidal signals with a frequency different from f_1, the FRF will not peak. As can be seen in Figure 4.4, the ingoing signal is the same as in Figure 4.2, but the participation of $sin(10 \cdot \omega \cdot t)$ is more important in the response signal, and $sin(5 \cdot \omega \cdot t)$ is not present in the response. The FRF is a source of information on the eigenmodes, in addition to giving

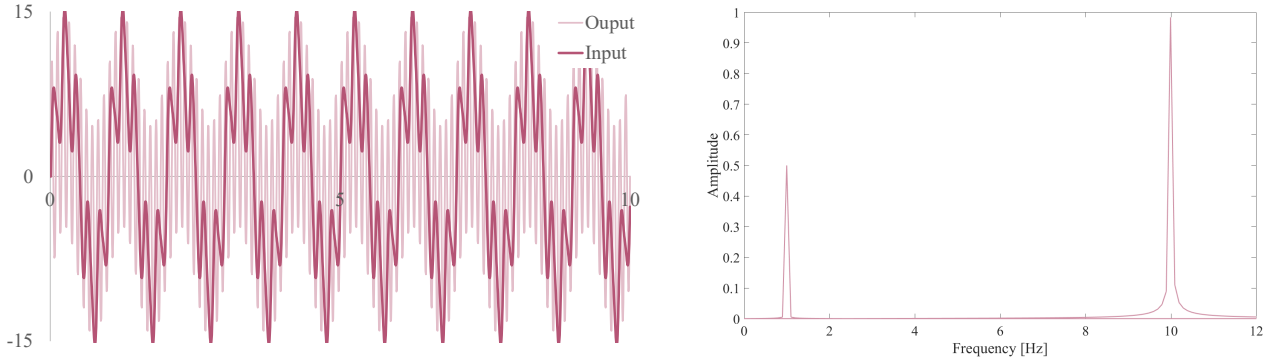

(a) Signals taken as examples for the computation of a Frequency Response Function (FRF).

(b) Example of a FRF applied to the signals represented in Figure 4.4 (a).

Figure 4.4: Example of a FRF.

the amplitude of participation of a frequency to the response of the structure. The width of the FRF represents the damping coefficient per mode. The narrower the peak, the less damped the mode. It can be characterized by a quality factor Q:

$$Q = \frac{\omega_k}{\Delta\omega} \tag{4.8}$$

$$\xi_k = \frac{1}{2 \cdot Q} = \frac{\omega_b - \omega_a}{2 \cdot \omega_k} \tag{4.9}$$

With ω_a and ω_b the frequencies attributed to the half-power point value, the values where the output power has dropped by half of its peak value. As the power is proportional to the square of the amplitude of the FRF, the amplitude at which the power is halved corresponds to $1/\sqrt{2}$ of the maximal amplitude of the FRF. The bigger the quality factor, the less damped the system, as $\Delta\omega$ will be smaller, and thus, the peak will narrow down, as illustrated in Figure 4.5. This quality factor method is an alternative in the frequency domain to the log-decrement method (see section 2) set in the time domain, both allowing to compute the damping ratio of the structure. [1]

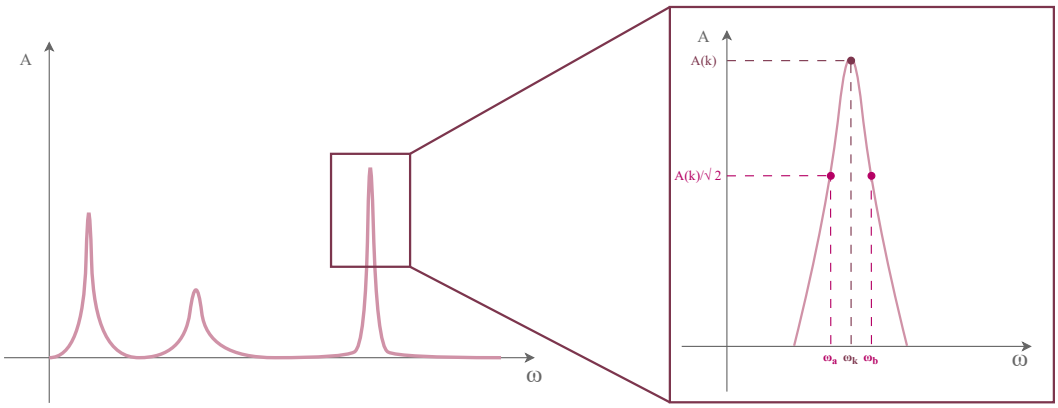

Figure 4.5: Main parameters in the estimate of the damping coefficient ξ_k of eigenmode k, based on the shape of the FRF.

Non Periodic signal

Non-periodic signals such as sine sweeps are often used to reconstruct the FRF of a given eigenfrequency, when the studied structure is non-linear. Non-linear structures have a very specific behaviour because either their damping ratios, stiffness, or masses evolve when the structure is excited. Non-linearities due to mass are rarer in civil engineering, but can be illustrated by a water tower emptying during an earthquake. During the excitation of the tower, the mass will decrease with time and lead to a non-linear behaviour of the structure. The evolution of damping, however, is much more difficult to grasp, and is often only determined experimentally or not taken into account at all during calculations. Non-linearities due to stiffness are usually represented by a cubic restoring force in the equation of motion instead of a linear one, as represented in equation (4.10) and Figure 4.6. That force results in a quadratic stiffness, instead of a constant one. That evolution of stiffness is used to model the behaviour of cable elements.

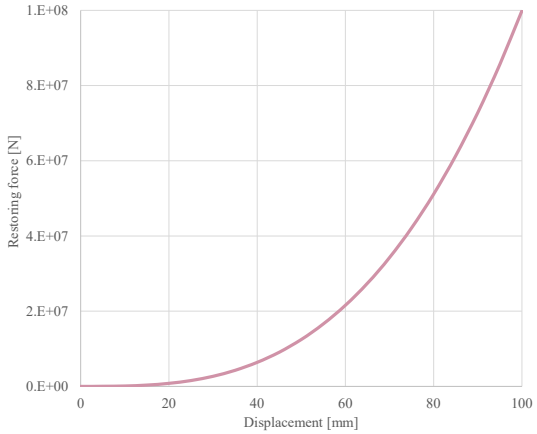

Figure 4.6: Schematic representation of the evolution of cubic restoring force based on displacement.

$$m \cdot \ddot{x}(t) + c \cdot \dot{x}(t) + k_1 \cdot x(t) + k_2 \cdot x^2(t) + k_3 \cdot x^3(t) \tag{4.10}$$

With k_1 [N/m], k_2 [N/m^2], k_3 [N/m^3].

Non-linearities influence the shape of the FRF: the peak will be more and more inclined as the non-linearity increases, as represented in Figure 4.7. The inclination towards higher frequencies represents a hardening

of the structure (increasing stiffness), and the inclination towards lower frequencies indicates a softening (decreasing stiffness) [3].

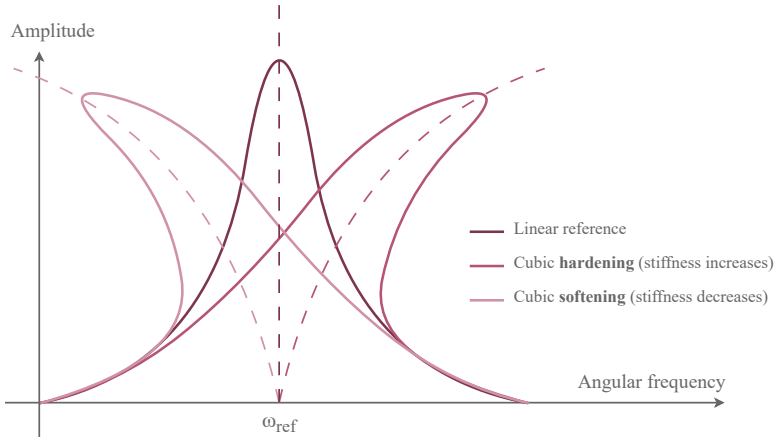

Figure 4.7: Evolution of the FRF based on the type of stiffness non-linearity.

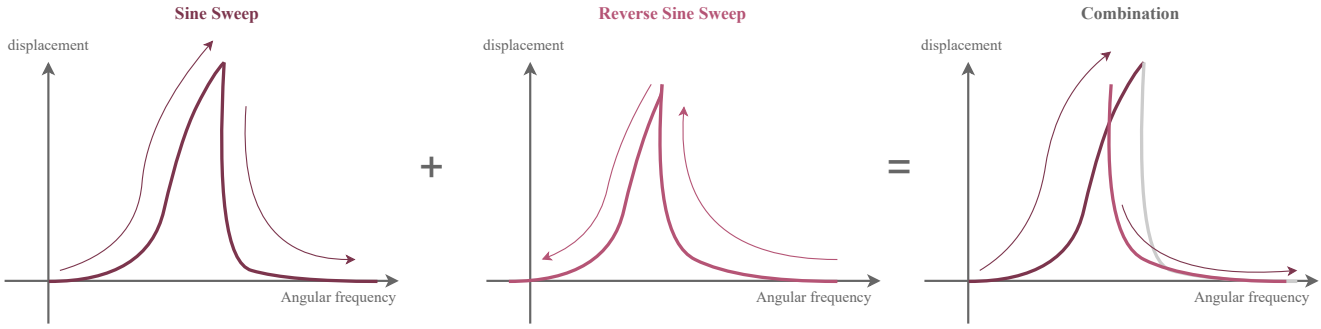

(a) Sine sweep process in order to get the FRF of the structure around a given frequency.

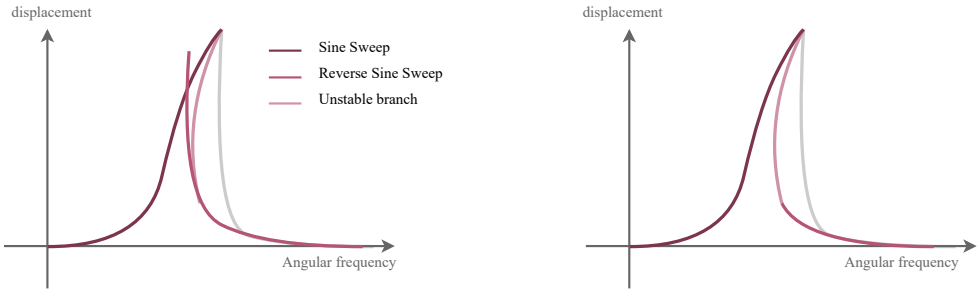

(b) Final reconstruction of the FRF, adding the unstable branch.

Figure 4.8: Example of a FRF reconstruction with sine sweeping.

Figure 4.7 shows that the eigenfrequency of a non-linear system is not finite anymore: a range of frequencies can respond at high amplitude and, more importantly, the eigenfrequency identified is not necessarily the most problematic frequency.

Due to that frequency shift, non-linear structures are excited with a sine sweep instead of a regular sine wave. The sine will sweep throughout a range of frequencies around the eigenfrequency to identify the most critical ones. The sine sweep process is completed in two stages: a sweep going from low to high frequencies, in order to get the first branch of the FRF (first sweep in Figure 4.8 (a)) and then, a reversed

sweep from high to low frequencies, to get the second part of the FRF (second sweep in Figure 4.8 (a)). It is then possible to reconstruct part of the FRF. However, there is an unstable branch that can only be obtained through experimental procedures, linking the two branches of the FRF.

To switch from the response of the sine sweep to the branches of the FRF, a Hilbert transform [4] is applied to the displacement based on time resulting from the excitation. The Hilbert transform produces a frequency-based envelope of the original time-based signal, as represented in equation (4.11) and Figure 4.9.

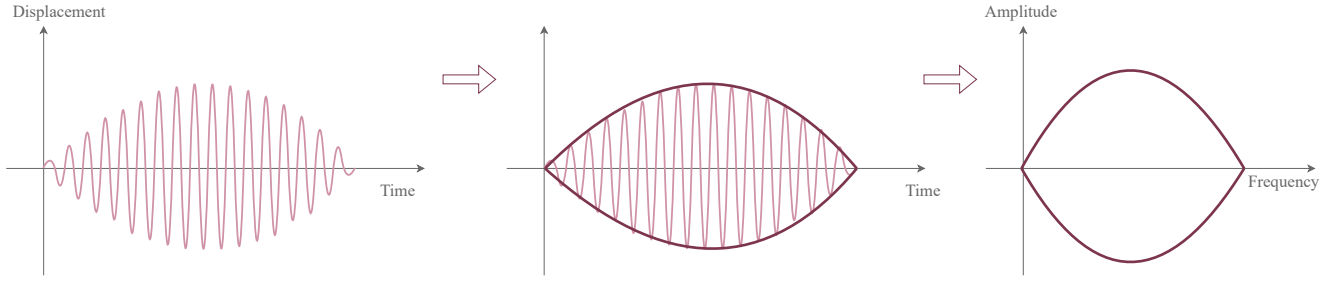

Figure 4.9: Schematisation of the concept of the Hilbert Transform.

It can be put into equation as follows:

$$\forall\, \tau \in [-\infty;\infty] \;:\; H(f(t)) = f(t) \cdot \frac{1}{\pi \cdot t} = \frac{1}{\pi} \cdot \int_{-\infty}^{\infty} \frac{f(t)}{t-\tau}\, d\tau = \frac{1}{\pi} \cdot \int_{-\infty}^{\infty} \frac{f(t-\tau)}{\tau}\, d\tau \tag{4.11}$$

Random signal

Random signals are rarely measured and used in the computation of the modal characteristics of a structure. The response signals to those excitations are analysed with a stochastic identification method, and specifically in this work, with the Covariance-driven Stochastic Subspace Iteration method (COV-SSI method) [5].

When computing the eigenfrequencies, mode shapes, damping coefficient, mode stability, ... of a system, the classical identification methods most often rely on a **input-output** based dataset. However, in the particular case of random excitation generated by an uncontrolled source (pedestrians, ambient forces, wind, ...), it is nearly impossible to estimate the input signal. To compute results, an assumption is made: **the input signal of a random excitation non-generated by a machine is a consequence of a stochastic process, that can be compared to white noise**. However, the main issue in the case of output-only analyses is that if the input contains some dominant frequencies, they cannot be separated from the eigenfrequencies of the system and will be identified as such. This means that if the white noise is generated by people walking, the eigenfrequencies in the [1.7-2.1] Hz range are possibly spurious and should not be taken into account in the identification process. In addition, the FT of the output cannot be of use to determine the eigenfrequencies in that range as it is impossible to determine whether a peak in the FFT in that range is due to a response to an eigenfrequency or a forced response of the deck.

NB: a forced response is a response to a frequency which is not an eigenfrequency of the deck but is applied with enough amplitude to force a response of the deck at that frequency.

In order to apply the *COV-SSI* method, it is important to have multiple output signals coming from various locations on the structure. The *COV-SSI* method is based on a discrete time formulation: the stochastic response is a function of the time.

$$\underline{y}(t) = \begin{Bmatrix} y_1(t) \\ y_1(t) \\ \dots \\ y_m(t) \end{Bmatrix} \tag{4.12}$$

The equation of motion of the system can thus be interpreted as a classical MDOF system:

$$\mathbf{M} \cdot \underline{\ddot{y}}(t) + \mathbf{D} \cdot \underline{\dot{y}}(t) + \mathbf{K} \cdot \underline{y}(t) = \underline{f}(t) \tag{4.13}$$

where **M** is the mass matrix, **D** the damping matrix, **K** the stiffness matrix and $\underline{f}(t)$ is the loading vector. To take the classical continuous time formulation to the discrete time domain, let's use $\underline{x}(t)$, the State Space formulation, where $\underline{x}$(t) is a vector that represents the system at any time t:

$$\underline{x}(t) = \begin{Bmatrix} \underline{y}(t) \\ \underline{\dot{y}}(t) \end{Bmatrix} \tag{4.14}$$

Using that terminology in the equation of motion, the system can be re-written as follows, as a state space form:

$$\underline{\dot{x}}(t) = \mathbf{A}_c \cdot \underline{x}(t) + \mathbf{B} \cdot \underline{f}(t) \tag{4.15}$$

$$\underline{y}(t) = \mathbf{C} \cdot \underline{x}(t) \tag{4.16}$$

where

$$A_c = \begin{bmatrix} 0 & \mathbf{I} \\ -\mathbf{M}^{-1} \cdot \mathbf{K} & -M^{-1} \cdot \mathbf{C} \end{bmatrix} \quad \& \quad \mathbf{B} = \begin{bmatrix} 0 \\ \mathbf{M}^{-1} \end{bmatrix} \tag{4.17}$$

The general solution of such an equation is given by:

$$\forall\, \tau \in [0;t] : \underline{x}(0) \cdot \underline{x}(t) = e^{\mathbf{A}_c \cdot t} + \int_0^t e^{\mathbf{A}_c \cdot (t-\tau)} \cdot \mathbf{B} \cdot \underline{f}(\tau) d\tau \tag{4.18}$$

Where the pink part of the equation is the homogeneous solution and the grey part is the particular solution.

From measured outputs y_t, let's compute the output covariance sequence, in order to find how much the system can "predict" itself over time. The output covariance in lag i, for ℓ number of output variables (number of accelerometers providing data) is defined by:

$$\hat{R}_i = \frac{1}{N-i} \cdot \sum_{\tau=1}^{N-i} \underline{y}_{\tau+i} \underline{y}_{\tau}^T \quad \mathbf{R}_i \in \mathbb{R}^{\ell x \ell} \tag{4.19}$$

$$\mathbf{R}_i = \mathbb{E}[\underline{y}_{\tau+i} \underline{y}_{\tau}^T] \text{ for } i = 0,1,\dots,2i-1 \tag{4.20}$$

where N represents the number of data points. This allows to build the Toeplitz matrix based on the covariance results R_i computed above:

NB: a Toeplitz matrix is a matrix in which each descending diagonal (from left to right) is constant, as opposed to the Hankel matrix where the anti diagonals (right to left) are constant

$$\mathbf{T}_i = \begin{bmatrix} \mathbf{R}_1 & \mathbf{R}_2 & \dots & \mathbf{R}_i \\ \mathbf{R}_2 & \mathbf{R}_3 & \dots & \mathbf{R}_{i+1} \\ \vdots & \vdots & \ddots & \vdots \\ \mathbf{R}_i & \mathbf{R}_{i+1} & \dots & \mathbf{R}_{2i+1} \end{bmatrix} \tag{4.21}$$

Applying singular value decomposition to the Toeplitz matrix:

$$\mathbf{T}_i = \mathbf{U} \cdot \Sigma_i \cdot \mathbf{V}^T \tag{4.22}$$

where U is an orthogonal matrix whose columns are the left singular vectors of $\mathbf{T}_i$, Σ_i is a diagonal matrix with diagonal elements that are the singular values σ_i and $\mathbf{V}$ is an orthogonal matrix whose columns are the right singular vectors of $\mathbf{T}_i$. The matrices are truncated for n, the value of the model order:

$$\mathbf{U}_1 = U(:,1:n) \qquad \Sigma_1 = \Sigma(1:n, 1:n) \tag{4.23}$$

The extended observability matrix Γ, allows to understand the internal dynamic behaviour and can be computed by an estimation $\hat{\Gamma}$:

$$\Gamma_i = \begin{bmatrix} \mathbf{C} \\ \mathbf{C} \cdot \mathbf{A} \\ \vdots \\ \mathbf{C} \cdot \mathbf{A}^{i-1} \end{bmatrix} \in \mathbb{R}^{i\ell \text{x} n} \qquad \hat{\Gamma}_i = \mathbf{U}_1 \Sigma_1^{1/2} \tag{4.24}$$

Estimate of $\mathbf{A}$ and $\mathbf{C}$:

- $\hat{\mathbf{C}}$: the first ℓ rows of $\hat{\Gamma}_i$
- $\hat{\mathbf{A}}$:

$$\hat{\Gamma}_i = \begin{bmatrix} \hat{\Gamma}_1 \\ \hat{\Gamma}_2 \end{bmatrix} \quad \text{where} \quad \begin{matrix} \hat{\Gamma}_1 = \hat{\Gamma}_i(1:(i-1)\cdot\ell) \\ \hat{\Gamma}_2 = \hat{\Gamma}_i(\ell+1:i\cdot\ell) \end{matrix} \quad \text{and} \quad A = \hat{\Gamma}_1^{\dagger}\hat{\Gamma}_2 \tag{4.25}$$

  and $\hat{\Gamma}_1^{\dagger}$ is the pseudo-inverse of $\hat{\Gamma}_1$

The modal parameters can then be identified:

$$\lambda_n, \Lambda_n = \det(\mathbf{A} - \lambda \cdot \mathbf{I}) \tag{4.26}$$

$$s_i = \frac{ln(\lambda_i)}{Fs} = \sigma_i + j \cdot \omega_{d,i} \tag{4.27}$$

$$f = \frac{|\omega_i|}{2 \cdot \pi} \;\; \& \;\; \omega_i = \sqrt{\sigma_i^2 + \omega_{d,i}^2} \tag{4.28}$$

$$\xi_i = -\frac{\sigma_i}{\omega_i} \tag{4.29}$$

$$\phi_i = \mathbf{C} \cdot \Lambda_i \tag{4.30}$$

Eventually, it is possible to compute the stability of the computed poles, i.e. if the modes identified are stable in frequency, damping and shape with the increase of the model order. For model order k:

$$\epsilon_f = \left| \frac{f^n - f^{n+k}}{f^n} \right| < 1\ \% \tag{4.31}$$

$$\epsilon_\xi = \left| \frac{\xi^n - \xi^{n+k}}{\xi^n} \right| < 1\ \% \tag{4.32}$$

$$\epsilon_\phi \text{ (MAC criterion)} = \frac{|(\phi^n)^H \phi^{n+k}|^2}{||(\phi^n||^2 ||\phi^{n+k}||^2} > 95\ \% \tag{4.33}$$

If the poles verify one or more of these criteria, they can be considered:

- stable in frequency
- stable in damping
- stable in shape
- stable overall

This is used to represent the stabilization diagram and have a visual representation of the stability of the modes.

Excitation of the bridge

There are three main ways to excite a large structure such as a bridge:

- **Shaker**: the shaker consists in a set of masses attached to an actuator. By moving the actuator, the masses are accelerated and induce a force in the tested structure. The generated load can be fully random or sinusoidal. As the shaker is managed by a computer and is equipped with sensors following the movement of the masses, the force induced in the structure is known at all time. The shaker is most often used to excite a structure at a specific frequency with a sine wave, as shown in Figure 4.11 below.

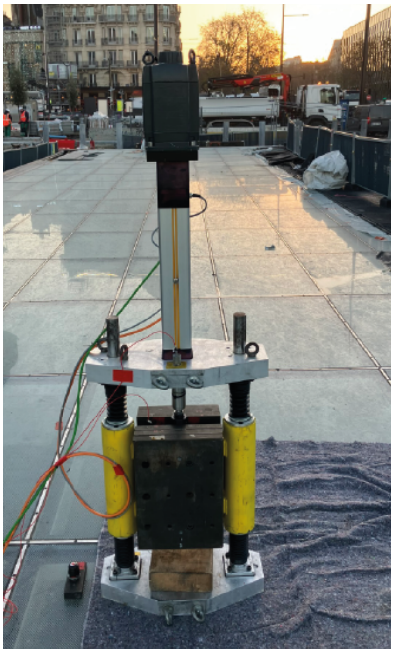

Figure 4.10: Shaker used for bridges - from V_2i.

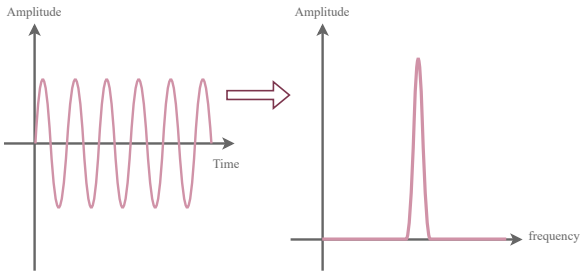

Figure 4.11: FT of a sine wave signal: Left force applied to the structure - Right: FT of the force.

- **Hammer**: the hammer is a device used to give an Dirac-like impulse, in order to channel the free response of the structure. It is equipped with a sensor, allowing to know the shape and intensity of the impulsion. Depending on the frequencies that need to be triggered, the head of the hammer can be changed. A steel nozzle is used to generate the clearest signal, and reach as many frequencies as possible. In contrast, if there is no need to trigger high frequencies, the nozzle used is made of rubber, a softer material, that produces a more diffuse impact. The hammer and the difference

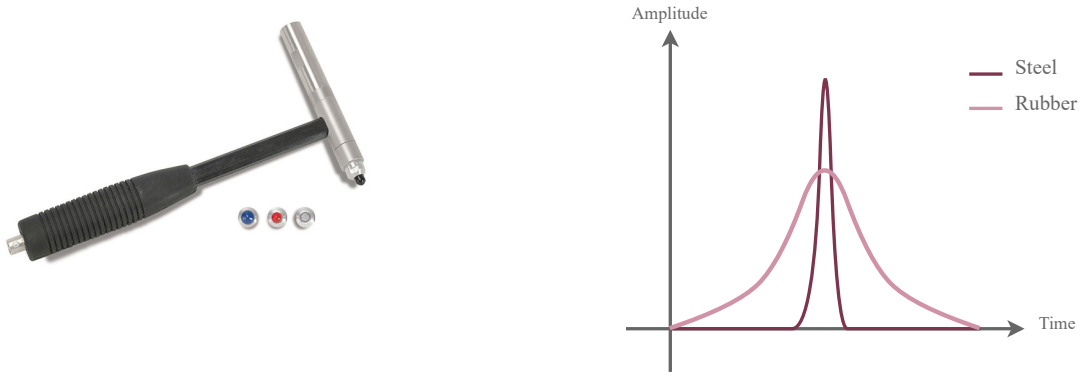

(a) Example of an impact hammer (from *SINUS Messtechnik GmbH- Sound and Vibration measurement systems.*

(b) Effect of the nozzle of the hammer on the impulse load.

Figure 4.12: Representation of a hammer used in civil engineering and schematics of the effect of the nozzle on the impulse load.

between the two types of nozzles are represented in Figure 4.12. The advantage of the hammer is that, when an impulse is given, it triggers all the frequencies of the structure at once. Indeed, as the input is a Dirac-like function, its FT is a constant on all the spectrum, as represented in Figure 4.13.

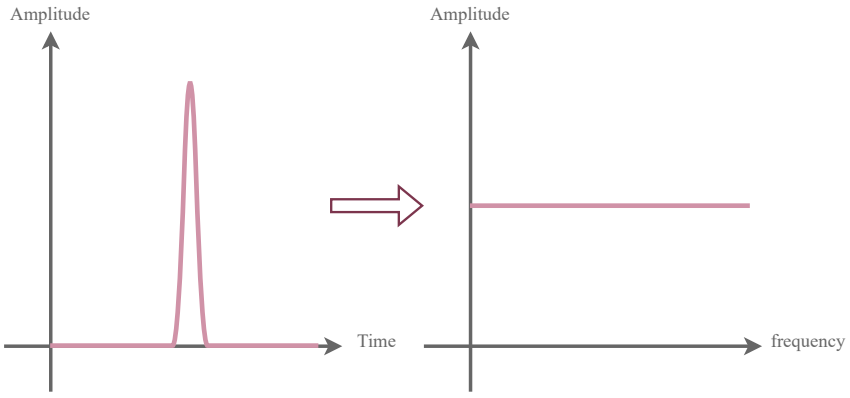

Figure 4.13: FT of a Dirac-like signal: Left force applied to the structure - Right: FT of the force.

- **Ambient noise**: this method consists in letting the structure behave by itself when subjected to the elements (wind, rain, ...). It will naturally respond to its eigenfrequencies, at a small amplitude and the response of the structure will allow to identify those frequencies. Those excitations are seldom measured, as they are completely random.

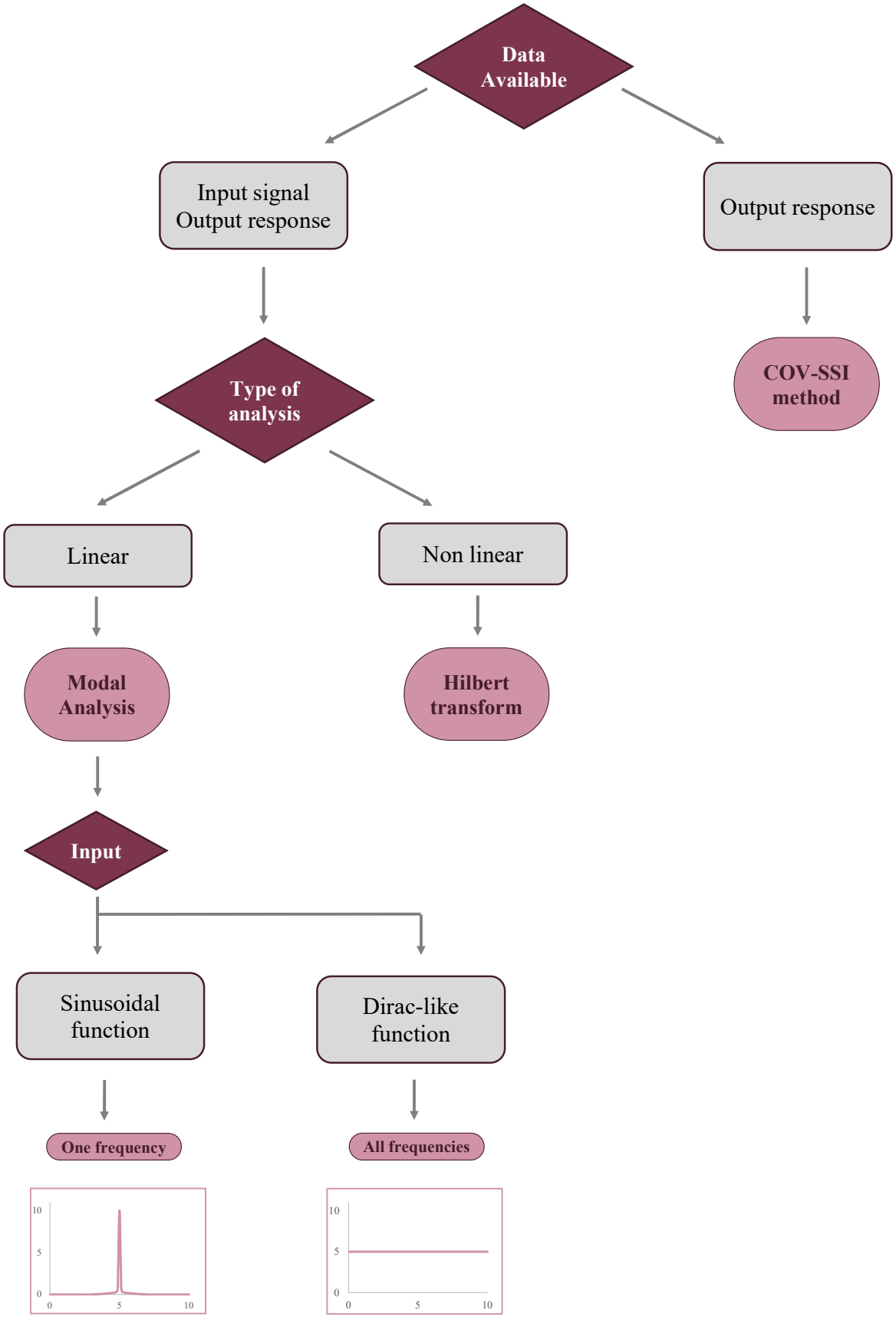

Figure 4.14: Type of analysis to use for signal treatment depending on the data available.

4.2 Experimental tests

The purpose of experimental testing is to validate the numerical model developed with the software `Finelg`. First, the eigenvalues have to be determined as well as their corresponding modes. It is important to ensure that the deformed shapes of the numerical modes correspond to the real-life ones. When the numerical modes do not match the shape of the experimental ones, it is often the result of spurious support conditions in the model. Stiffness or material issues can be identified if the eigenfrequencies of the model and the experimental campaign are too far apart, but the mode shapes are correct. In bridges with cables, stiffness can be validated by measuring the free response of a hanger after an impact. The eigenfrequency of the response can be determined, and is directly linked to the internal tension. Taut cables are stiffer than loose ones and that quick check can be applied to several cables to estimate a global tension repartition in all hangers, and thus verify the eventual difference in stiffness with the model.

The purpose of the experimental campaign was also to test the dynamic amplification of the bridge under the same signal, at different amplitudes, in order to characterize the non-linearities due to stiffness and damping. A totally linear structure has a constant amplification rate: if a 100 N force induces a 10 mm displacement, a 200 N force will induce a 20 mm displacement. However, in non-linear structures, the increase of the amplification levels is not straightforward and has to be characterized for every different system.

The **original** plan for the tests was to conduct a campaign with the help of machinery, in particular, a shaker. The tests with a shaker are split into three periods, summed up in Figure 4.15:

1. **Random solicitation**, to highlight the main eigenfrequencies.
2. **Sine Sweep** around the frequencies highlighted browsing through a specified range of frequencies, to identify precisely the most responsive frequency.
3. **Controlled solicitations**, with a sine wave signal. Its frequency is based on the natural frequency emphasized by the sine sweep. The shaker is often moved between the frequencies, so that the tests are always performed in an anti-node of the triggered mode.

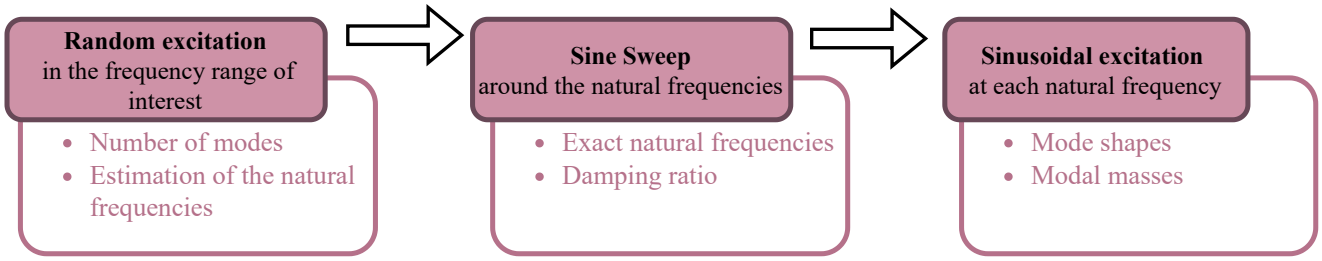

Figure 4.15: Modus Operandi of experimental tests when the shaker is used.

However, despite substantial efforts, the authorisation to conduct the tests with the shaker could not be obtained, and the campaign had to be revised. The force was thus induced by a group of people. The main purpose of the campaign remains unchanged: corroborate the model of the bridge, to conduct more tests numerically. The tests were split into different types of excitations:

1. **Random excitation**: a group of people walks on the deck of the bridge, unsynchronized, to generate a noise-like signal.
2. **Energetic Random excitation**: the group runs, triggering higher frequencies (range **[2.5 ; 4] Hz**).

3. **Synchronized walk**: all pedestrians walk at the same frequency. This allows to measure the acceleration of the bridge and to determine the possible need for a TMD if the accelerations are too high.

4. ***"Human-Shaker"***: all pedestrians act as a shaker inducing a sine wave at a chosen frequency. As they jump at that frequency, the accelerometers are moved around the bridge in order to determine the mode shape and the accelerations of the deck. An accelerometer attached to an individual of the group characterizes the signal.

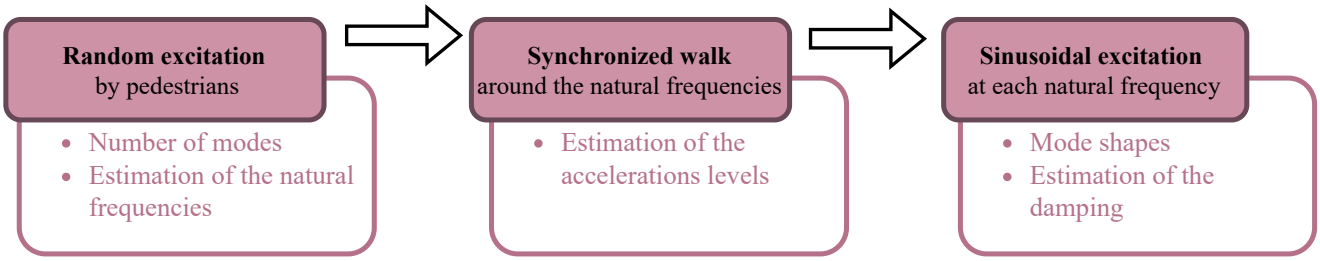

Figure 4.16: Modus Operandi of experimental tests when no shaker is used.

Unfortunately, during the on-site tests, due to an issue with the accelerometers, no data measured during the "Human-Shaker" tests was stored. This part will not be further investigated in this section; otherwise, the response would have been analysed with a deterministic periodic signal approach.

Equipment

Accelerometers are the only equipment used for the tests:

- 6 x *G-Link-200 wireless accelerometer*: triaxial waterproof accelerometers with a sensitivity of 1000 mV/g, meaning that for the tension levels in the batteries of the accelerometers, they can measure in a range of [-10 g ; 10 g]. This range is more than enough for the bridge, where the levels are not expected to exceed 0.15 g. The sampling frequency is set on 64 Hz, the measured frequencies can go up to $\frac{64}{2} = 32$ Hz (Nyquist frequency). Those accelerometers are set on the deck of the bridge, as shown in Figure 4.17 (a).

(a) *G-Link-200 wireless accelerometer*, used to measure the accelerations of the deck.

(b) *Gulf Coast Data Concepts MEL Logger*, used to measure the accelerations of the cables.

Figure 4.17: Two types of accelerometers used for the test campaign: Left - *G-Link-200 wireless accelerometer* & right - *Gulf Coast Data Concepts MEL Logger*.

- 3 x *Gulf Coast Data Concepts MEL Logger*: triaxial waterproof accelerometer. Their sensitivity is lower, as it can only measure in a range of [-2 g ; 2 g]. The sampling frequency was set on 256 Hz (128 Hz measured) and the accelerometers are attached to the cables with zip ties, as can be seen in Figure 4.17 (b).

Results of the campaign

Results of the random excitation campaign

During the test campaign, a random excitation allowed to compute the number of modes and to estimate their natural frequencies by performing a FT on the signal picked up by the accelerometers. Nevertheless, the signals can be further investigated by using the *COV-SSI* method, described earlier in this chapter. As excitation is generated by a group of people walking, the frequencies emerging from the range of the walk are spurious and cannot be considered. Consequently, the frequencies in the [1.7-2.1] Hz range are completely filtered out of the output signals. The results are cleaned from that frequency band to prevent the response to those frequencies from distorting the results.

Six accelerometers are placed on the structure, approximately every 16 m. Two sets of data are collected, one for each side of the bridge, to have a representation of the torsion in the mode shape results. The position of the accelerometers is represented in Figure 4.18. A span is 3.95 m long and the point of reference is the pylon (considered as x = 0 m); the sensors are placed at :

Sensor number.	1	2	3	4	5	6
Span number	4	7	12	16	20	25
Distance from pylon [m]	15.8	27.65	47.4	63.2	79	98.75

Table 4.1: Placement of the accelerometers on the deck of the bridge for the random excitation.

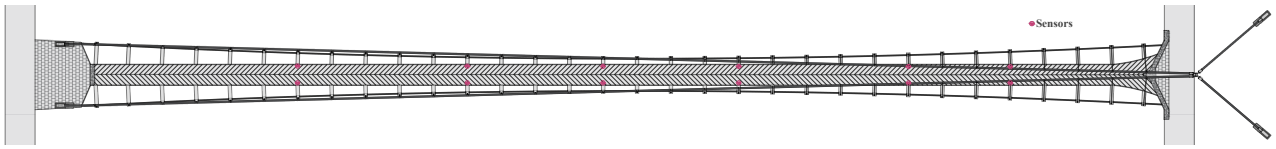

Figure 4.18: Position of the sensors for the random excitation.

1. **Fourier Transform of each separate signal**

   The FT of the raw signals can be compared with the FT of the signals where [1.7 ; 2.1] Hz is completely filtered out to prove that the filtering has a purpose. In addition, all frequencies above 5 Hz are filtered as well, to focus the results of the *SSI-COV* method on the frequencies targeted. As illustrated in Figure 4.19, the pedestrians' walking frequency range reveals signs of forced response. The range is entirely responding, and the peaks are higher than the other frequencies. The signal is therefore filtered to avoid contamination of the data when studied with a *COV-SSI* method. Figure 4.20 demonstrates that the peaks are more visible, as the forced response doesn't overwhelm the signal response. It is possible to identify a first set of eigenfrequencies that were considered a reference for the subsequent experimental tests, namely: 0.66 Hz, 0.7 Hz, 0.9 Hz, 1.1 Hz, 1.23 Hz, ... Figure 4.20 also shows different levels of excitation between the sensors, already suggesting the possible location for the nodes and anti-nodes for each eigenfrequencies of the bridge.

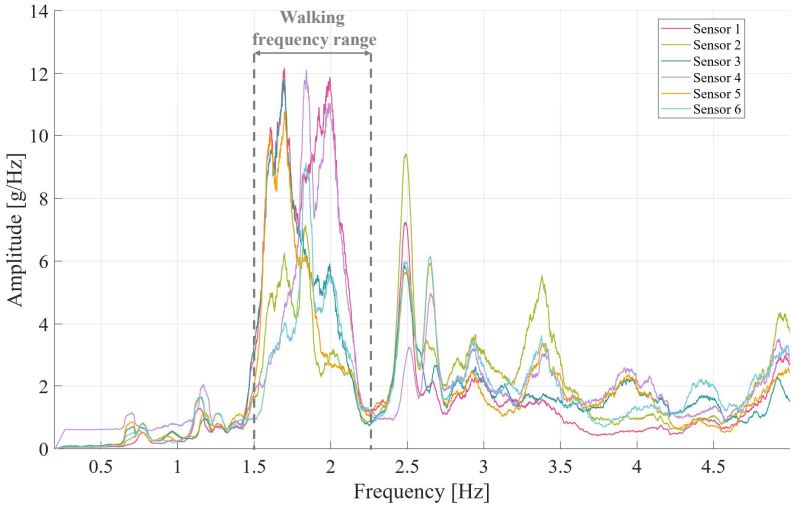

Figure 4.19: FT of the raw signals per accelerometer.

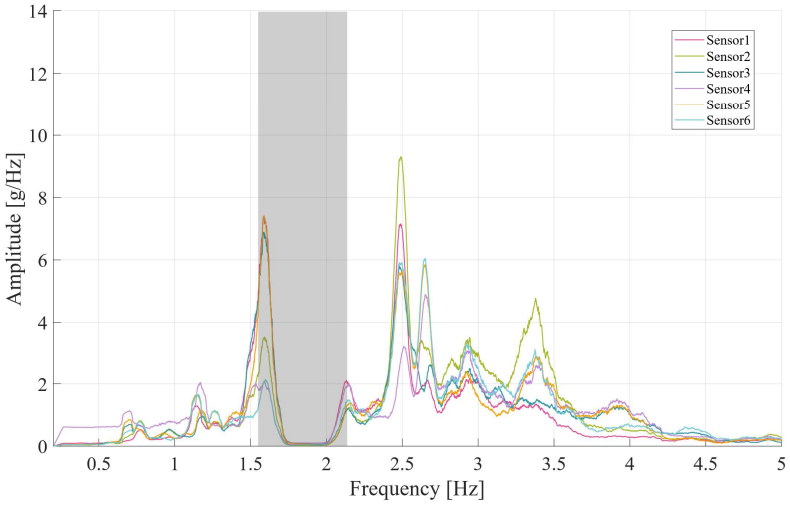

Figure 4.20: FT of the filtered signals: bandstop [1.7 - 2.1] Hz and 5+ Hz.

NB: The peak around 1.5 Hz is probably a remainder of the forced response, as the distribution of the walking frequencies is tri-linear (see Figure 4.21 (a), from the European design guide for footbridges (Service d'Etude Technique des Routes et Autoroutes (SETRA))).

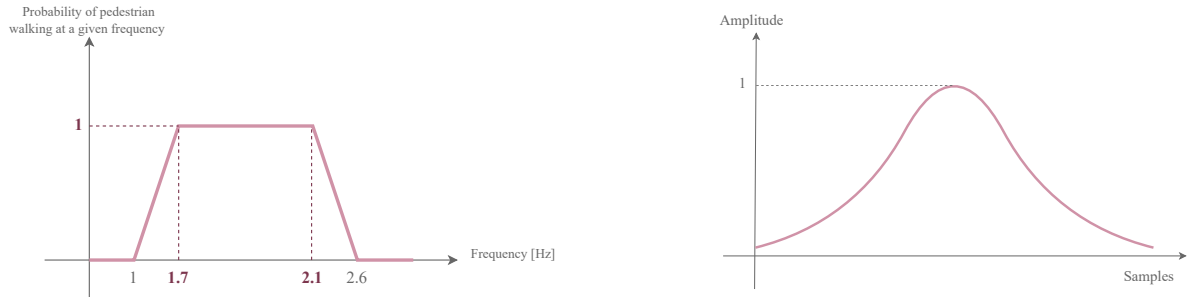

(a) Distribution of the probability of the frequency of pedestrians walking, from the *SETRA guide*.

(b) Schematics of the shape of a Hamming window used to filter the data.

Figure 4.21

Moreover, this peak can be caused by the type of window used to filter the frequencies. The window is a Hamming window and due to its shape, does not entirely filter out the extremum values of the range that has to be excluded. Figure 4.21 (b), representing the shape of a Hamming window, shows that the window isn't at full capacity for all the frequency range defined, and that can be the explanation for the frequencies peaks included in range [1.7 - 2.1] Hz in the FT.

2. **Stack the signals to supply data for the *COV-SSI* analysis**

   To compute the Toeplitz matrix based on the output covariance sequence, the data has to be re-arranged to fit the algorithm conditions. The signals from each accelerometer must be combined into an $n \times L$ matrix, n being the number of accelerometers and L the length of the signals, as shown in Figure 4.22.

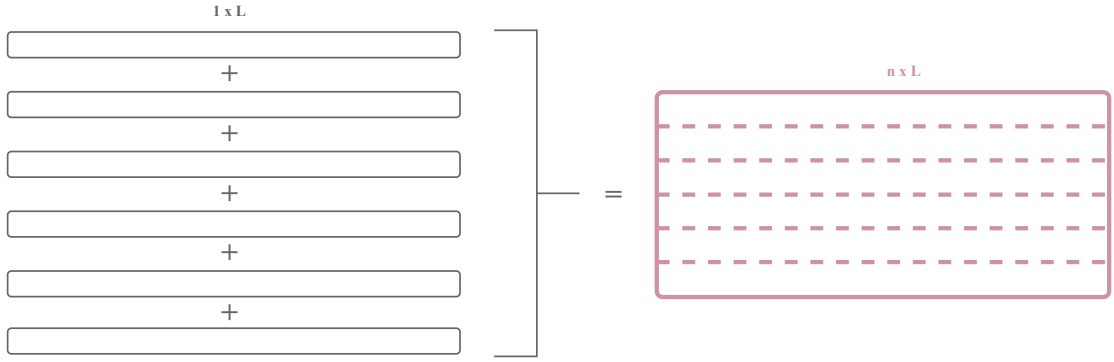

Figure 4.22: Combination of the accelerometers dataset into a matrix $n \times L$.

3. **Perform the *COV-SSI* analysis**

   The overall results of the analysis can be represented by a stabilization diagram, i.e. a plot of the stable poles versus the PSD of the signal. The modes that are considered stable can be further analysed with details of the mode shape and damping coefficient. The mode shape is only representative; only 6 accelerometers were placed on the whole length of the bridge.

4. **Stabilization diagrams**

   The poles of the stabilization diagrams are represented with different symbols, based on the type of computed stability:

   . New pole

   ⊕ Stable pole

   .v Pole stable in frequency and in shape

   .d Pole stable in frequency and in damping

   .f Pole stable in frequency

   The PSDs used in the stabilization diagrams are a combination of the six PSDs computed per sensor. This enables to have an overview of all responding frequencies. By doing this, a sensor placed in a node of a mode shape can be balanced by another one in an anti-node. It is computed as follows:

$$S_{global} = \left(\prod_{i=1}^{n} S_i \right)^{1/n} \tag{4.34}$$

Vertical modes

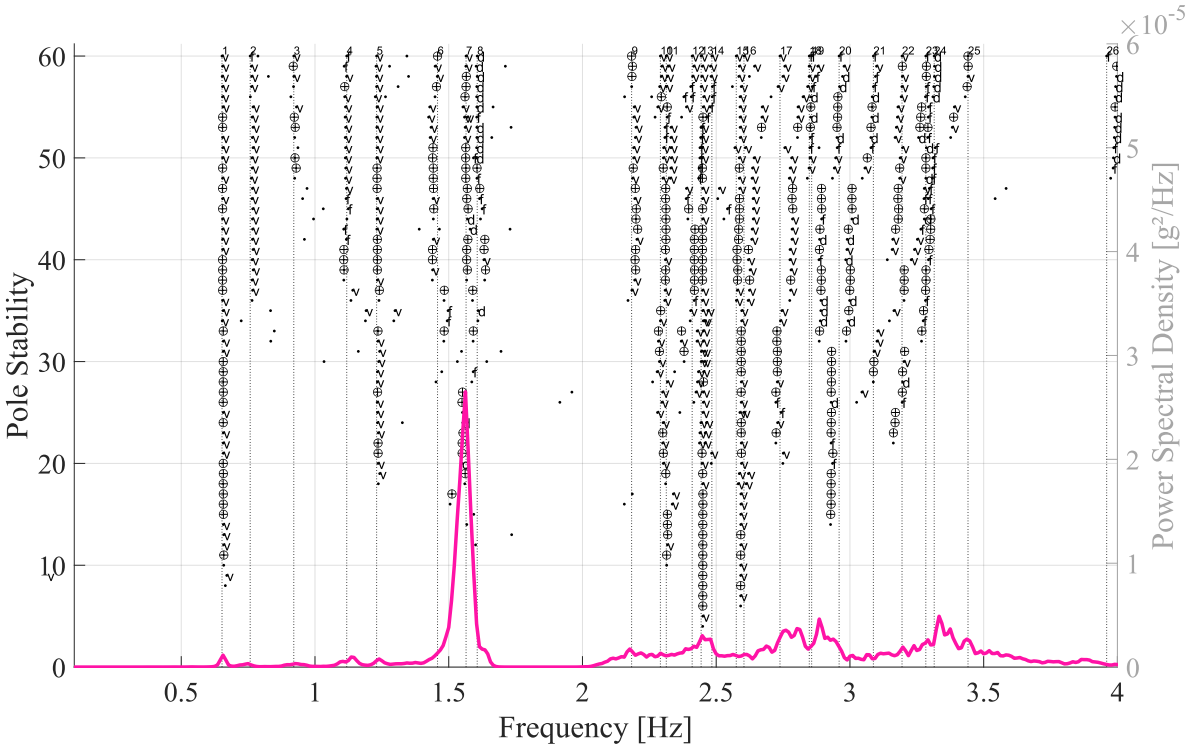

Figure 4.23: Stabilization diagram for the vertical modes for the right side of the bridge.

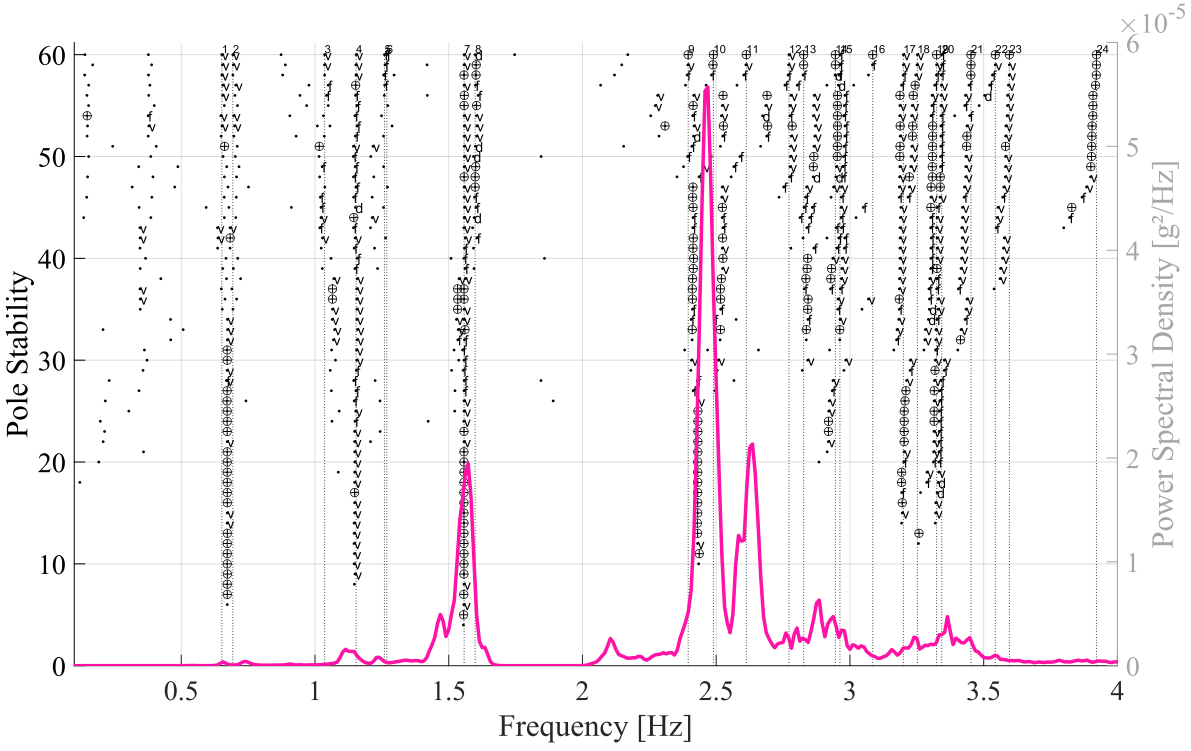

Figure 4.24: Stabilization diagram for the vertical modes for the left side of the bridge.

Computing the poles is a trade-off. The frequencies identified are not always the actual eigenfrequencies of the bridge, but numerical artefacts of the computations. For example, in Figure 4.24, the peak right before 1.5 Hz is not identified as an eigenfrequency. The first reaction is thus to increase the number of iterations of the algorithm. However, there is a risk of identifying spurious eigenfrequencies. It is important to either restrict the number of computed frequencies or to be careful in the results analysis. Often, the spurious frequencies are not stable in mode and in damping and do not match at all the peaks of the PSD superimposed to the poles diagram. When comparing the stabilization diagram of the left and right side of the bridge, the highlighted frequencies are fairly similar, with different amplitude levels, indicating possible torsion in the shape of the modes. Most poles identified are at least stable in frequency and damping or shape, but few are stable overall.

Figure 4.25 represents a superposition of the two PSDs of the left and right sides of the bridge, showing possible torsional modes as differences in amplification for the same frequencies can be noticed, as at 1.1 Hz.

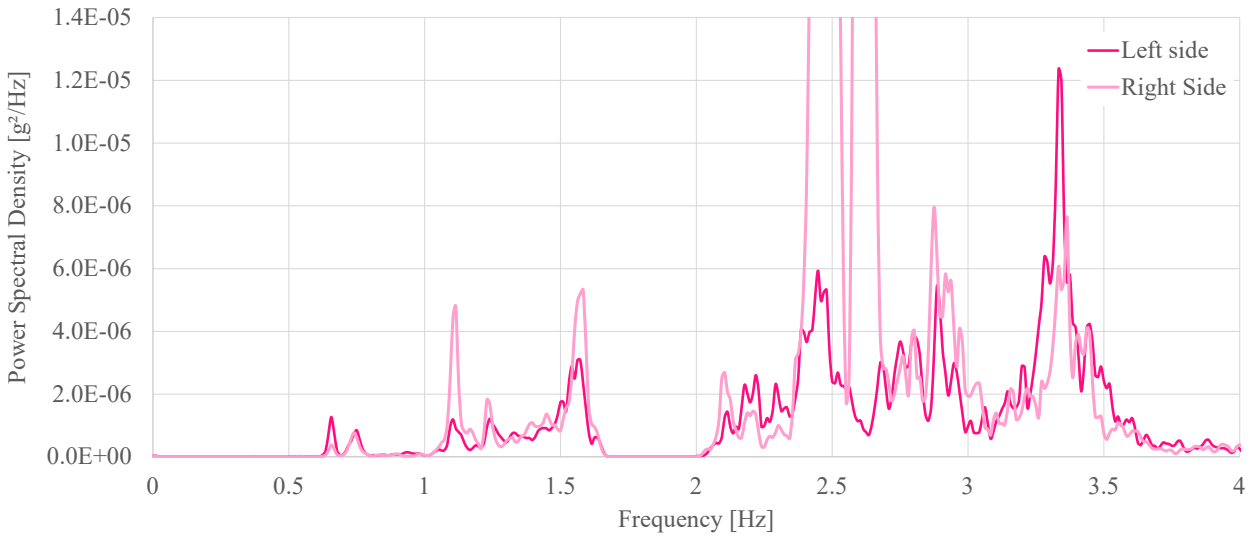

Figure 4.25: PSD of the left side versus PSD of the right side for the vertical modes.

Horizontal modes:

Regarding the stability of the horizontal modes, shown in Figures 4.26 and 4.27, two modes stand out: 0.5 Hz and 0.9 Hz, probably respectively the first and second horizontal modes. The others seem less important, but 1.1 Hz also stands out, suggesting a torsional mode working both horizontally and vertically.

Figure 4.28 shows the two PSDs according to the horizontal directions. In this graph, the torsion of frequency 1.1 Hz is well represented. However, the other modes do not seem to induce as much torsion as the vertical ones, as the PSDs match on most frequencies.

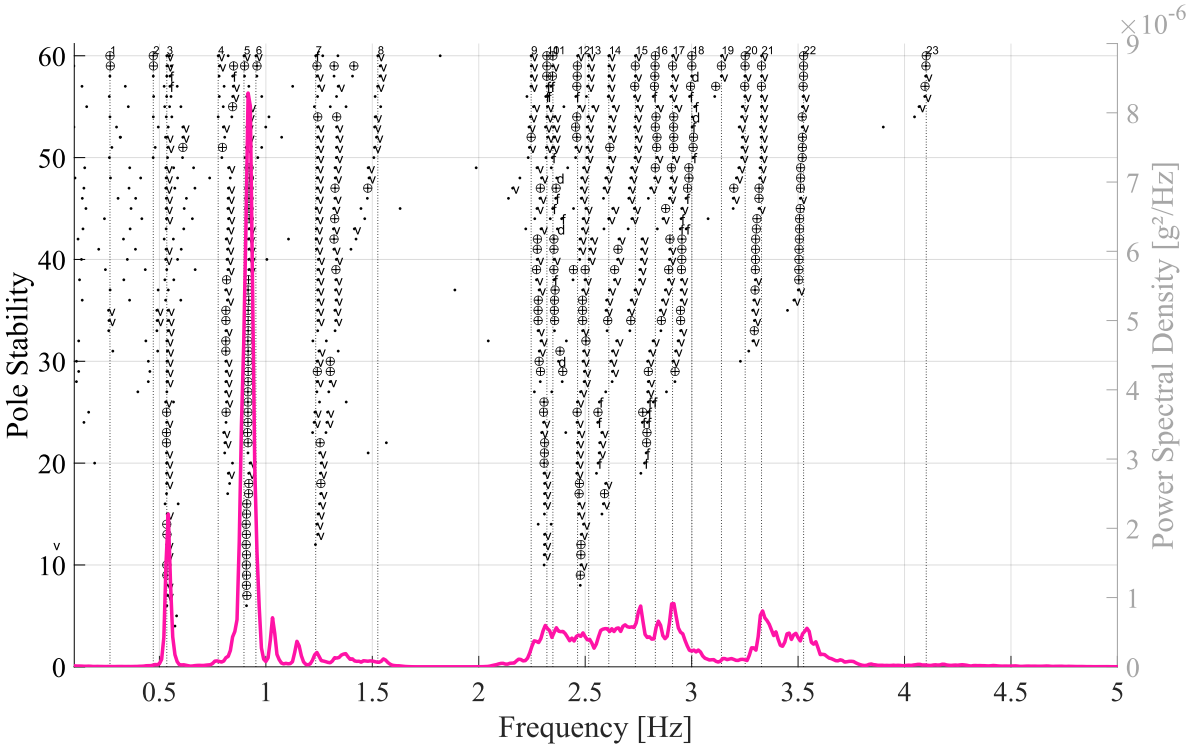

Figure 4.26: Stabilization diagram for the horizontal modes for the right side of the bridge.

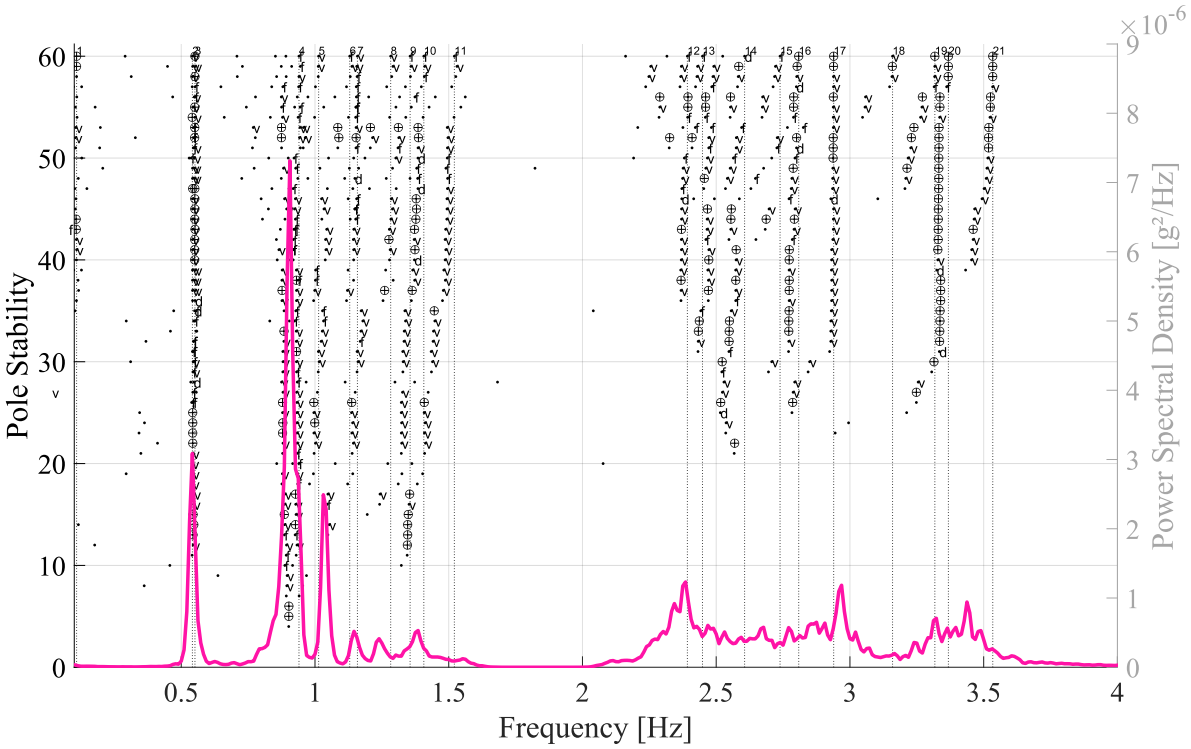

Figure 4.27: Stabilization diagram for the horizontal modes for the left side of the bridge.

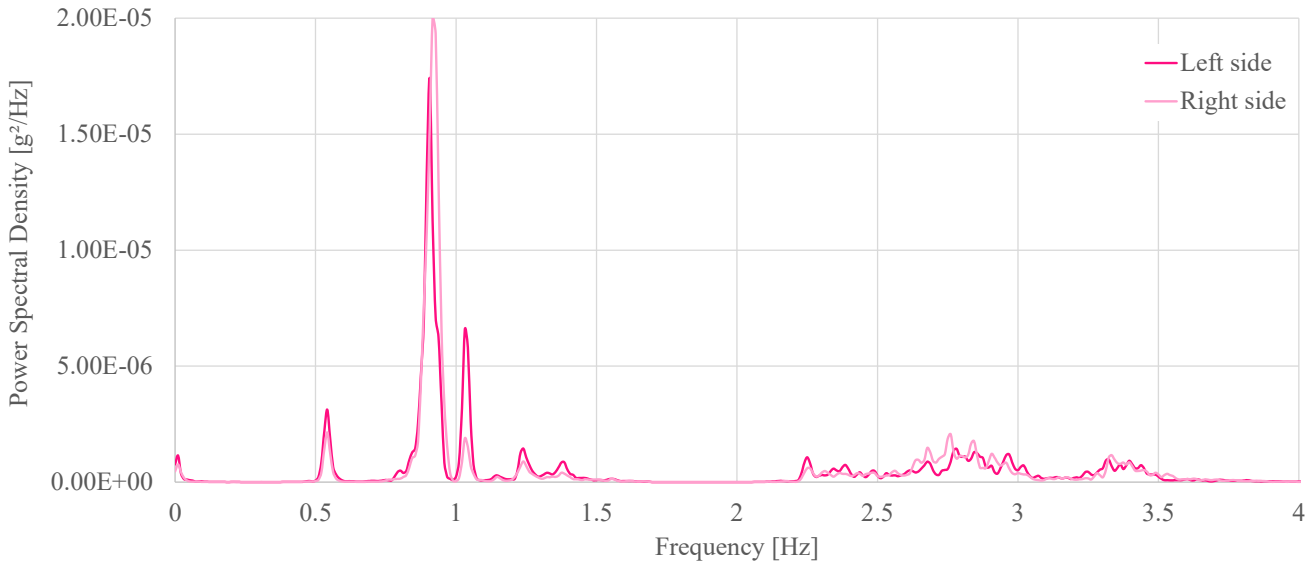

Figure 4.28: PSD of the left side versus PSD of the right side for the horizontal modes.

5. Final shapes of the modes

Vertical modes

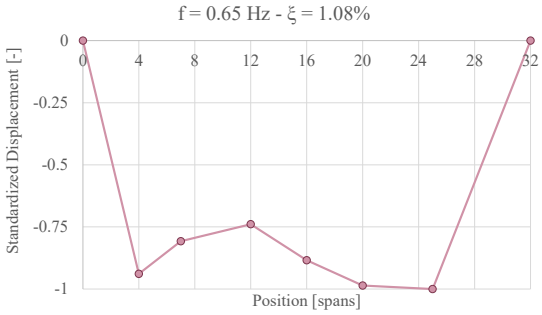

Figure 4.29: First vertical mode: 0.65 Hz.

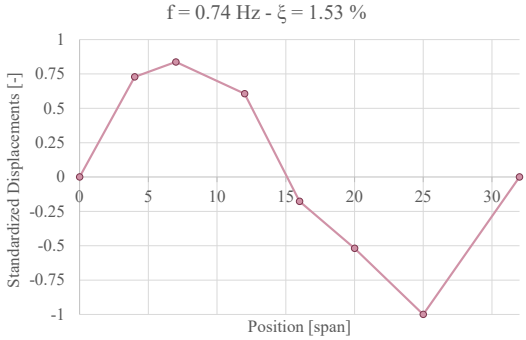

Figure 4.30: Second vertical mode: 0.74 Hz.

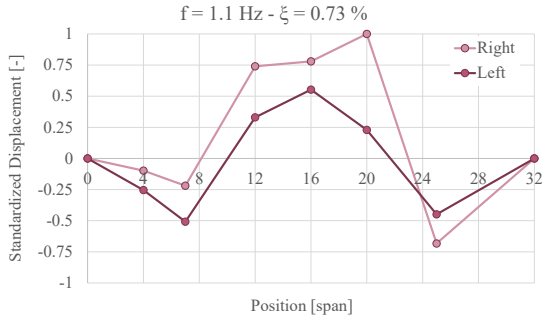

Figure 4.31: First mode of torsion: 1.1 Hz.

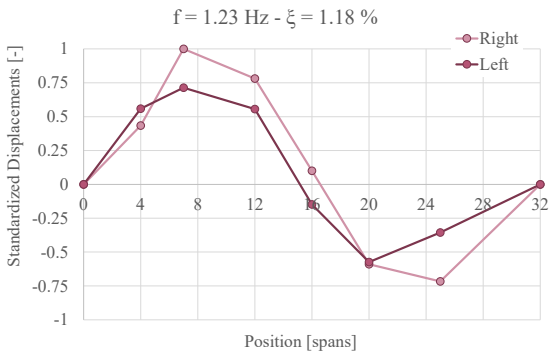

Figure 4.32: Second mode of torsion: 1.29 Hz.

This mode is the damped mode, according to the documents provided by *Cornelissen + Partners*. The effect of that damper is noticeable in the mode shape represented in Figure 4.29. Indeed, the first mode should be shaped as a half-sine wave but the nodes near the position of the TMD are closer to their initial position, showing the action of the TMD. The effect of the TMD is not at full capacity as displacement at 75 % of the maximal displacement remains around the position of the TMD. It might be caused by the difference between the identified eigenfrequency: 0.65 Hz and the frequency to which the TMD is tuned: 0.707 Hz.

Figure 4.30 represents the shape of the second vertical mode. The mode shape follows two half-sine waves, as expected. Figure 4.31 represents the first torsional mode. It is more or less shaped as half a sine wave, but the left and right sides do not reach the same displacements, representing the torsion of the bridge. This mode is the second mode of torsion. The difference of displacement between the left and right of the deck confirms this hypothesis. The global mode shape seems to follow the two half-sine wave shape. The documents provided by *Cornelissen + Partners* stated that two TMDs were designed especially to damp this mode. However, on site, no TMD was observed at the alleged location of those two dampers, while the TMD for the first vertical mode was clearly distinguishable. This and the mode shape resulting from the analysis seem to indicate that the TMDs were not placed on the footbridge. Following the experimental testing, the torsional TMDs were removed from the numerical model, as no evidence of their presence was found on site, even after visual inspection of the underside of the deck.

Horizontal modes

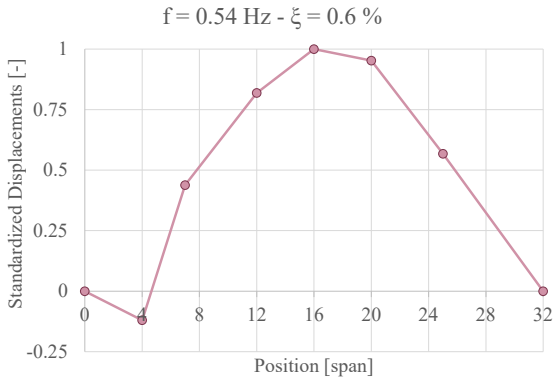

Figure 4.33: First horizontal mode: 0.54 Hz.

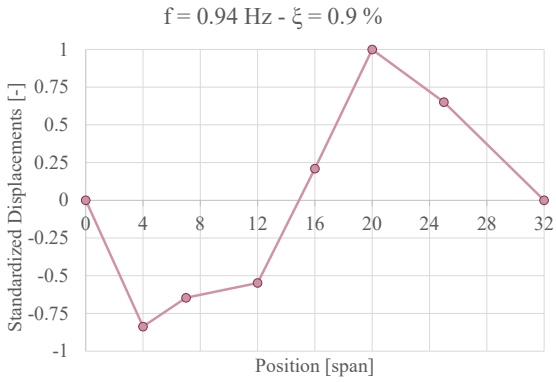

Figure 4.34: Second horizontal mode: 0.94 Hz.

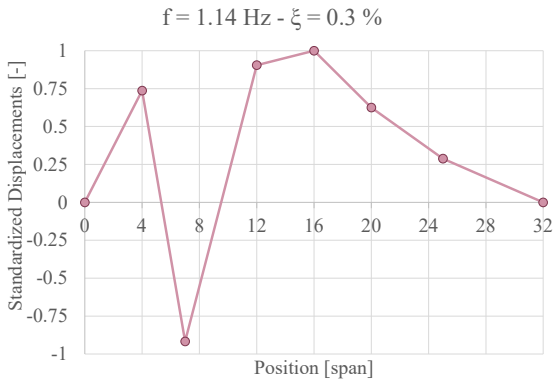

Figure 4.35: Third horizontal mode: 1.1 Hz.

Figure 4.33 shows the mode identified at the first eigenfrequency as the fundamental horizontal mode, as the deformed shape suggests a deformation following a half-sine shape. The same is valid for Figure 4.34, where it is possible to observe the double half-sine shape. The damping ratios of the horizontal modes are smaller than the vertical ones. This may be due to the cable. Indeed, for a cable of length ℓ, mobilized in its parallel direction, versus a cable mobilized in a perpendicular direction, by a displacement d:

$$N_{//} = N_{cable} \tag{4.35}$$

$$\text{for } d << \ell : N_{\perp} = N_{cable} \cdot \frac{d}{\ell} \tag{4.36}$$

$$\Rightarrow N_{//} > N_{\perp} \tag{4.37}$$

This set of equations shows that the resisting force to a parallel effort is bigger than to a perpendicular one. The stiffness is smaller horizontally, and, considering the damping as a combination of mass and stiffness (see *Rayleigh Damping*), the damping of horizontal modes will thus be smaller. The damping identified per mode is relatively large for a civil engineering structure. However, as the bridge was excited by pedestrians, their presence on the deck contributes to the global damping of the structure as well, leading to an identified damping ratio higher than usual (around 0.3 to 0.8 %).

Results of the *COV-SSI* for a random excitation generated by runners

This analysis provides insight into the frequencies that were previously removed from the signal. The running frequencies ([2.6 - 4] Hz) are filtered from the signal. This new configuration of the stabilization diagram, in Figure 4.36, highlights new frequencies, such as 1.13 Hz, 1.52 Hz (now confirmed as part of the eigenfrequencies, and not just a remainder of the filter), 1.97 Hz and 2.55 Hz. Again, the *COV-SSI* method gives a first idea of the mode shapes. When observing Figure 4.37 to 4.40, the modes seem to follow the continuity of the vertical modes previously identified, as the number of nodes and anti-nodes grows with the frequencies.

NB: It is important to remember that as there are only 6 accelerometers, high frequency modes with multiple peaks are harder to define. Caution is required when analysing the results.

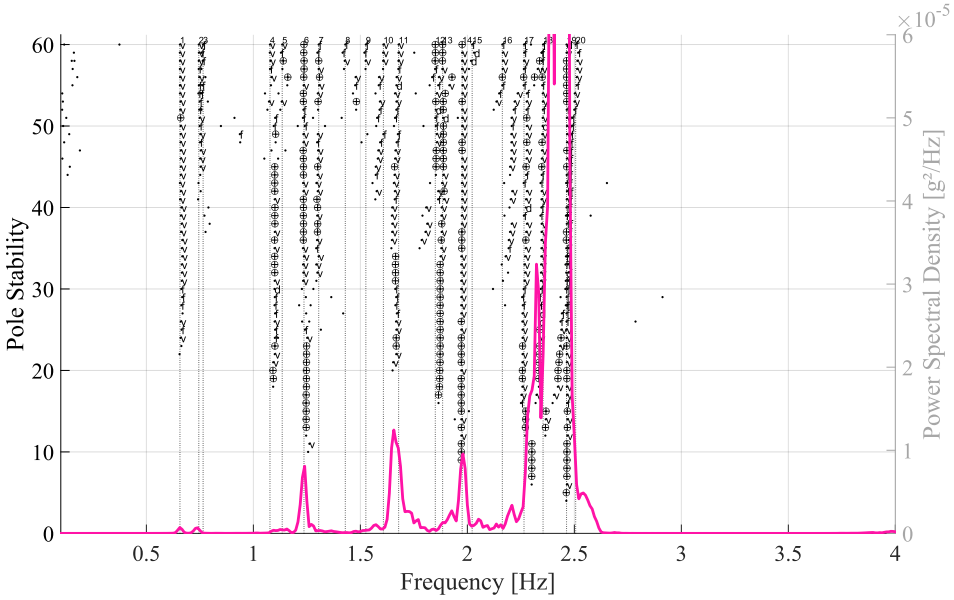

Figure 4.36: Stabilization diagram for the vertical modes for a running-type excitation.

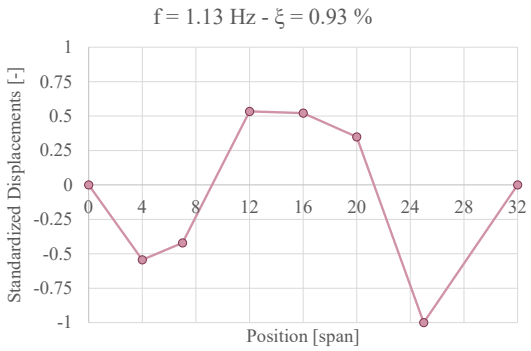

Figure 4.37: Third vertical mode: 1.52 Hz.

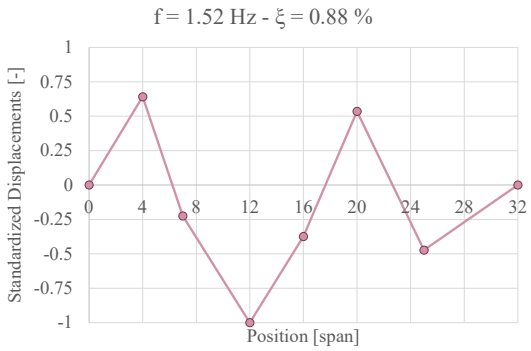

Figure 4.38: Fourth vertical mode: 1.81 Hz.

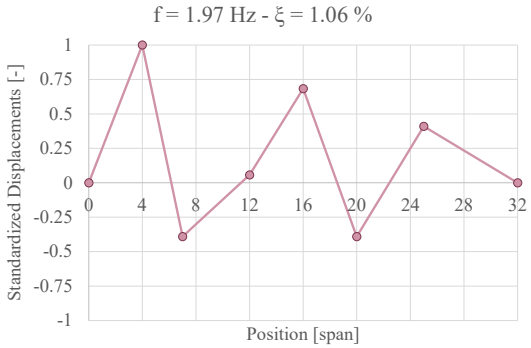

Figure 4.39: Sixth vertical mode: 1.97 Hz.

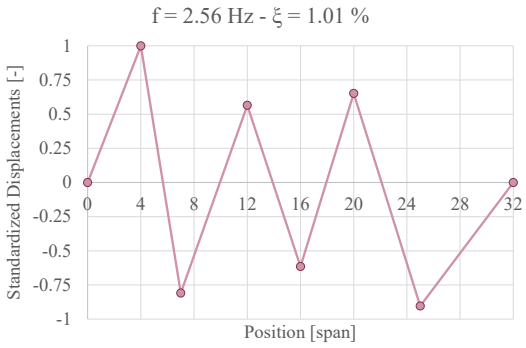

Figure 4.40: Sixth vertical mode: 1.97 Hz.

Acceleration levels

When performing the on-site testing, several frequencies stood out from the FTs. Synchronized walks were performed at those frequencies to capture the acceleration levels. To trigger the horizontal modes, the frequencies adopted are twice the identified horizontal frequency. A pedestrian walking at a frequency f induces a horizontal excitation at a frequency f/2 on the structure. The tested frequencies are:

1. 0.73 Hz: identified at that time as the first vertical mode, and supposedly the damped mode
2. 1.1 Hz: the first torsional mode
3. 1.23 Hz: the second torsional mode
4. 2 x 1.14 Hz: the third horizontal mode
5. 2 x 1.8 Hz

The *SETRA* guidelines for sizing footbridges against vibrations recommend ranges of frequency in which acceleration needs to be damped. Figures 4.41 and 4.42 represent the frequency ranges based on their likeliness to be triggered by pedestrians and Figure 4.43 and 4.44, the acceleration levels that have to be damped, based on the targeted level of comfort. The bridge is classified in class III: i.e. *a footbridge for standard use, that may occasionally be crossed by large groups of people but that will never be loaded throughout its bearing area*. In addition, as it is a suspended footbridge, the required comfort level is minimum, meaning that *under loading configurations that seldom occur, accelerations undergone by the structure are perceived by users, but do not become intolerable*. For that class and level of comfort, only the first acceleration range for critical frequencies has to be verified. Figures 4.41 and 4.42 illustrate

that the critical frequency range is between 1.7 Hz and 2.1 Hz for vertical modes, and 0.5 Hz and 1.1 Hz for horizontal modes (half the vertical frequencies). This means that the only important frequencies concerned by the guidelines are the walking frequencies, but the frequencies triggered by runners are not taken into account. As minimal comfort is targeted, Figures 4.43 and 4.44 show that the accelerations considered critical are between 1 and 2.5 m/s² for vertical modes and 0.3 to 0.8 m/s² for horizontal ones. However, Figure 4.44 highlights 0.1 m/s² as a limitation. This is often considered as the sole limitation for horizontal modes regardless of the range. Above that acceleration, pedestrians tend to start to synchronize with the rolling of the bridge and accentuate even more the acceleration levels. In order to have a better visualization of the results, the envelope of the positive accelerations is computed through a Hilbert transform.

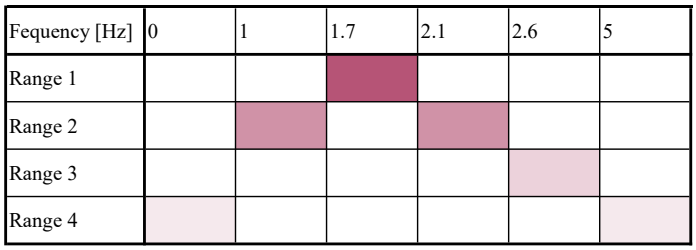

Figure 4.41: SETRA recommendations on ranges for vertical mode frequencies.

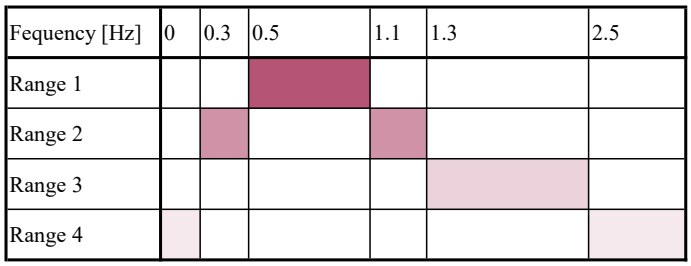

Figure 4.42: SETRA recommendations on ranges for horizontal mode frequencies.

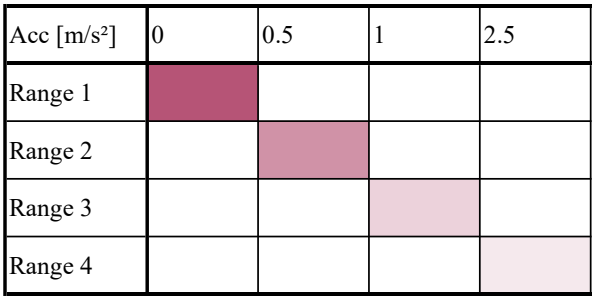

Figure 4.43: SETRA recommendations on accelerations for vertical modes.

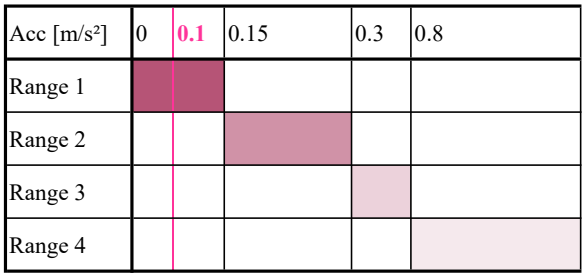

Figure 4.44: SETRA recommendations on accelerations for horizontal modes.

Vertical Accelerations

Figures 4.45 to 4.48 show the acceleration levels generated in the bridge for different frequencies. The accelerations of the first modes (0.73 to 1.23 Hz) are within the acceptable limits for a class III footbridge, as they all remain below 0.2 m/s². Even with a modified bridge class, the acceleration would be low enough for a class I. However, the accelerations detected for a mode with a higher frequency, 2.28 Hz, are above the prescribed value of 1 m/s². Due to the class of the footbridge, the frequency is not in the critical range, but this can be disturbing for runners, and would have to be investigated further in the eventuality of the organisation of a race or trail in the park.

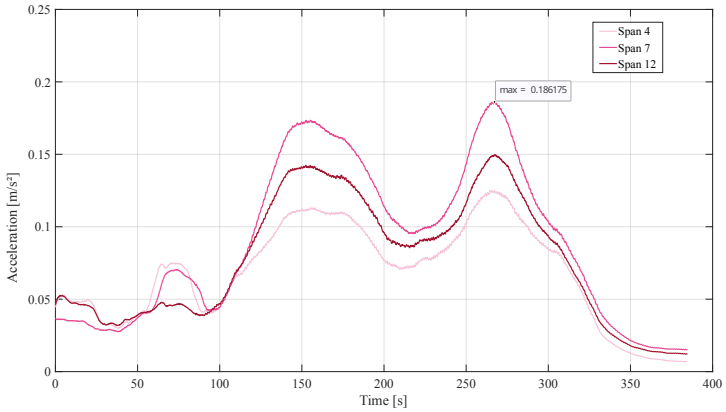

Figure 4.45: Envelope of the positive accelerations for frequency 0.73 Hz - First vertical mode.

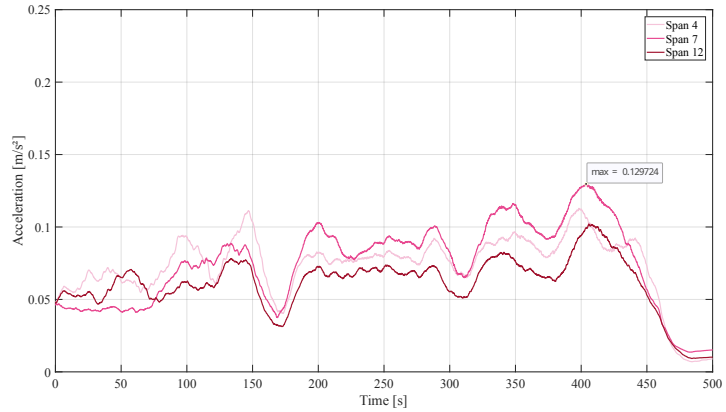

Figure 4.46: Envelope of the positive accelerations for frequency 1.1 Hz - First torsional mode.

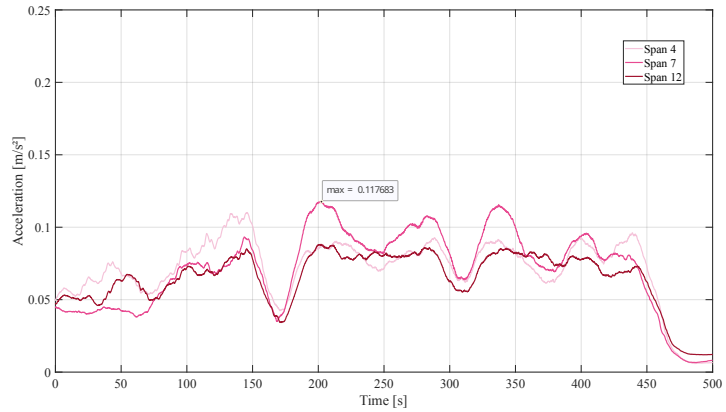

Figure 4.47: Envelope of the positive accelerations for frequency 1.23 Hz - Second torsional mode.

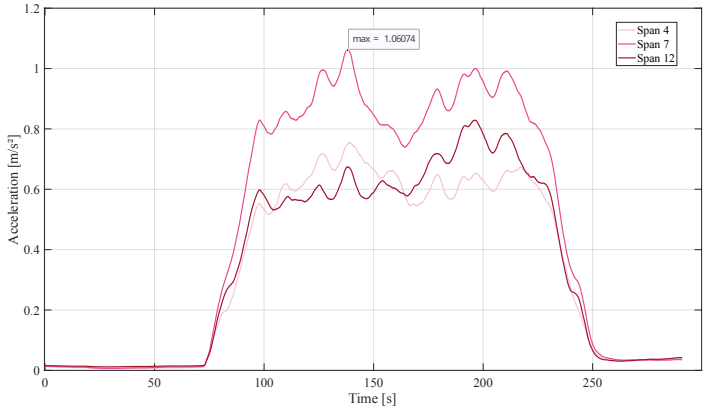

Figure 4.48: Envelope of the positive accelerations for frequency 2.28 Hz (2x1.14 Hz) - third horizontal mode.

Horizontal Accelerations

Figure 4.49 shows that the maximal acceleration for the horizontal mode tested is around 0.15 m/s², which is above the limit set at 0.1 Hz. If that criterion is disregarded in favour of the original criterion set at 0.3 m/s² for class III bridges, the acceleration levels are considered acceptable for that frequency.

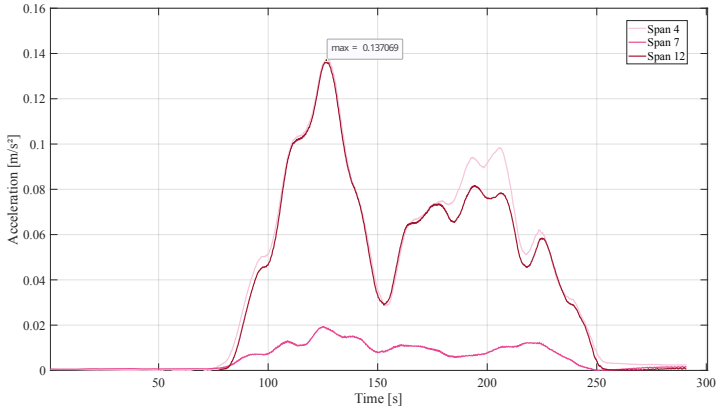

Figure 4.49: Envelope of the positive accelerations for frequency 1.14 Hz - Third horizontal mode.

Excitation of the hangers

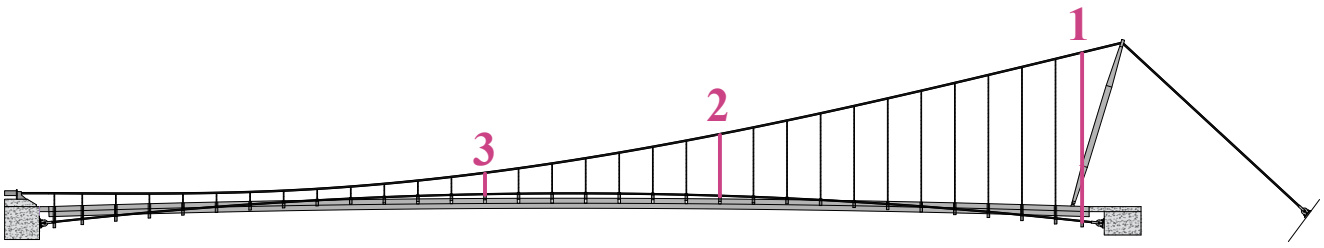

Figure 4.50: Schematics of the elevation of the bridge, with the tested hangers highlighted.

Three hangers were tested in order to characterize the tension in each hanger. The hangers are not all at the same horizontal distance from the deck due to the specific shape of the cross beams. Therefore, all

cables do not have the same level of accessibility, and so, the hangers tested were the easiest to reach. During the on-site visit, the longest hangers seemed to be loose and not perfectly taut. This could impact the tension distribution in the hangers compared to the computation of the numerical model. The location of the hangers tested is represented schematically in Figure 4.50, and their characteristics are detailed in Table 4.2.

	1	2	3
Span n°	1	12	19
Length [m]	19.16	6.75	2.55
Linear mass [kg/m]	1.475		

Table 4.2: Characteristics of the tested hangers.

Before analysing the results from the test campaign, the tension borne in each hanger can be estimated, based on the following assumptions:

- Each hanger carries the weight of half a hanger spacing, on both sides of the hanger (Figure 4.51)
- There are two longitudinal rows of hangers
- The deck contributes to half of the total weight of the bridge

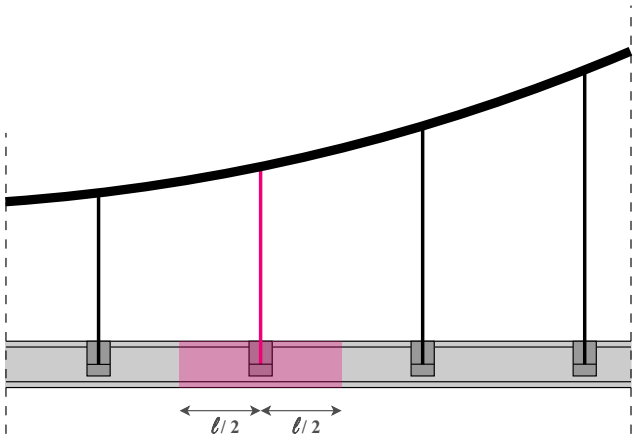

Figure 4.51: Schematics of the weight supported by each hanger, in elevation.

It is possible to compute

$$m_{tot} = 118{,}150 \text{ kg (from numerical model)} \tag{4.38}$$

$$m_{deck} \simeq 59{,}000 \text{ kg} \rightarrow G_{deck} = 590{,}000 \text{ N} \tag{4.39}$$

$$g_{deck} = \frac{G_{deck}}{L_{deck}} = \frac{590{,}000}{120} \simeq 5000 \text{ N/m} \tag{4.40}$$

$$T_{hanger} = \frac{1}{2} \cdot g_{deck} \cdot \frac{\ell}{2} \cdot 2 = 10 \text{ kN} \tag{4.41}$$

Each hanger is supposed to bear around 10 kN in tension. However, due to the loosening of some cables, that value can change, but it cannot be drastically different.

The analysis performed to determine the tension in the hangers is similar to the analysis performed under

a Dirac-like function, as the impact is as brief as possible. However, the impact level is unknown. It is still possible to compute the FT of the free response of the cable, in order to determine the predominant modes. For a Dirac-like function, all frequencies are triggered at the same time, so several frequencies peak in the FT, corresponding to multiples of the first frequency (fundamental mode) of the hanger. In addition, when the cables are long, it is not always possible to impact them in their centre, the location of the anti-node of the first mode (half-sine wave). The impact position can result in a higher frequency predominating in the FT over the first frequency.

- *hanger 1 - 19.16 m* :

  The FT of the response of cable 1 is relatively clear. The eigenfrequencies stand out and are more or less proportional. In this case, frequency 5.8 Hz seems to impose itself as the first eigenfrequency of the hanger.

  NB: The bending stiffness and the flexibility of the supports (deck and suspension cables able to move), both usually not taken into account when computing the eigenfrequencies of a cable, induce variation in the proportion ratio between the first frequency and the others [6].

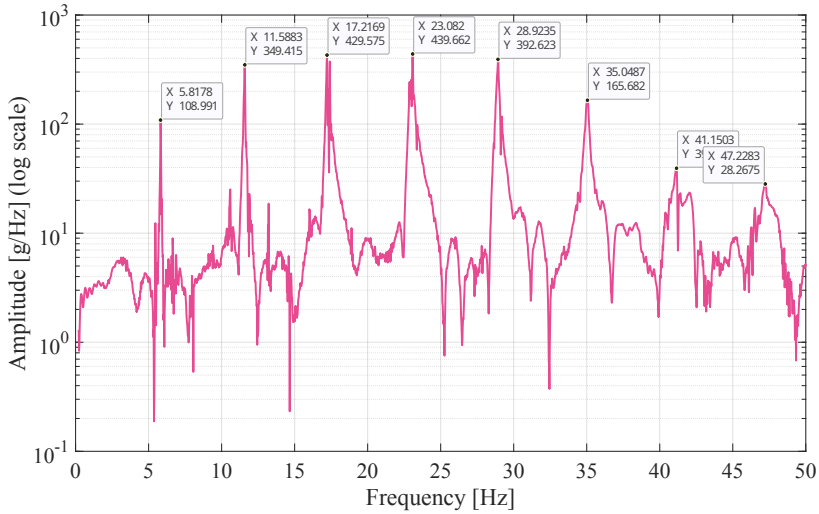

Figure 4.52: Fourier Transform of the free response of hanger 1, in logarithmic scale.

- *hanger 2 - 6.75 m* :

  The analysis of Fourier transform of cable 2 is more complex than the first. Indeed, at first sight, 15.7 Hz seems to be the first eigenfrequency. However, this value expresses a very high tension in the hanger, much more significant than the tension estimated earlier. As the hanger is 6.7 m long, it might be possible that, when raising one's arm for the impact, taking into account the horizontal distance from the railing, the impact was closer to the anti-node of the second mode (at 2.23 m high). In this case, the second mode predominates in the response and the FT. Smaller responses can still be distinguished around 7.9 Hz and 21.7 Hz, pointing towards a first eigenfrequency at 7.9 Hz and not 15.7. A first eigenfrequency at 15.7 Hz results in a tension of 66 kN in the hanger. This seems highly unlikely, even if there is a redistribution of efforts due to the loosening of some hangers as the estimated tension was around 10 kN.

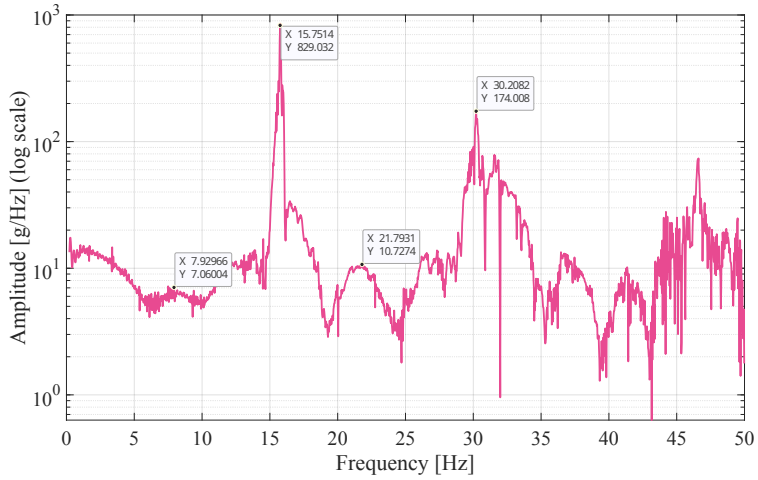

Figure 4.53: Fourier Transform of the free response of hanger 2, in logarithmic scale.

- *hanger 3 - 2.55 m* :

  Hanger 3 seems to have a much higher eigenfrequency than the other two. However, it is much shorter than the others, therefore, to bear sufficient tension and reach at least 10 kN, the hanger must have a bigger first eigenfrequency.

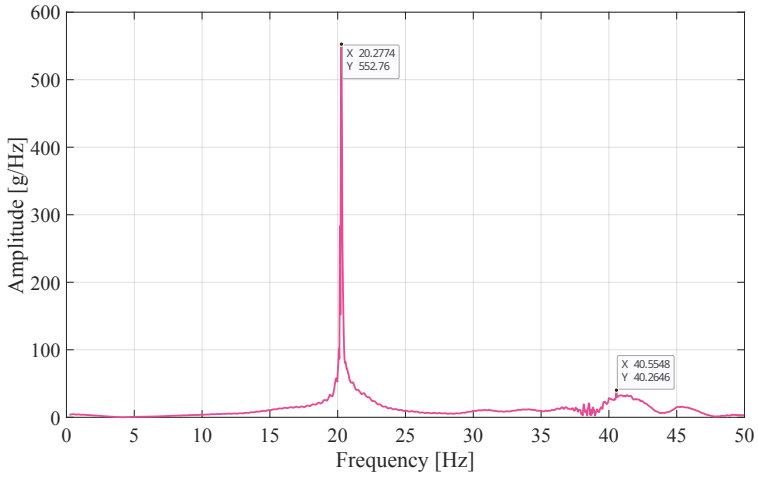

Figure 4.54: Fourier Transform of the free response of hanger 3.

Results of the analysis

The results of the computation of the tension per hanger are presented in Table 4.3 below. The formula to compute the tension in a cable is the following:

$$f = \frac{1}{2 \cdot \ell} \cdot \sqrt{\frac{T}{\mu}} \Leftrightarrow T = (f \cdot 2 \cdot \ell)^2 \cdot \mu \tag{4.42}$$

With f, the first eigenfrequency of the cable; ℓ, the length of the cable; T, the tension in the cable and μ, the linear mass of the cable.

	1	2	3
Length [m]	19.16	6.75	2.55
Linear mass [kg/m]	1.475		
Identified eigenfrequency [Hz]	5.8	7.9	20.3
Tension [kN]	72.8	16.7	15.8
Tension/m [kN/m]	3.8	2.5	6.2

Table 4.3: Data and results of the computation of the tension in selected hangers.

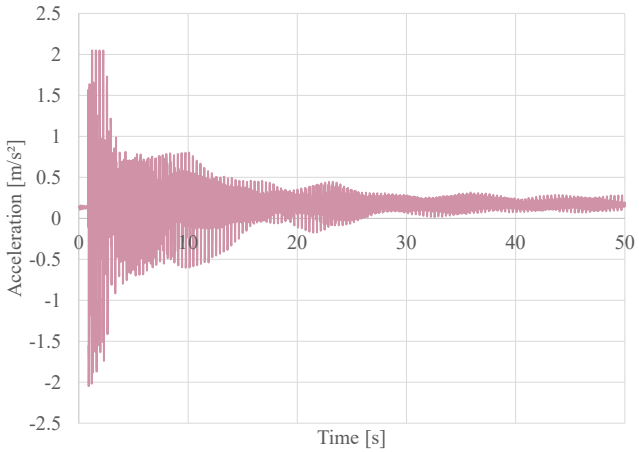

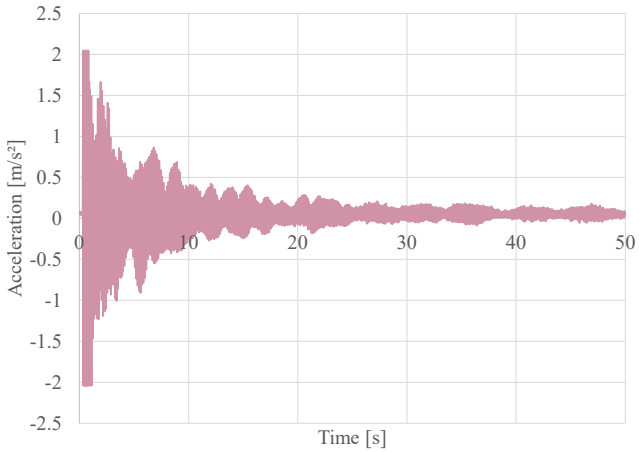

(a) free response of hanger 1: acceleration based on time. (b) free response of hanger 2: acceleration based on time.

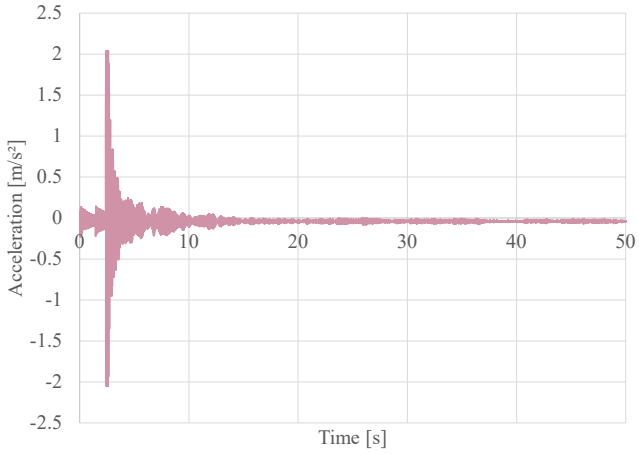

(c) free response of hanger 3: acceleration based on time.

Figure 4.55: free response of the three hangers tested.

A hypothesis regarding the tension distribution in the hangers is made. The middle hangers bear relatively similar tension, whereas those closer to the supports carry more tension. Though, when checking the tension per meter in each hanger (see Table 4.3), the third hanger undergoes the largest tension per meter. This effect is noticeable in the raw free responses of the hangers. Figure 4.55 (a) and (b), representing the free response of hanger 1 and 2, appear more clouded by parasite modes: the decay of the signals is no longer modulated by a single decreasing exponential and other modes have a greater impact on the response, compared to hanger 3 in Figure 4.55 (c), whose signal is cleaner. It might be due to the impact, more centred, as hanger 3 is only 2.55 m long, but also to the cable being more tensed, and thus, reducing the interference effect between modes. The more distended the cable, the less periodic the

signal. This leads to detuned harmonics (the harmonics are no longer perfectly proportional), making them harder to identify. This might be another explanation behind the shape of the FT of hanger 2, in Figure 4.53, the hanger with the less tension per meter of the three hangers that have been tested.

Figure 4.56 represents the estimated tension distribution in the hangers, based on the results of the experimental campaign.

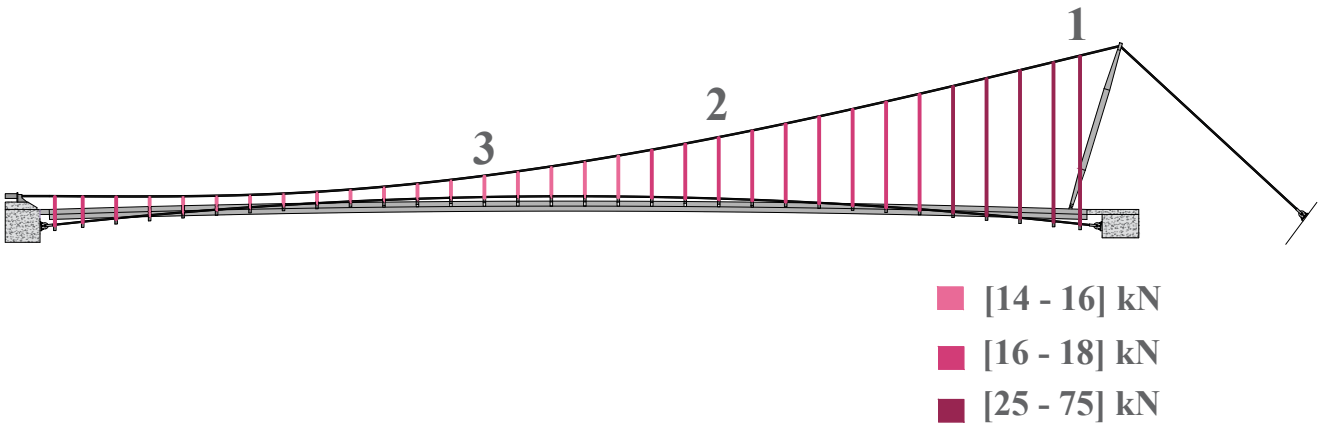

Figure 4.56: Estimation of the tension distribution in all the hangers of the bridge, based on the experimental campaign completed on three hangers.

4.3 Conclusion of the experimental campaign

In conclusion, experimental testing is really useful to characterize the actual behaviour of the bridge. This campaign gave an estimate of the eigenfrequencies of the bridge, as well as the mode shapes corresponding to those frequencies. The acceleration levels were determined for a few modes and can be compared to the values of the *SETRA* guide for sizing footbridges against vibrations. In most cases, the acceleration levels of the tested modes did not exceed the values expected for a class III footbridge with minimal comfort. However, some frequencies, such as 1.14 Hz for the horizontal mode and 2.28 Hz for the vertical ones, still have non-negligible acceleration levels. Further investigations on the higher modes triggered by running have to be planned in the perspective of the organization of a race or a trail.

During the on-site visit, a visual inspection enabled a comparison between the real footbridge and the drawings provided by *Cornelissen + Partners*, that highlighted two major differences:

- The TMDs against torsion do not appear to be have been installed
- The main central beam, expected to be a IPE 240 welded to a double angle section is just a simple IPE 240

In addition, the analysis of the data enlightens an unexpected phenomenon: some hangers are distended and thus, the tension distribution in the bridge is probably different from what is expected with the non-linear static analysis of the numerical model.

5 Numerical Model

The main challenge of this work is to build a numerical model of the footbridge that reproduces as accurately as possible the real-life behaviour of the bridge. To this end, particular attention had to be brought to the dimensions and material of the bridge. This was possible thanks to the drawings provided by courtesy of the engineering office *Cornelissen + Partners*. Furthermore, the findings of the experimental campaign enabled to adjust the model to the real-life behaviour. The software used to build this model, `Finelg`, was developed by the engineering office *Greisch* in collaboration with the University of Liège.

This section includes a description of the model (geometry, material, ...), a presentation of the main issues to resolve before starting the computations, and a summary of the various types of analyses performed in order to have accurate results for the final computations. The issues are mostly related to the definition of the cables of the model. In `Finelg`, cable elements only possess longitudinal stiffness but no lateral stiffness. This means that once they are horizontally shifted from their initial position, no rigidity can counteract that displacement, and thus, the model cannot converge to a realistic solution. The analyses include a static analysis to represent the deformation of the bridge under its own self-weight, a modal analysis to represent the eigenfrequencies, eigenmodes and modal characteristics of the bridge and then, a step-by-step dynamic analysis, to study the dynamic behaviour of the bridge under varying load.

5.1 Description of the numerical model

The numerical model is based on a collection of drawings and technical sheets. Figure 5.3 represents a simplified diagram of the bridge that shows the main components of the bridge and their material. The bridge is entirely made of steel, with the exception of the decking surface, made of aluminium plates. However, the steel grade varies based on the element of the model. The longitudinal beams and the cross beams of the deck are made of S235 steel, whereas the pylon is made of hollow tubes of S355 steel. The pylon is composed on both ends of two cones going from a diameter of 350 mm to a diameter of 700 mm, with a 700 mm diameter cylinder in the middle. Elements of varying section are not available in `Finelg`, so the cones are split into four cylinders of increasing diameter, as can be seen in Figure 5.3, in yellow.

The main cable, bottom cable and back cables (in purple and blue in Figure 5.3) are referenced as *Locked cables of type VVS-1* whereas the hangers are defined as *Open-Spiral Strand (OSS)*. Both are made of galvanized high-strength steel round wires that are spun from both ends in different directions around a central core. The locked cables are also protected by an outer layer of intricate z-shaped wires that shields the core from external aggression, such as rain water. The difference between the types of cable is illustrated in Figure 5.1. The modulus of elasticity is lower than for common steel - 160 GPa instead of the classic 210 GPa - as expected for high-strength steel.

One specificity of the deck of the bridge lies in the main longitudinal beams. They are composed of an IPE 240 beam, with a rail track beam welded on the lower flange. To simplify the model, an IPE section with equivalent inertia in its main direction is used to represent that composite beam. Thus, an IPE 360

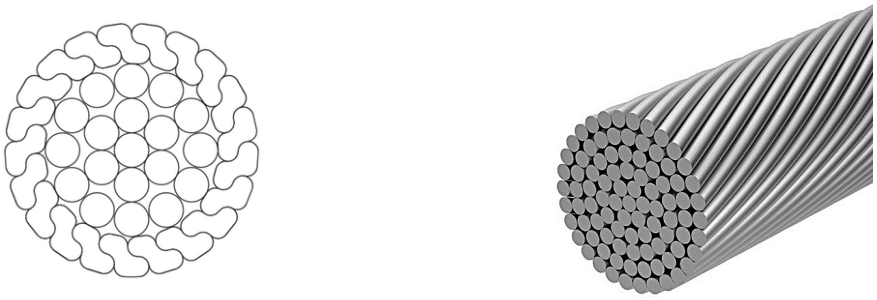

(a) Cross section of a locked cable type VVS
Source: Pfeifer

(b) Cross-section of a open spiral strand cable
Source: Teufelberger-Redaelli.

Figure 5.1: Two types of cables cross-section used in the model.

replaces an IPE 240 on top of a L-section of 200 x 100 x 10 mm. The cross-beams are also simplified. They are supposed to be beams with varying height, going from 270 to 210 mm, as illustrated in Figure 5.2 (a). It was decided to model them as IPE 270 over their whole length, to ensure continuity in the cross beams. The shape of the numerical cross-beams is illustrated in 5.2 (b).

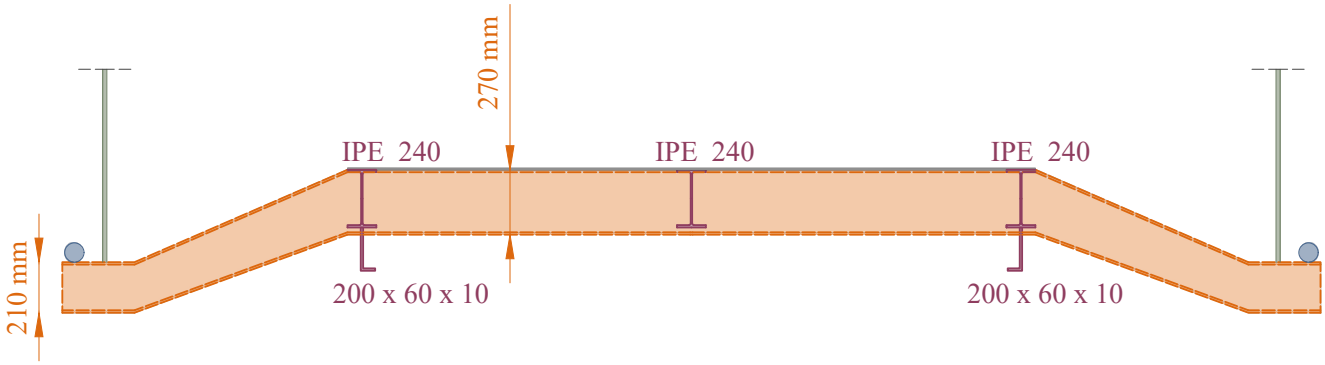

(a) Example of an actual cross-section of the bridge.

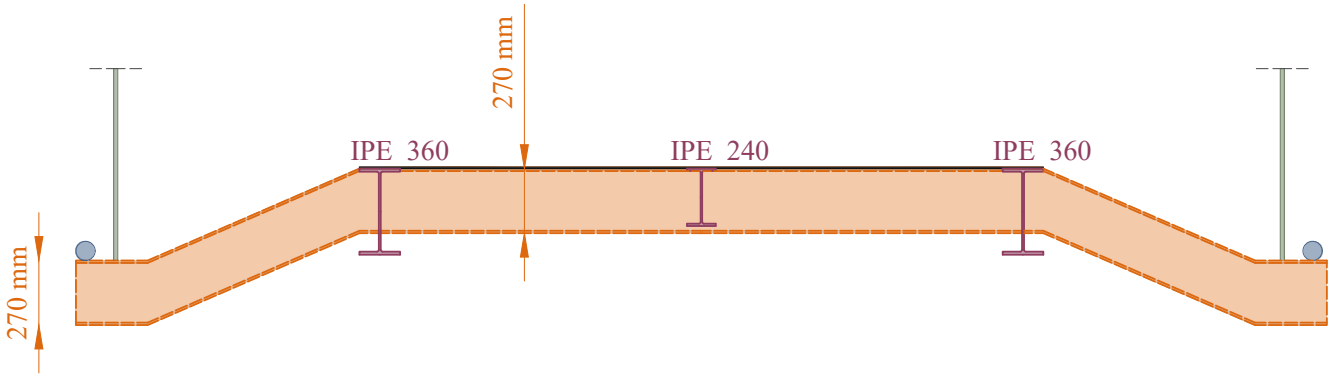

(b) Example of a simplified cross-section of the bridge, used in the numerical model.

Figure 5.2: Example of the simplification of the cross-section of the bridge in the numerical model.

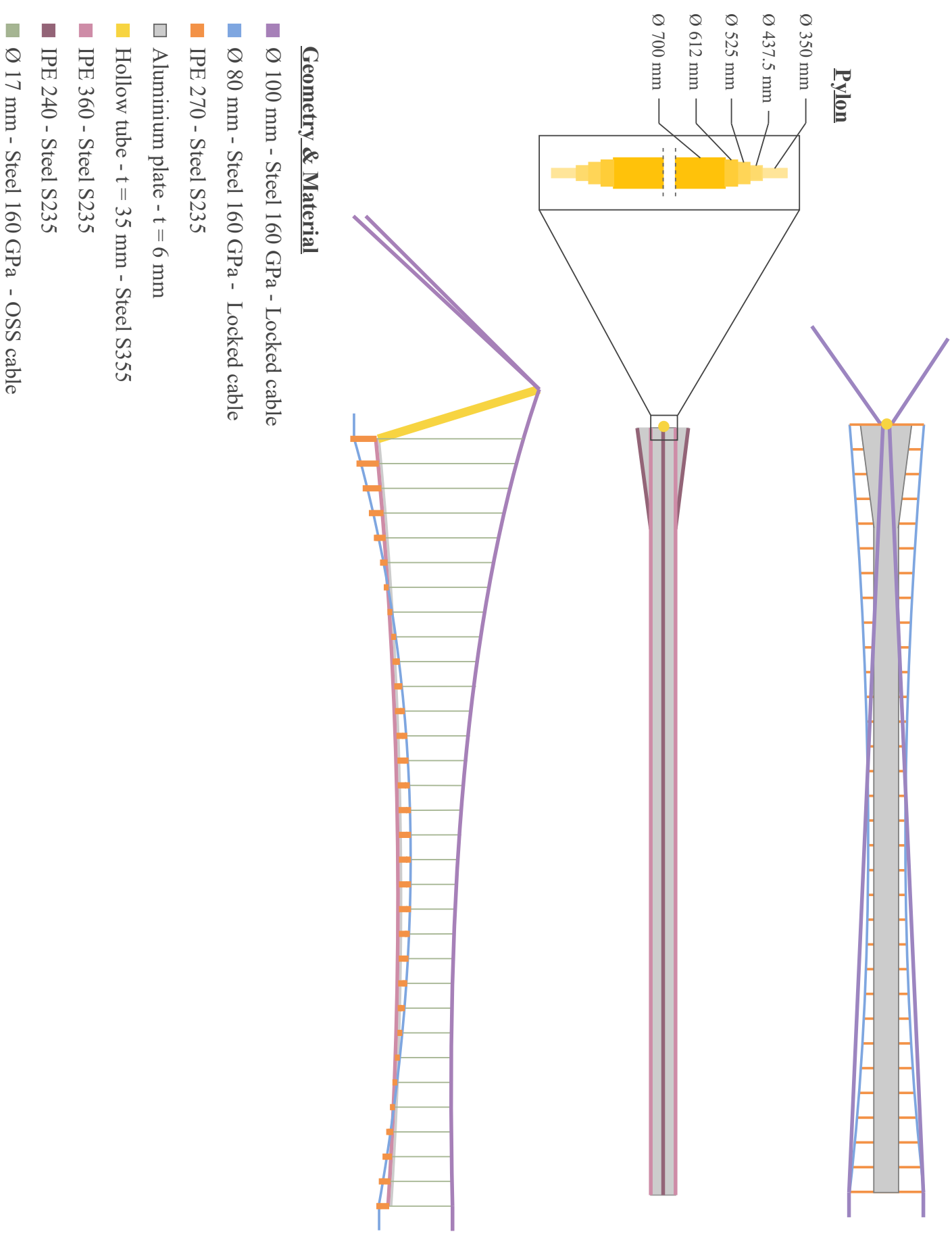

Figure 5.3: Simplified diagram representing the geometries and material used for the numerical model of the Victor-Neels bridge on a plan view and a longitudinal view.

5.2 Cable elements

Lateral stiffness

The cables are very sensitive items in `Finelg`, and require particular attention. They are represented by **rods**, designed to resist only axial loading in a linear analysis. This means they do not have any transversal stiffness. Though it does exist in real-life and is the product of inherent non-linearities in cable elements. From a finite elements perspective, as illustrated in Figure 5.4, the internal efforts N of a cable element subjected to a lateral load depend on the displacement of both sub-elements of the cable, i.e. $N = N(u_1, u_2)$. This dependency on the displacement makes the problem non-linear and is not considered in linear analysis. The stiffness matrix of a cable can be divided into two sub-matrices, $\mathbf{K}_0$, representing the linear axial behaviour and $\mathbf{K}_\sigma$, representing the non-linear behaviour, and are not taken into account in linear analysis.

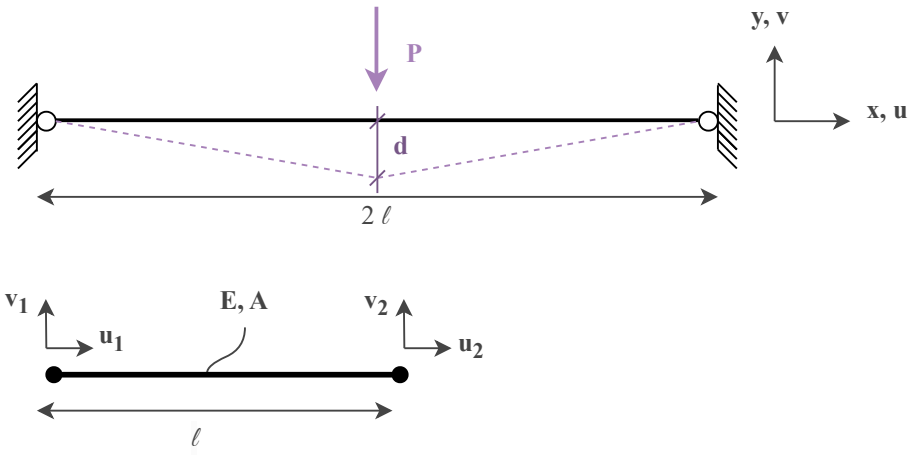

Figure 5.4: FE representation of a rod in `Finelg`.

$$\mathbf{K}_{cable} \cdot \underline{u} = \underline{p} \quad \& \quad \mathbf{K}_{cable} = \mathbf{K}_0 + \mathbf{K}_\sigma \tag{5.1}$$

$$\left[\begin{bmatrix} \frac{E\cdot A}{\ell} & 0 & -\frac{E\cdot A}{\ell} & 0 \\ 0 & 0 & 0 & 0 \\ -\frac{E\cdot A}{\ell} & 0 & \frac{E\cdot A}{\ell} & 0 \\ 0 & 0 & 0 & 0 \end{bmatrix} + \begin{bmatrix} 0 & 0 & 0 & 0 \\ 0 & \frac{N}{\ell} & 0 & -\frac{N}{\ell} \\ 0 & 0 & 0 & 0 \\ 0 & -\frac{N}{\ell} & 0 & \frac{N}{\ell} \end{bmatrix}\right] \cdot \begin{bmatrix} u_1 \\ v_1 \\ u_2 \\ v_2 \end{bmatrix} = \begin{bmatrix} 0 \\ -P/2 \\ 0 \\ -P/2 \end{bmatrix} \tag{5.2}$$

With E - the Young modulus of the cable, A - the area of the cable, ℓ - the length of the cable and N - the normal force in the cable.
The terms highlighted in the K_σ matrix are the *coupling terms*. They represent the *restoring force* of cables, a lateral force developed by a cable, acting similarly to a spring. This allows a cable subjected to lateral load to return to its initial position once that load is removed, as represented in Figure 5.5. If not present, in the FE modelling, the cable is not restrained by anything and is free to move unboundedly.

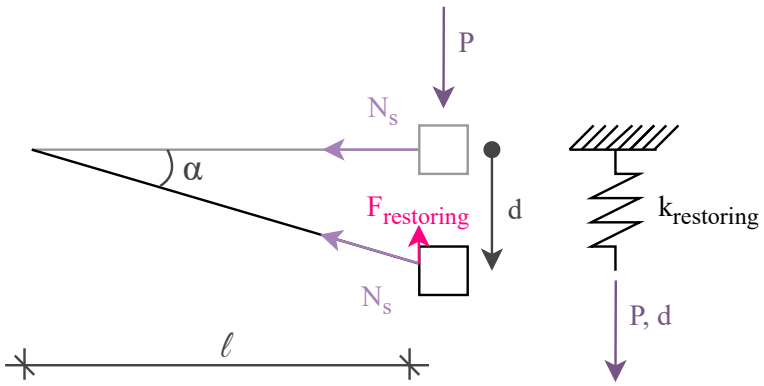

Figure 5.5: Schematic representation of the restoring force.

The restoring effect can be characterized as follows:

$$d = \ell \cdot \tan\alpha \approx \ell \cdot \alpha \Leftrightarrow \alpha = \frac{d}{\ell} \tag{5.3}$$

$$F_{restoring} = N_s \cdot \sin\alpha \approx N_s \cdot \alpha \tag{5.4}$$

$$F_{restoring} = N_s \cdot \frac{d}{\ell} = k_{restoring} \cdot d \tag{5.5}$$

$$\Rightarrow k_{restoring} = \frac{N_s}{\ell} \tag{5.6}$$

However, linear analyses in the software only take into account the K_0 matrix and thus, neglect the restoring effect. This means that once a cable is exposed to lateral force, it will not be counteracted by any stiffness and will undergo unbounded displacements. The system becomes a mechanism as the determinant of the linear stiffness matrix, $\mathbf{K}_0$, becomes equal to 0.

$$|\mathbf{K}_0| = 0 \Rightarrow \omega_{eig} = 0 \tag{5.7}$$

This overwhelms any other effect in the bridge. For example, when analysing the natural frequencies of the bridge, cable modes with frequencies close to zero take over any other actual mode of the bridge, with the cables acting in an unnatural way. That behaviour is represented in Figure 5.6 below.

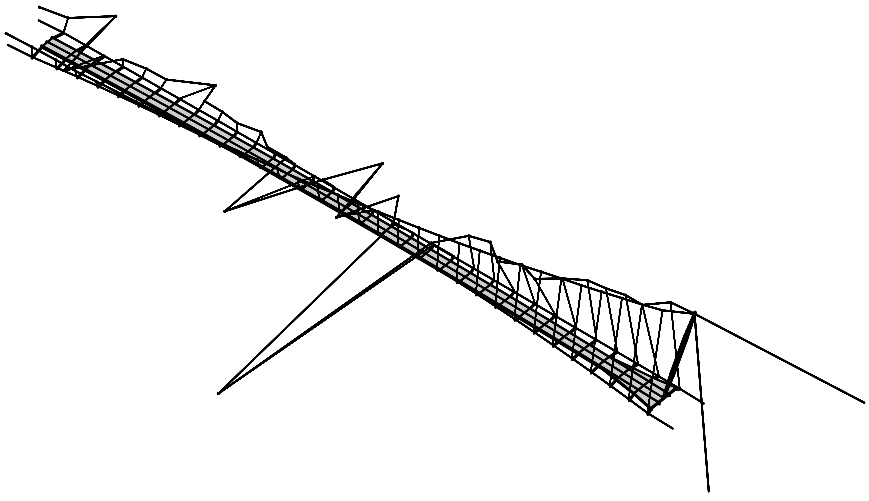

Figure 5.6: Behaviour of the cables when no lateral stiffness is modelled.

Not all cables are affected: stiffness has to be provided in all three directions by another element or the cable has to be defined as a single element. The secondary cables (in blue in Figure 5.3) are linked to the cross-beams which bring enough rigidity for the cables as well. The hangers are each defined as a single element, as well as the back cables anchored in the ground. The only elements concerned by a possible lack of lateral stiffness are the main suspension cables (in purple in Figure 5.3). To overcome that issue, stiffness has to be provided in another way. As most of the lateral stiffness of the deck comes from the suspension, it is fundamental to represent the restoring forces associated with the large axial forces in the hangers. To this end, several options were considered :

1. Figure 5.7 (a):1-D spring, connected to a rigid beam with no mass fixed to the deck. This allows to transfer the rigidity of the cross-beams for the cable, and to take the relative displacements of the deck into account
2. Figure 5.7 (b):3-D spring overlapped with the hangers
3. Figure 5.7 (c):Residual stress in the main cable - **Only possible for non-linear analysis**. Residual stresses are used to provide an initial axial force N, giving the cable an initial restoring force in the $\mathbf{K}_\sigma$ matrix. Hence, it cannot be used for linear analysis.

NB: It is not possible to use a spring anchored in "the external world", as the displacement of the deck influences the behaviour of the cables.

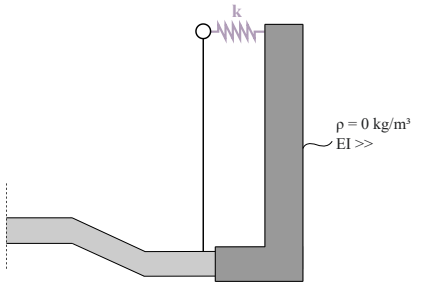

(a) Solution 1:1-D spring, connected to a rigid beam with no mass fixed to the deck.

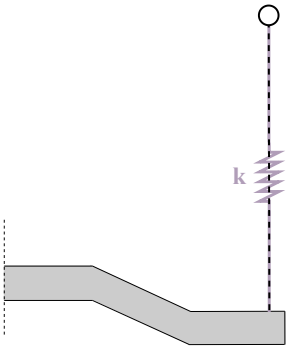

(b) Solution 2:3-D spring overlapped with the hangers.

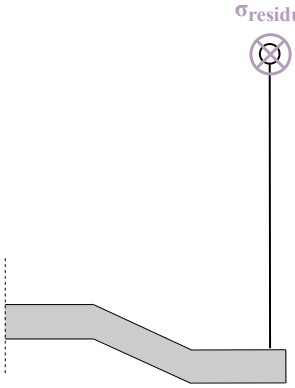

(c) Solution 3:Residual stress in the main cable - **For non-linear analysis only**.

Figure 5.7: Sketches of the various solutions considered to overcome the cable issue.

Residual force (N_{res}) and stiffness of the springs (k) of the suspension cables

For a cable divided into 32 elements of 3.95 m:

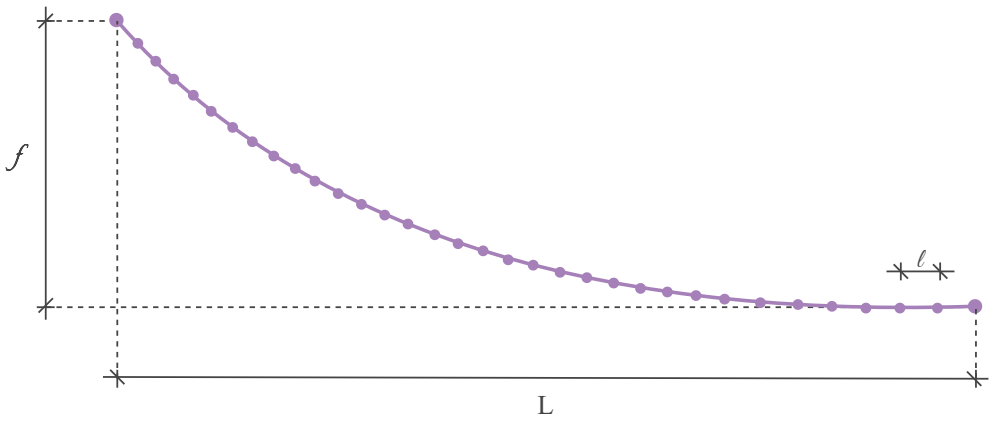

Figure 5.8: Sketch of the division of the suspension cable in 32 elements.

$$\text{From } \texttt{Finelg} : M_{tot} = 118{,}150 \text{ kg} \tag{5.8}$$

$$p = \frac{M_{tot} \cdot g}{L} = \frac{118{,}118 \cdot 9.81}{123.255} = 9400 \text{ kN/m} \tag{5.9}$$

$$f = 16.355 \text{ m} \tag{5.10}$$

$$N_{res} = \frac{p \cdot L}{8 \cdot f} = \frac{9400 \cdot 123.255^2}{8 \cdot 16.355} = 1091.3 \text{ kN} \tag{5.11}$$

$$k = \frac{N}{\ell} = \frac{1124.66}{3.95} = 276.3 \text{ kN/m} \tag{5.12}$$

The first two solutions were tested in linear analysis and brought the same results. The decision was to keep solution 2 (i.e. 3-D spring overlapped with hanger, see Figure 5.7 (b)), as it involves fewer elements and results in a cleaner model. Equation 5.11 indirectly provides the initial residual stress to be applied to the suspension cables for the non-linear analyses, calculated as $\sigma_r es = F_{res}/A_{cable}$. Equation 5.12 defines the initial stiffness of the 3-D springs in the linear analyses.

Sag effect

When under-stressed, the cables are at risk of being subjected to sag effect: a transversal deformation of the cable under its own weight due to a lack of tension, as represented in Figure 5.9 (a). Sometimes, that effect can be sought, as for the two suspension cables that yield large deformations. For cables that should be fully taut, for example in cable-stayed bridges, or for the two back cables linked to the pylon and anchored in the ground (in purple in Figure 5.3), that effect has to be avoided. It might induce unwanted deformations and accentuate the non-linearities already present due to the suspension cables. However, if the cables are under-taut and subjected to those deformations, it has to be taken into account in the model by defining the cable with an initial deformation.

It is possible to verify if the cable is prone to such effect by computing the tangent Young modulus (E_t) of the cable and comparing it to its elastic Young modulus (E_e). If they are close to one another, the cable isn't at risk of deflecting under its own weight because the internal tension is bigger than any effect due to its self-weight. This is represented in Figure 5.9 (b).

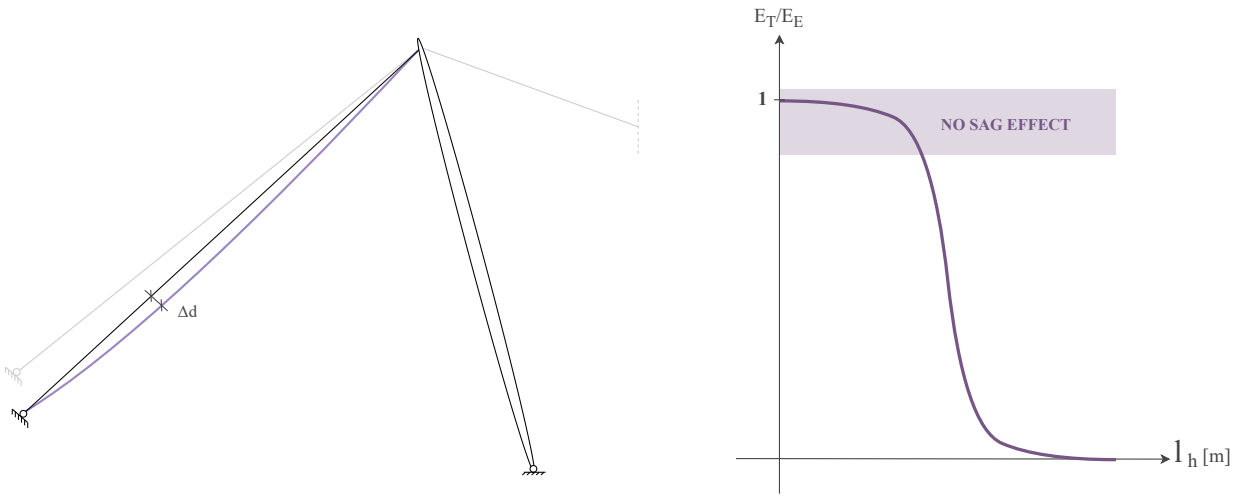

(a) Schematical representation of the sag effect: if under-taut, a cable will tend to deflect under its self-weight, developing non-linearities when deformed.

(b) Graph representing the risk of developing sag effect in a cable, depending on its length and the ratio between the tangent and elastic Young moduli E_t/E_e.

Figure 5.9: Schematic representation of the sag effect in a cable.

The ratio between the tangent and elastic Young moduli can be computed as follows:

$$\frac{E_t}{E_e} = \frac{1}{1 + \frac{(\gamma \cdot \ell_h)^2}{12 \cdot \sigma^3} \cdot E_e} \tag{5.13}$$

with γ - the volumetric weight of the cable,ℓ_h - the projected horizontal length of the cable, σ - the current stress state of the cable ($\frac{F}{A}$), E_e - the elastic Young modulus of the cable. The back cables have different lengths, thus are differently stressed. The forces in the cables result from the static non-linear analysis.

	Back cable no. 1	Back cable no. 2
ρ [kg/m³]	8320	8320
ℓ_h [m]	15.48	18.68
F [kN]	1793.5	1813.3
A [mm²]	6890	6890
σ [MPa]	260	263
E_e [MPa]	160,000	160,000
E_t/E_e	**0.9983**	**0.9988**

Table 5.1: Characteristics of the back cables.

As shown in Table 5.1, the two cables have a ratio of tangent and elastic Young moduli close to 1. In that case, the sag effect that could develop is neglected. As a demonstration, the graph representing the ratio between E_t and E_e depending on the cable length and stress level is plotted in Figure 5.10. The two vertical lines represent cable no. 1 and no. 2. As can be seen, for a stress level of 260 MPa, there is barely any risk of developing a chain effect, as the ratio does not exceed 0.9, even for cable lengths going up to 100 m. The two back cables can be represented as a single element.

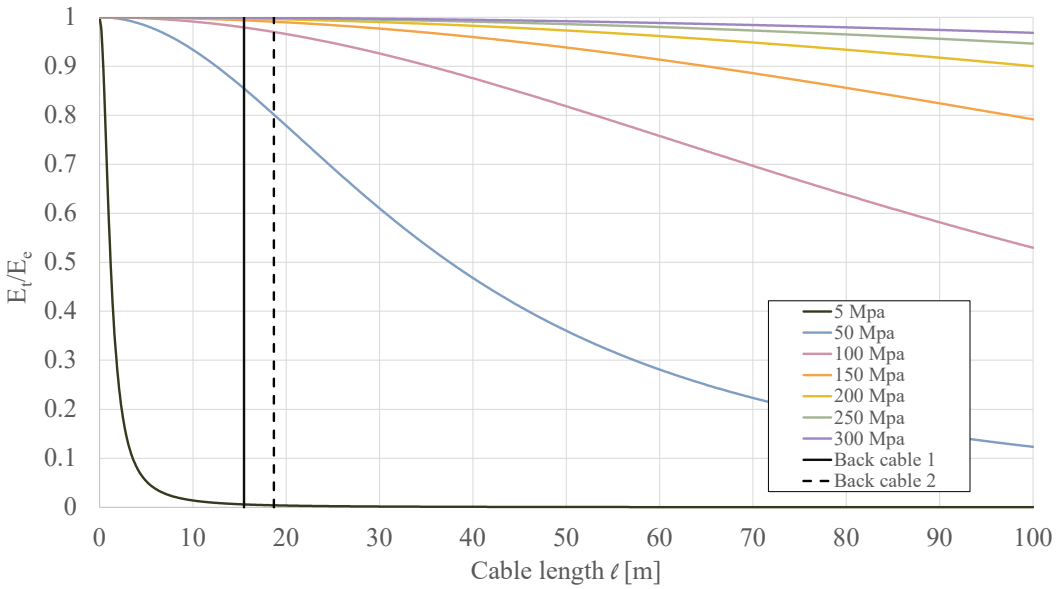

Figure 5.10: Ratio of the tangent and elastic Young Moduli depending on the length of the cable, with the characteristics (A, ρ, E_e) of the back cables, for different levels of internal stress.

5.3 Analyses

Three types of analyses are performed on the numerical model. They are summed up and shortly explained below, and the simulation process is explained in Figure 5.11.

- **Static** - Both linear and non-linear - Quantify the initial deformation of the footbridge under its self-weight
- **Dynamic modal** - Linear equivalent and non-linear - Determination of the eigenfrequencies and corresponding mode shapes. In addition, comparison of the effect of non-linear stiffness and equivalent linear stiffness
- **Step-by-Step dynamic** - Linear and non-linear - Determination of the behaviour of the footbridge under an imposed load. As linear simulations are much faster, they are used to tune the TMDs. Non-linear simulations are used to reconstruct the FRFs of the bridge under a sine sweep. In addition, sensitivity analyses are performed to determine the ideal time step and sweep rates to use for the non-linear analyses.

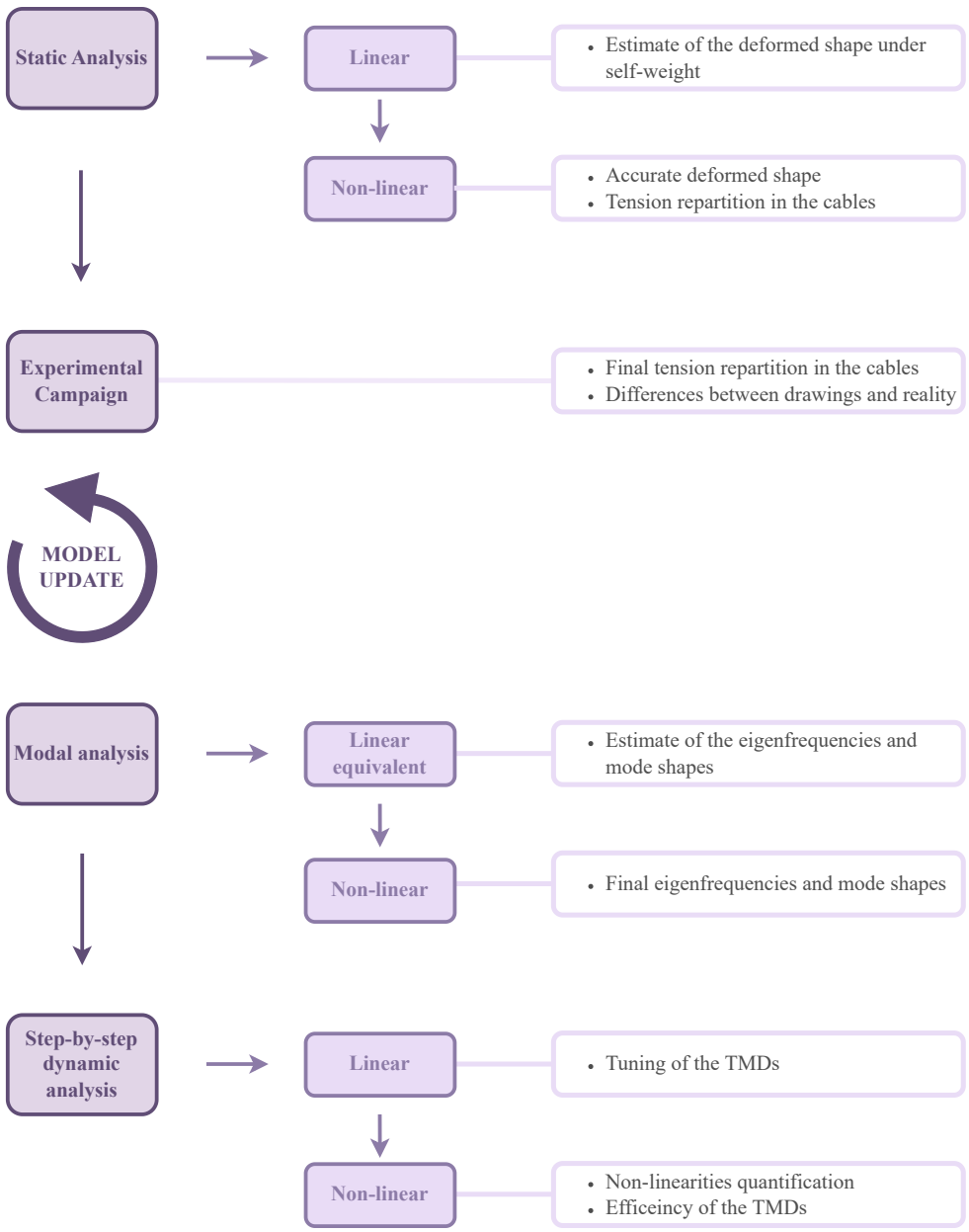

Figure 5.11: Summary of the simulation process and of the main checks per simulation.

Static analyses

As previously stated, the static analyses allow to quantify the deformed shape under the self-weight. The linear analysis is mainly used to cross-check the non-linear one, in order to verify that the model is working correctly and that the parameters of the analysis are well defined. In bridges with cables, the hangers are tuned to generate internal stresses under the deformations due to self-weight that suppress most of the initial deformation so that the bridge only deflects when an external load is applied.

The non-linear analysis performed with 10 **Newton-Raphson + skip steps and a equilibrium forces ratio of** $FHE_i/FHE_0 = 10^{-6}$. The deflections under self-weight without any tuning in the suspension cables and hangers are non-negligible. The Serviceability Limit State (SLS) for deflections for a pedestrian

footbridge are set at L/300 for soft mobility use only:

$$\delta_{SLS} = \frac{L}{300} = \frac{123.55}{300} = 41 \text{ cm} \tag{5.14}$$

	Linear	Non-Linear
δ [cm]	86.3	69.94
$\delta < \delta_{SLS}$	No	No

Table 5.2: Results of the first set of static analyses.

The deformed shapes for linear and non-linear analyses are equivalent, with the exception that the deflections are larger in the linear analysis. This can be explained by the difference in stiffness of the cables considered for the analyses. During the linear analysis, the stiffness considered is the initial stiffness of the cable. Nonetheless, as the structure is mobilized, the stiffness of the cables increases. This gives a better resistance to deflection in the non-linear analysis rather than in the linear one. Though, the similarity in the shape of the deformation illustrates the accuracy of the static non-linear model. The large

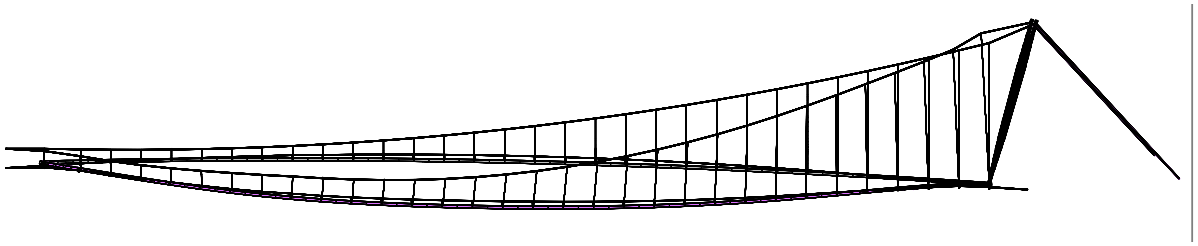

Figure 5.12: Result of the first non-linear static analysis - Deflection of the bridge under self-weight - amplified 10 times.

displacements under self-weight must be compensated by tuning each hanger with the same residual forces, as illustrated in Figure 5.13. The force in the suspension cable is raised as well, with an additional 1100 kN added to the initial residual forces. These tweaks with the cables reduce the deflections of the non-linear model to **19.7 cm**, half of the SLS criterion on deflection.

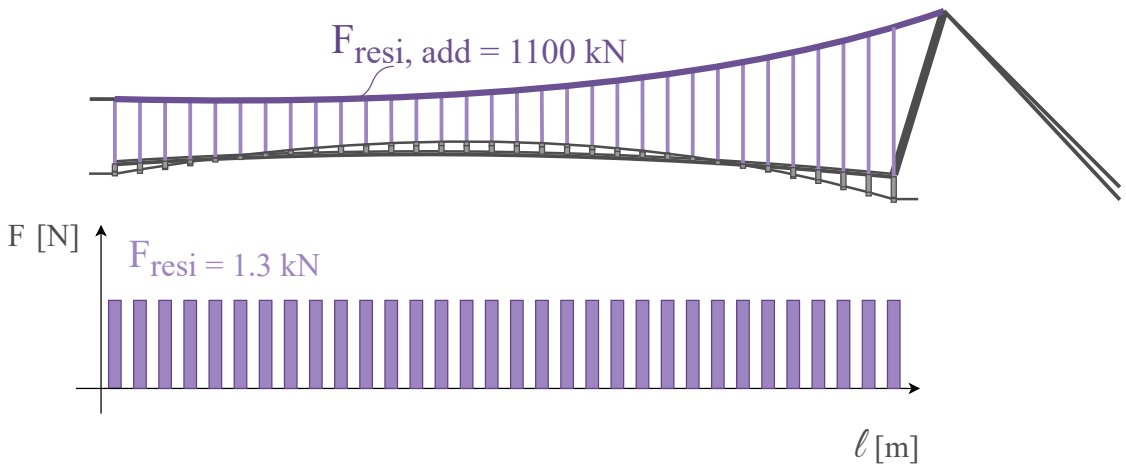

Figure 5.13: Schematics of the residual stresses induced in the hangers to suppress the initial deflections due to self-weight.

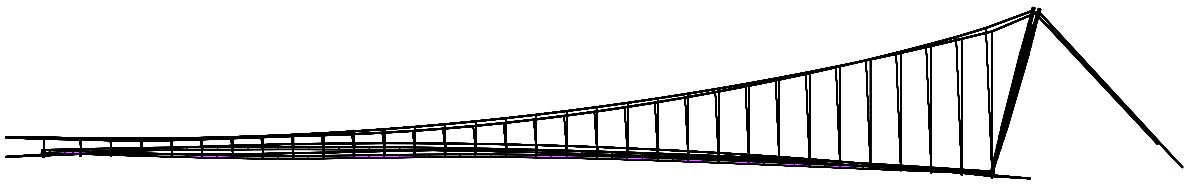

Figure 5.14: Result of the second non-linear static analysis with cables tuned - Deflection of the bridge under self-weight - amplified 10 times.

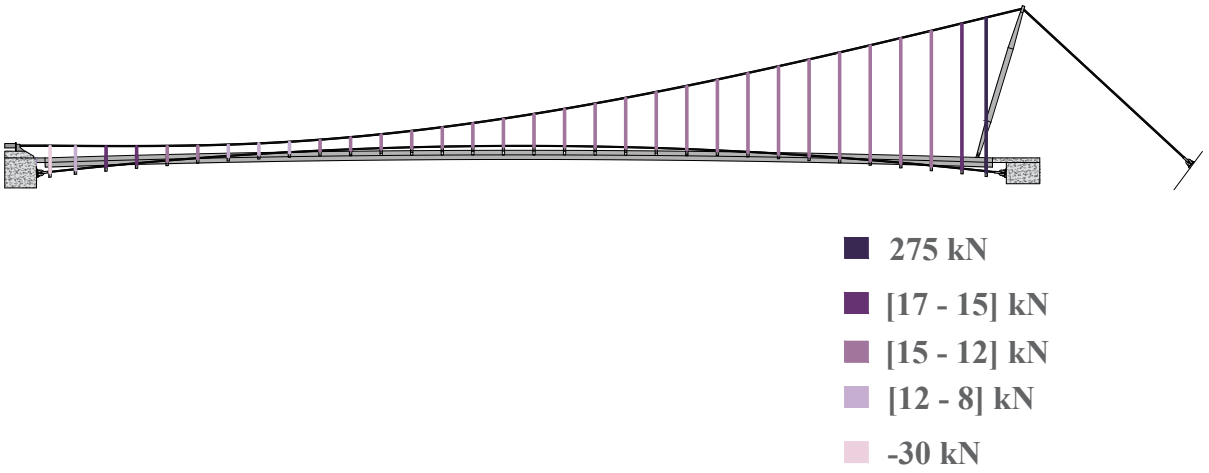

Figure 5.15: Tension distribution in the hangers with all hangers tuned identically.

Figure 5.15 is a summary of the tension distribution in the hangers. The average tension is about 13 kN per hanger, although the longest one bears a tension close to 275 kN while the last hanger is in compression. These values, especially the extreme ones, are different from the hypothesis formulated based on the experimental analysis of the hangers, in section 4. Another residual stress pattern is applied to the hangers in order to match the results of the experimental campaign. These adjustments induce a negative deflection under self-weight of 18.2 cm, still in the acceptable range for the SLS criterion, as shown in Figure 5.17. Moreover, the pattern causes an upward deflection of the bridge on the pylon side. This deflection enhances the initial curve of the bridge, which was less apparent in the first analyses. The adjustments allow to keep that initial curvature and thus, respond to the architectural intentions of the engineering office. Figure 5.18 illustrates that this new distribution results in an average tension of about 16 kN, closer to the expected values. The longest hanger now bears about 77 kN and the last cable is in tension.

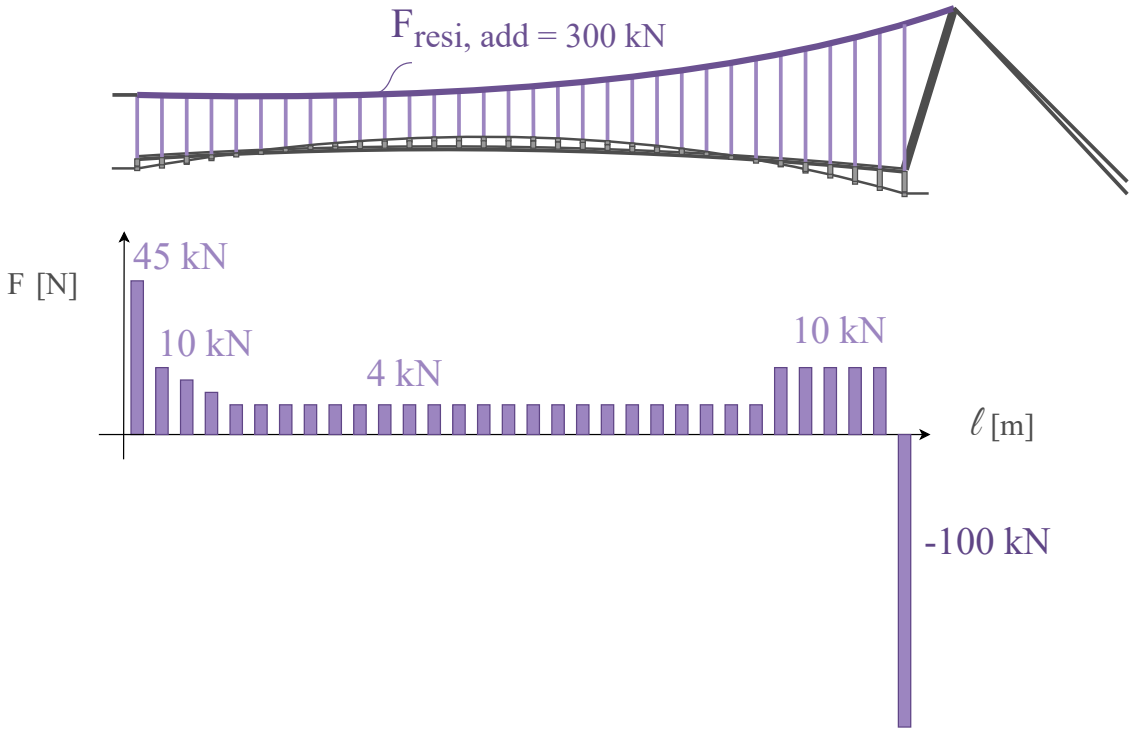

Figure 5.16: Updated distribution of the residual stresses to match the hypothesis of the tension repartition based on the results from the experimental campaign.

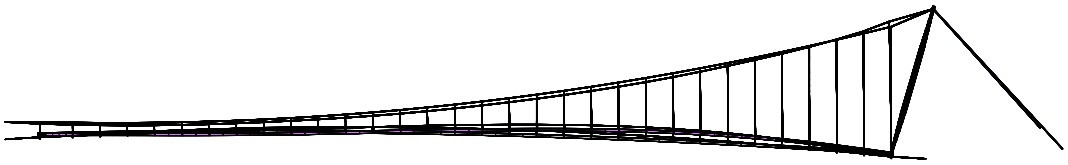

Figure 5.17: Updated deflection of the bridge, based on the residual stress distribution matching the hypothesis from the experimental campaign - amplified 2.5 times.

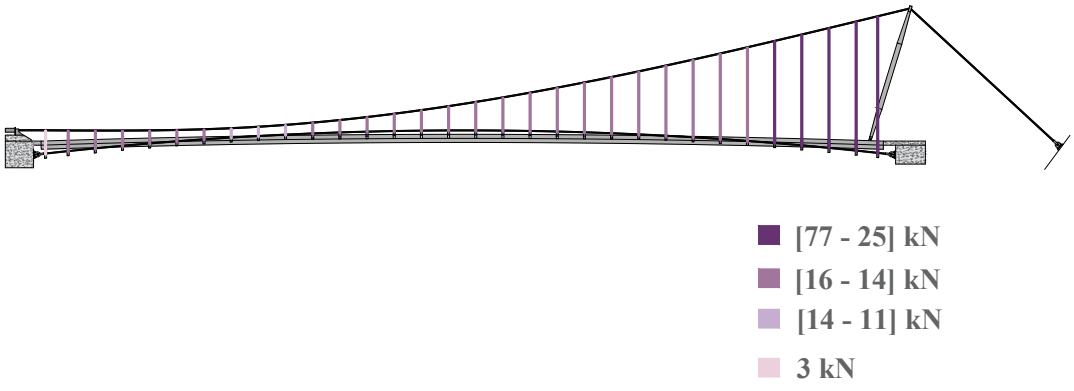

Figure 5.18: Updated tension distribution in the hangers, based on the residual stress distribution matching the hypothesis from the experimental campaign.

Dynamic modal analyses

The deformed shape of the bridge under its self-weight and the experimental campaign allowed to define a pattern of residual stresses to apply to the hangers and the suspension cables. Now that those values are established, it is possible to move on to the dynamic analyses to determine the eigenfrequencies and mode shapes of the structure.

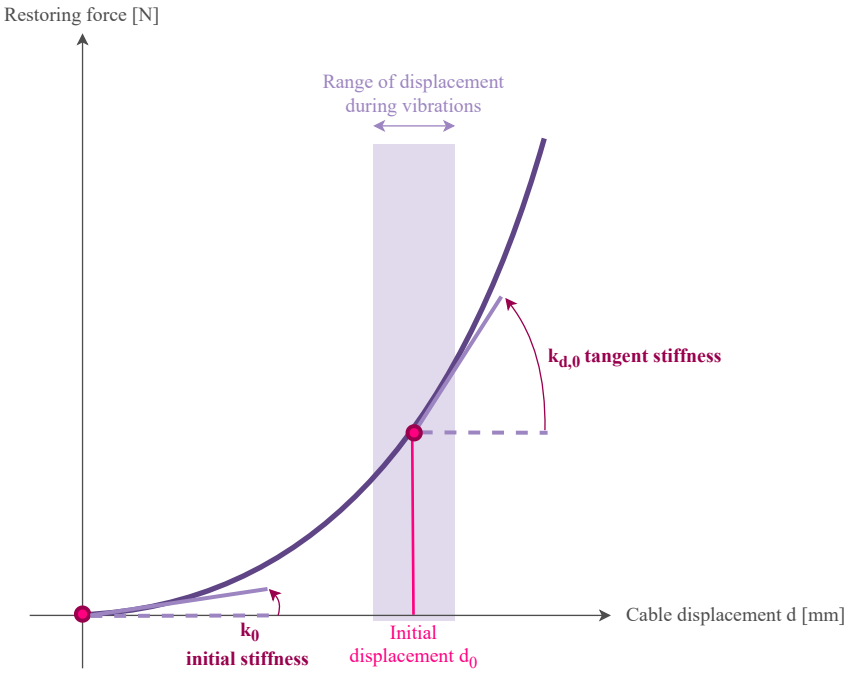

Figure 5.19: Representation of the cubic evolution of the restoring force based on displacement of the structure.

Two sets of analyses are performed: a linear one, called linear equivalent, and a non-linear one. The linear equivalent dynamic analysis consists of supplying the non-linear deformed shape to the numerical model to provide stiffness to the cables. As the cables have a non-linear behaviour, represented by a quadratic stiffness, the initial deformation mobilizes the cable and gives them a higher stiffness, corresponding to the tangent to the value of the cubic restoring force function. This value is higher than the initial stiffness and closer to the actual non-linear value of the stiffness of the cable, as represented in Figure 5.19. The non-linear analysis works with the same concept. It is divided into two parts:a first non-linear static analysis with 10 Newton-Raphson + skip steps and an equilibrium forces ratio of $FHE_i/FHE_0 = 10^{-6}$ followed by a linear computation of the eigenfrequencies and eigenmodes. These analyses can be compared in order to quantify the differences between the 3-D springs or residual stresses to model the restoring force.

Results of the non-linear modal analysis:

The results of the main analysis are represented in Figures 5.20 to 5.23. All deformed shapes are standardized, with the maximal displacement considered equal to 1 and then amplified 25 times. Hence, the deformed shapes alone cannot quantify the modal participation per mode. Table 5.3 summarizes the characteristics of each mode, including eigenfrequencies and modal participation. Those results will be compared to the linear equivalent and to experimental results, in order to evaluate the accuracy of the numerical model.

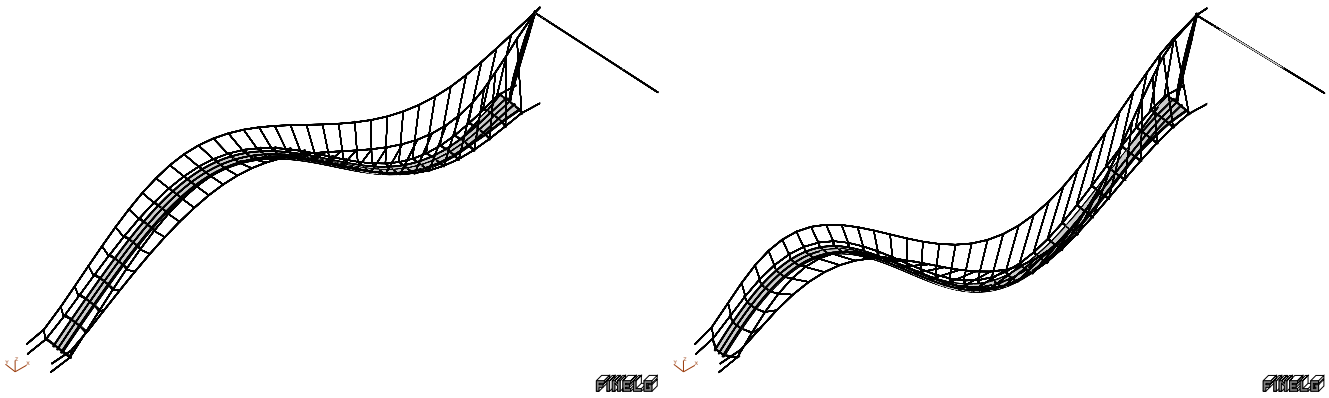

(a) Representation of the first vertical eigenmode - f = 0.575 Hz - Amplification x25.

(b) Representation of the second vertical eigenmode - f = 0.67 Hz - Amplification x25.

Figure 5.20: Representations of the two first vertical eigenmodes - Amplified x25 - From `Finelg`.

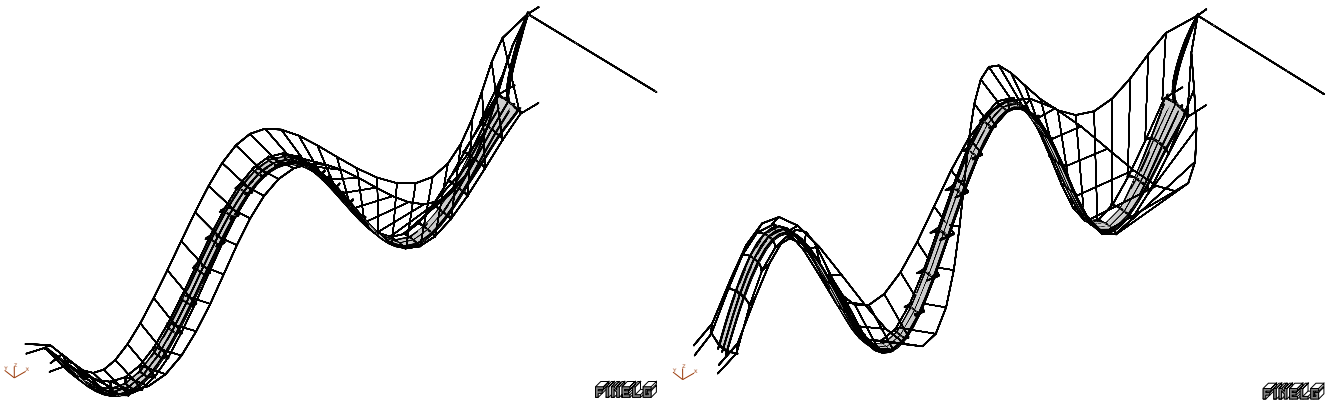

(a) Representation of the third vertical eigenmode - f = 1.07 Hz - Amplification x25.

(b) Representation of the fourth vertical eigenmode - f = 1.52 Hz - Amplification x25.

Figure 5.21: Representations of the third and fourth vertical eigenmodes - Amplified x25 - From `Finelg`.

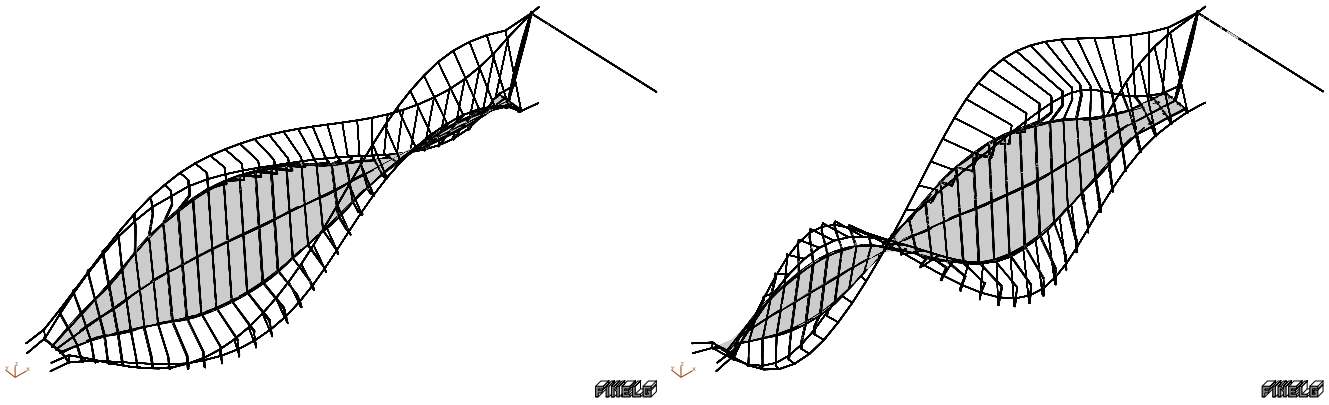

(a) Representation of the first torsional eigenmode - f = 1.1 Hz - Amplification x25.

(b) Representation of the second torsional eigenmode - f = 1.39 Hz - Amplification x25.

Figure 5.22: Representations of the two first torsional eigenmodes - Amplified x25 - From `Finelg`.

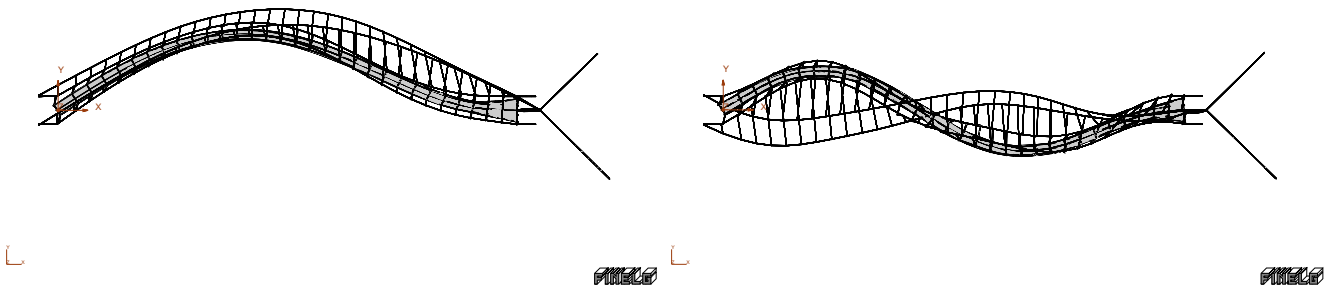

(a) Representation of the first horizontal eigenmode - f = 0.75 Hz - Amplification x25.

(b) Representation of the second horizontal eigenmode - f = 2.15 Hz - Amplification x25.

Figure 5.23: Representations of the two first horizontal eigenmodes - Amplified x25 - From Finelg.

Type of mode	Eigenfreq. [Hz]	Global Shape	Generalized mass [kg]	Modal participat°
Vertical	0.57	1/2 sine wave	32,870	V: 37.14 %
Vertical	0.67	2 x 1/2 sine wave	33,714	V: 17.64 %
Vertical	1.07	3 x 1/2 sine wave	37,903	V: 20.19 %
Vertical	1.52	4 x 1/2 sine wave	47,125	V: 0.11 %
Torsional	1.10	1/2 sine wave + Torsion	12,801	V: 0.94 %
Torsional	1.39	2 x 1/2 sine wave + Torsion	13,670	V: 0.03 %
Horizontal	0.75	1/2 sine wave + Torsion	31,380	H: 61 %
Horizontal	2.15	2 x 1/2 sine wave + Torsion	7590	H: 0.8 %

Table 5.3: Main characteristics of the first eigenfrequencies from a non-linear analysis in Finelg.

Based on the modal frequencies, mode shapes, generalized masses, and modal participation factors calculated, it can be concluded that the model exhibits a dynamic behaviour expected for a standard bridge structure. The first, second, and third vertical modes, along with the first horizontal mode, show the highest modal participation factors and are therefore the dominant contributors to the dynamic response of the structure. The first vertical mode represents the fundamental vertical vibration mode, and the first horizontal mode corresponds to the fundamental horizontal vibration mode, as indicated by the large modal participation. Although the fourth vertical mode has a relatively high generalized mass, its modal participation is very low due to its complex mode shape featuring multiple half sine waves with opposing vertical displacements. This results in a low net vertical displacement despite large internal movements within the structure. Such higher-order modes are inherently more difficult to excite externally because of these opposing motions.

The torsional modes demonstrate both low generalized mass and low modal participation. These modes rotate around the longitudinal axis of the bridge and do not contribute significantly to the vertical or lateral dynamic response. The net vertical displacement in these modes is close to negligible. Overall, the modal characteristics point towards a typical behaviour for a bridge, where the fundamental modes govern the response, and higher modes have a limited influence on the global dynamic behaviour.

Table 5.4 summarizes the results of the numerical and experimental analyses. An analysis was conducted to evaluate the model accuracy against the experimental results and to compare the differences between the linear and non-linear models. The results are summed up in Figure and 5.25. When focusing on Figure 5.24, the relative differences between the two analyses are limited. The highest relative difference reaches around 20 %, even though, for most modes, it does not exceed 10 %. In addition, it seems that the analyses have closer results for higher frequencies. The same behaviour can be observed in Figure 5.25.

	Linear equivalent	Non-linear	Experimental
Restoring effect	3-d springs	Residual stresses	/
Vertical modes			
Mode 1 V [Hz]	0.62	0.57	0.65
Mode 2 V [Hz]	0.80	0.67	0.74
Mode 3 V [Hz]	1.11	1.07	1.13
Mode 4 V [Hz]	1.49	1.52	1.52
Mode 5 V [Hz]	1.98	1.93	1.97
Mode 6 V [Hz]	2.54	2.49	2.56
Torsional modes			
Mode 1 T [Hz]	1.14	1.1	1.1
Mode 2 T [Hz]	1.49	1.39	1.23
Mode 3 T [Hz]	1.92	1.90	Non Determined
Horizontal mode			
Mode 1 H [Hz]	0.78	0.75	0.5
Mode 2 H [Hz]	2.2	2.15	0.98

Table 5.4: Eigenfrequencies and mode shapes from the dynamic analyses and the experimental campaign.

This can be explained by the fact that the first modes are more global modes whereas the higher modes are considered more local. The simplifications in the numerical model have a lesser impact on those modes as less mass and displacement are concerned. The first modes are the most sensitive and need a really detailed and accurate model to be accurate. This is represented in Figure 5.26.

The first mode has the most modal participation, often around 50 %, due to its half sine wave shape. Then the modal participation of the other modes decreases as the mode number gets higher, representing more local modes. For the modes 4, 5, and 6, the participation is inferior to 5 % for all three analyses. This explains why those modes are often neglected in design against vibrations, as it is unlikely for those modes to induce high vibrations. Figure 5.25 shows that the model seems globally sound. The relative differences in the vertical and torsional modes are low: the maximum difference reaches 13 % while the average is around 6 %. The accuracy error is often considered acceptable up to 15 % for dynamic studies in most engineering offices.

NB: The relative difference of the second horizontal mode is not represented in the graph for readability reasons, as it is around 120 %..

The horizontal behaviour is completely off the marks. This is probably due to the support conditions. Indeed, in the model, all the supports are considered blocked in the horizontal direction. The deck of the bridge is too restrained and therefore too stiff,leading to higher natural frequencies. When considering one of the supports of the deck free in the horizontal direction, the frequencies are modified, as illustrated in Table 5.5 below. Even though the relative difference is high, 30 % for the second mode, the frequencies are much closer to the experimental values. The issue with this solution is that it changes the deformed shape into unrealistic configurations, as the support is not restrained in the horizontal displacement. The modified mode shapes are represented in Figure 5.27. The solution is probably in the middle: the support condition in the horizontal direction is a dilatation joint in the horizontal direction, for the deck to be able to move and thus, have lower horizontal stiffness, but not to be completely unrestrained in that direction. As having no horizontal restriction seemed unrealistic, the supports are all considered blocked in that direction. Indeed, the rest of the analyses performed on the numerical model concerns the vertical modes, and thus, are less affected by the horizontal supports.

	Initial frequency	Modified frequency	Experimental result	Relative difference
Mode 1 [Hz]	0.78	0.48	0.54	10 %
Mode 2 [Hz]	2.2	1.23	0.94	30 %

Table 5.5: Horizontal frequency modifications due to a change in the horizontal support conditions.

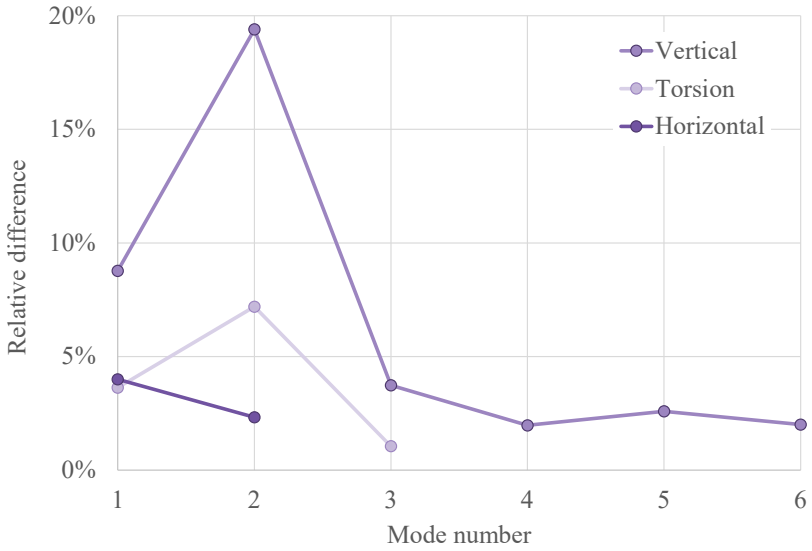

Figure 5.24: Relative differences between the eigenfrequencies obtained with a **linear equivalent** analysis and a **non-linear** analysis.

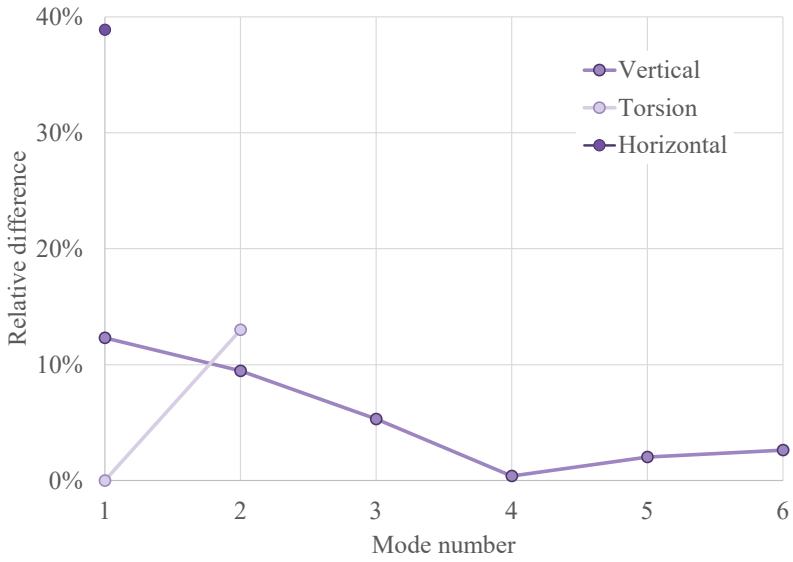

Figure 5.25: Relative differences between the eigenfrequencies obtained with a **non-linear** analysis and the **experimental** results.

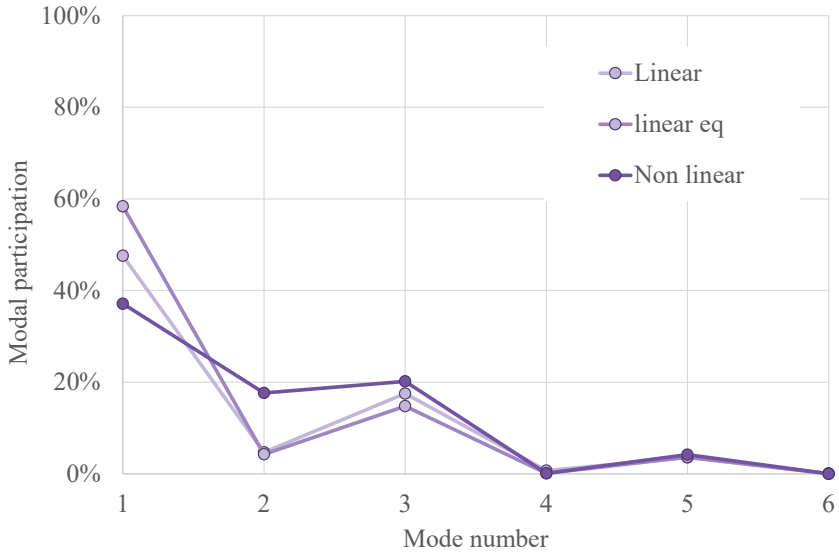

Figure 5.26: Modal participation factor based on the mode number.

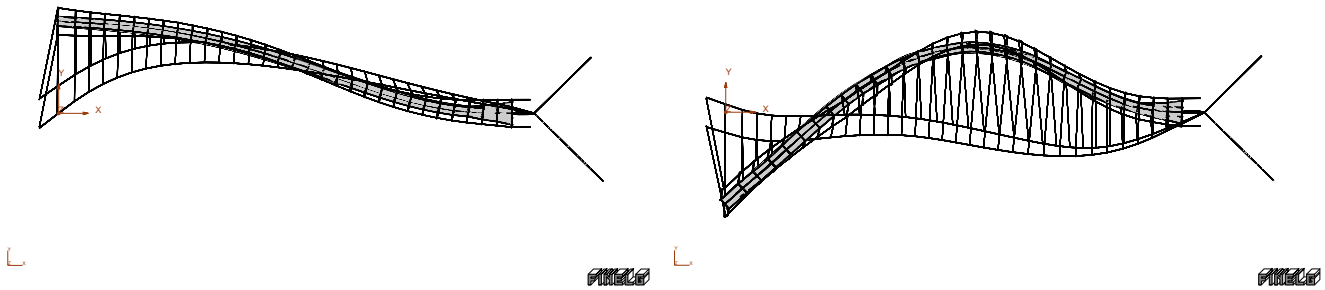

(a) Representation of the first horizontal eigenmode with modified support conditions - f = 0.75 Hz.

(b) Representation of the second horizontal eigenmode with modified support conditions - f = 2.15 Hz.

Figure 5.27: Representations of the two first horizontal eigenmodes with modified support conditions - Amplified x25 - From `Finelg`.

To demonstrate the usefulness of the linear equivalent method, consisting in using the deformed shape of the last non-linear step to compute the eigenfrequencies and eigenmodes, the modal analysis is performed with a linear model with no initial stiffness. Figure 5.28 illustrates the relative differences between the frequencies resulting from the linear equivalent analysis and from the simple linear analysis, both compared to the non-linear results, for the vertical modes and for the torsional modes. The relative differences between the linear and non-linear results are bigger than for the linear equivalent analysis. As the cable stiffnesses for the linear equivalent analysis and the non-linear method are closer to one another than to the initial stiffness, the values are also closer. The initial stiffness being smaller than the tangent, the eigenfrequencies of the bridge are smaller for the simple linear model. It is possible, based on the results of the analysis, to estimate the overall stiffness of the bridge per mode by using the simplified formula of resonant frequency computation, for a SDOF system. For example, for the first vertical eigenmode:

$$\omega = \sqrt{\frac{k_{gen}}{m_{gen}}} \Rightarrow k_{gen} = \omega^2 \cdot m_{gen} \tag{5.15}$$

	Linear	Linear equivalent	Non-linear
Eigenfrequency [Hz]	0.51	0.62	0.57
Eigenfrequency [rad/s]	3.2	3.89	3.58
Generalized mass (from `Finelg`) [kg]	34 605	38,316	32,870
Generalized stiffness [N/m]	355,335	581,464	420,165

Table 5.6: Estimate of the generalized stiffness for the first vertical mode.

As Table 5.6 shows, the stiffness of the linear model is smaller than the other two, resulting in a lower resonant frequency.

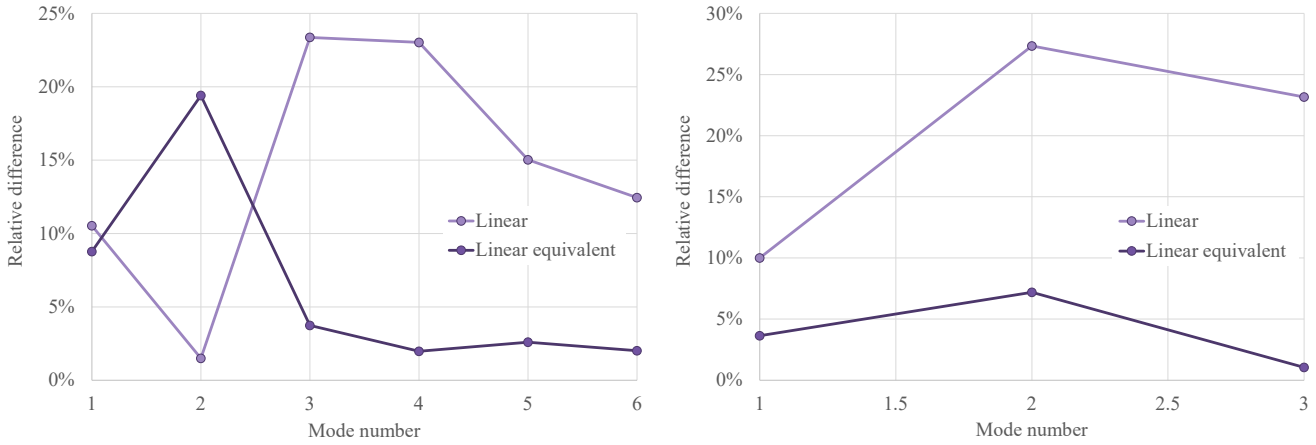

(a) Relative differences for the vertical modes between the eigenfrequencies obtained with a linear equivalent analysis or a linear analysis, and a non-linear analysis.

(b) Relative differences for the torsional modes between the eigenfrequencies obtained with a linear equivalent analysis or a linear analysis, and a non-linear analysis.

Figure 5.28: Relative differences between the linear vs. non-linear and linear equivalent vs. non-linear analyses.

Step-By-Step analyses

Damping model

There are several ways to implement damping in `Finelg`, but the most commonly used in civil engineering is the Rayleigh damping model, previously described in section 2. This method requires the definition of two parameters, α and β, that define the respective participation of the mass and stiffness matrices in the construction of the damping matrix. As a reminder, α and β are computed as follows:

$$\mathbf{C} = \alpha \cdot \mathbf{M} + \beta \cdot \mathbf{K} \tag{5.16}$$

$$\begin{cases} \xi_i = \frac{\alpha}{2 \cdot \omega_i} + \frac{\beta \cdot \omega_i}{2} \\ \xi_j = \frac{\alpha}{2 \cdot \omega_j} + \frac{\beta \cdot \omega_j}{2} \end{cases} \tag{5.17}$$

Two sets of damping ratios and eigenfrequencies are needed to properly determine α and β. However, this thesis is mostly based on the study of the response of the fundamental mode. To this end, the assumption $\alpha = \beta$ is set. The SETRA guide [7] recommends 0.4 % for the damping ratio of steel structures. The purpose of this thesis is to evaluate the behaviour of the bridge with pedestrians, though pedestrians contribute to the damping ratio [8]. The decision is thus to increase the damping ratio of the bridge to 0.6 % to take that

effect into account. The non-linear model is expected to be stiffer than the linear model, and thus produce smaller displacements. To account for that difference, the aim is to set the damping ratio at 0.58 % for the non-linear model, and 0.062 % for the linear model, giving a mean damping ratio of 0.06 % overall. Therefore, a 0.058 % damping ratio results in $\alpha = \beta = 0.003$, as computed in equation (5.18).

$$0.0058 = \frac{\alpha}{2 \cdot \omega_i} + \frac{\beta \cdot \omega_i}{2} \Rightarrow \alpha = \frac{1}{0.0058} \cdot \left(\frac{1}{2 \cdot 2 \cdot \pi \cdot 0.575} + \frac{2 \cdot \pi \cdot 0.575}{2} \right) = 0.003 \tag{5.18}$$

Linear Analysis

The purpose of this analysis is to verify that the tuned mass dampers (TMDs) are functional, and that the dampers designed by *Ruscheweyh Consult* are efficient. The only TMDs represented are those tuned on the first vertical eigenfrequency, as the other set of dampers was not installed on the bridge. The document regarding the damping of the bridge described 4 TMDs but in this model, they are merged into two, one on each side of the main longitudinal beam. As the damped mode is vertical, the position of the TMDs on the cross section of the bridge does not matter. Nonetheless, if the damped mode were a torsional mode, they would have to be placed at the extremities of the cross section, in order to work as efficiently as possible.

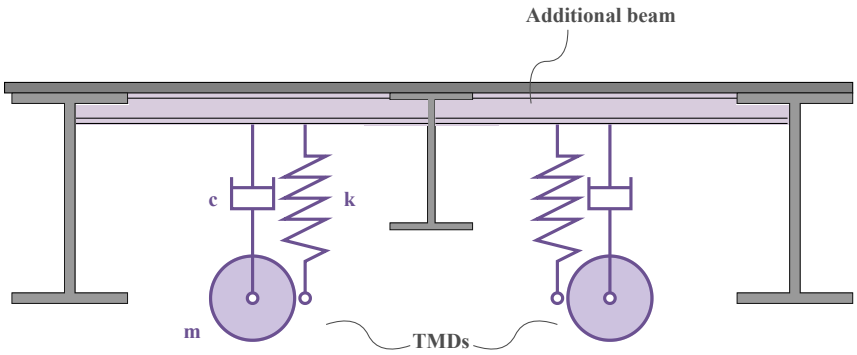

Figure 5.29: Schematisation of the cross-section of the bridge the TMDs and their additional beam.

In the numerical model, the TMDs are modelled as a structure made of a mass, spring and dashpot. The spring is unidirectional and linked to the dashpot to synchronize their movements. The mass is modelled separately as a force representing a concentrated mass, applied where the spring and dashpot are connected to the deck. An additional small beam must be added, in order to ensure the energy transfer of the TMD to the deck, as illustrated in Figure 5.29.

The characteristics of the TMDs are kept as close as possible to the existing ones. To that end, the mass ratio between the generalized mass and the mass of the TMD is preserved. In addition, as the damping of the TMD is not provided in the available documents, the TMD is designed as a Den Hartog TMD. To design a single damper, the number of TMDs has to be taken into account, as the computations take into account the total mass, stiffness and damping. The computations are described below. In addition, Table 5.7 sums up the characteristics of a single TMD.

NB: As the analysis performed is linear, the eigenfrequency are different from the non-linear one. For these simulations, another TMD fitting the linear conditions was designed, but allowed to validate the process for

the design of the TMD for the non-linear computations.

$$\mu = \frac{m_d}{m_{gen}} \tag{5.19}$$

$$\omega_d = \frac{\omega_{struct}}{1+\mu} \tag{5.20}$$

$$\omega_d = \sqrt{\frac{k_d}{m_d}} \Rightarrow k_d = \omega_d^2 \cdot m_d \tag{5.21}$$

$$\xi_{ideal} = \sqrt{\frac{3}{8} \cdot \frac{\mu}{1+\mu}} \tag{5.22}$$

$$c_{crit} = 2 \cdot \sqrt{m_d \cdot k_d} \tag{5.23}$$

$$c_d = \xi_{ideal} \cdot c_{crit} \tag{5.24}$$

Dimensionless parameters related to the efficiency of the TMD can be computed to ensure a strong design before the computations.

$$G_\kappa = \frac{\frac{\dot{\omega}}{\omega^2}}{\frac{m_d}{m_s}} = \frac{\frac{0.0002}{(0.62 \cdot 2 \cdot \pi)^2}}{0.031} = 4.26 \cdot 10^{-4} \tag{5.25}$$

$$G_\xi = \frac{\xi_d}{\sqrt{\mu}} = \frac{0.106}{\sqrt{0.03}} = 0.60 \tag{5.26}$$

$$G_\delta = \frac{\omega_d/\omega_s - 1}{\sqrt{\mu}} = \frac{(0.519 \cdot 2 \cdot \pi)/(0.617 \cdot 2 \cdot \pi) - 1}{\sqrt{0.031}} = -0.17 \tag{5.27}$$

$$\tag{5.28}$$

From [9], those parameters indicate that the damper should have an efficiency of about 85 to 90 %.

	Existing TMDs	Non-linear TMDs	Linear TMD
Number of dampers	4	2	2
ω [rad/s]	$0.707 \cdot 2 \cdot \pi = 4.4$	$0.575 \cdot 2 \cdot \pi = 3.61$	$0.62 \cdot 2 \cdot \pi = 3.2$
ω_d [rad/s]	$0.685 \cdot 2 \cdot \pi = 4.30$	$0.557 \cdot 2 \cdot \pi = 3.50$	$0.62 \cdot 2 \cdot \pi = 3.78$
m_d [kg]	293	513.65	585.9
k_d [N/m]	5550	6525.4	5906.4
m_{gen} [kg]	37,500	32,870	34,605
μ [-]	3.1 %	3.1 %	3.1 %
ξ_{ideal} [-]	10.6 %	10.6 %	10.6 %
c_{crit} [Ns/m]	2550	3661.5	3720
c_d [Ns/m]	271.8	388.3	394.6

Table 5.7: Characteristics of one existing TMD and of one numerical TMD.

To verify tuning of the damper, a 10,000 N sine sweep load is applied to the deck of the bridge at the anti-node of the first mode. The displacement is computed as follows.

$$d_{static} = \frac{F}{k} = \frac{10{,}000}{581{,}464} = 17.2 \text{ mm} \tag{5.29}$$

$$d_{amp} = d_{static} \cdot \frac{1}{2 \cdot \xi} = 29 \cdot 80.38 = 1382.6 \text{ mm} \tag{5.30}$$

$$\tag{5.31}$$

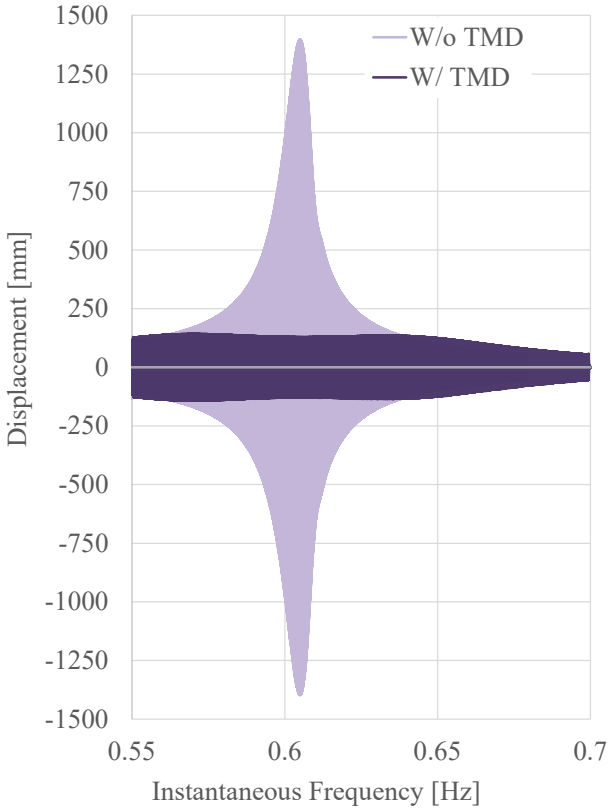

Figure 5.30: Comparison of the response of the structure with and without damping under a 10,000 N TMD.

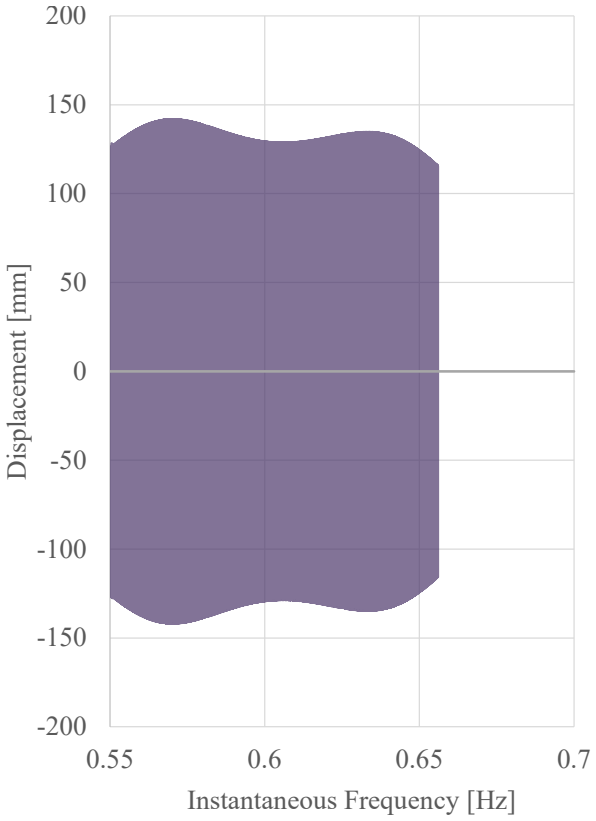

Figure 5.31: Response of the damped structure under a 10,000 N sine sweep.

Figure 5.30 illustrates the response of the structure with and without damper. The damper significantly reduces the peak displacement of the structure, decreasing it from approximately 1380 mm to less than 150 mm. This corresponds to a reduction of about 90 %, in agreement with the theoretical efficiency estimated earlier. The TMD proves to be both effective and well-tuned for this application. Figure 5.31 represents a zoom on the response with the TMD. The response is similar to a typical TMD response, where the original resonance peak is split into two smaller peaks of comparable amplitude. While the TMD effectively reduces displacements, the remaining vibration still results in relatively high accelerations, around 2.25 m/s², as shown in equation (5.32). However, such large loading conditions, on the order of 10,000 N, are extremely rare during the service life of a footbridge, particularly for a class III structure. In such exceptional cases, the objective would be to prevent structural damage rather than to ensure pedestrian comfort. Nonetheless, this analysis demonstrates the TMD high effectiveness, and the observed behaviour remains applicable under more typical loading scenarios as well.

$$a_{TMD} = d_{TMD} \cdot \omega^2 = 0.15 \cdot (2 \cdot \pi \cdot 0.617)^2 \simeq 2.25 \text{ m/s}^2 \tag{5.32}$$

Non-linear analysis

This section describes the sensitivity studies performed in order to assess the impact of selected computation parameters on the accuracy of the computation. First, a sensitivity analysis on the time step is performed, in order to check whether the non-linearities of the bridge have an impact on the accuracy of the model for a step-by-step analysis. Second, as the final purpose of this thesis is to excite the structure

with a sine sweep, an analysis on the sweep rate is performed, to determine a criterion on the limit sweep rate for the development of a steady state.

Time-step sensitivity

A series of sine sweeps are prepared, with the exact same characteristics, except for their time step. The frequency with the bigger modal participation is 0.575 Hz. Hence, the analysis focuses on this mode to ensure a significant displacement, that can be easily compared between the simulations. The sine sweep ranges between 0.53 and 0.60 Hz. As a reminder, the equation of a sine sweep starting at a non-zero frequency is the following :

$$s(t) = A_0 \cdot sin(\omega_0 \cdot t + \frac{1}{2} \cdot \dot{\omega} \cdot t^2) \tag{5.33}$$

with

- A_0, the amplitude of the sine
- ω_0, the initial frequency
- $\dot{\omega}$, the angular speed, i.e. the rate of sweeping

The characteristics of the sine sweep are to be found in Table 5.8 hereunder.

A_0	1000 N
ω_0	0.5 Hz
$\dot{\omega}$	0.001 rad/s^2

Table 5.8: Characteristics of the sine sweep used for the sensitivity analysis.

An array of 7 different time steps is defined in order to build a robust analysis. They are expressed as a ratio of the final period of the sweep for easier identification, as shown in Table 5.9. The time steps range from $T/20$, the reference for linear computations, to $T/50$.

Sweep n°	Time step		Nb iterations	Duration of the simulation	
[-]	[s]		[-]	[s]	[min]
1	$T/20$	0.083	5280	1210	20.1
2	$T/25$	0.066	6600	1380	23
3	$T/30$	0.055	7920	1520	25.4
4	$T/35$	0.047	9240	1735	29
5	$T/40$	0.041	10,558	2000	33.3
6	$T/45$	0.037	11,880	2325	38.7
7	$T/50$	0.033	13,197	2475	41.1

Table 5.9: Characteristics of the simulations for the sensitivity analysis.

As Table 5.9 shows, the size of the time step impacts the time necessary for the computation. However, this should not prevail over result accuracy. This explains the significance of finding a balance between the accuracy of the model and the time of the simulation.

Figure 5.32 illustrates the positive envelope of the results from the computation, expressed as the displacement along the frequency swept. It is readily possible to identify that the bigger time steps have a tendency to shift the position of the peak of the signal, and that that peak tends to have a lower

amplitude. That can be explained by the fact that a too large time step increases the risk of overlooking the extrema of the entry signal, and thus never imposing the load at full amplitude, as shown in Figure 5.33.

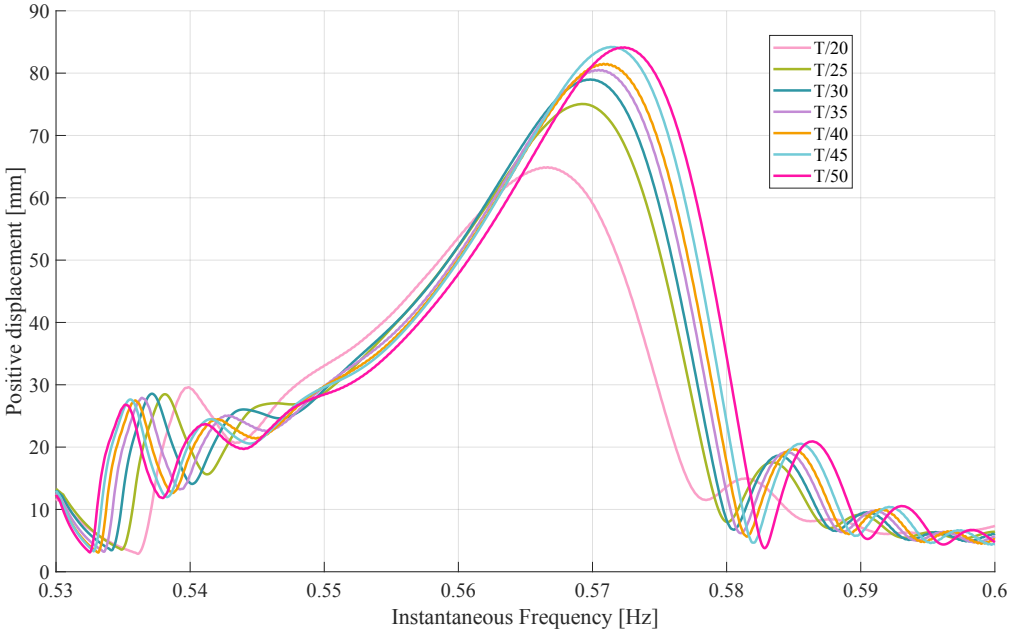

Figure 5.32: Positive envelope of the displacements based on the instantaneous frequency.

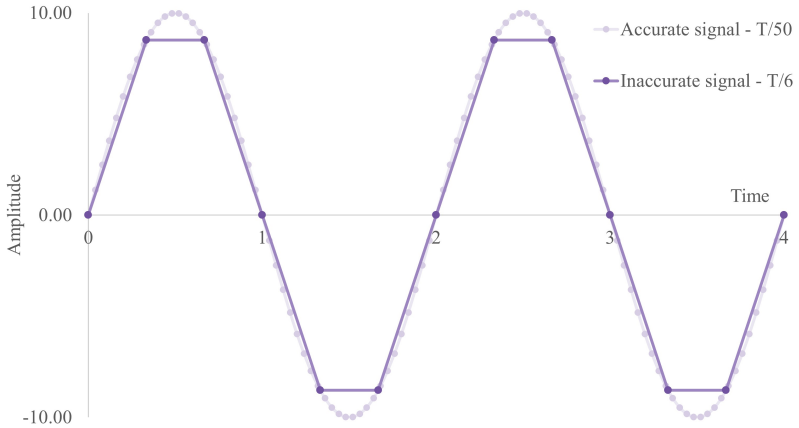

Figure 5.33: Example of distorted signal: the reconstruction of the signal never reaches the extrema of the sine.

The signal with the smallest time step (i.e. $T/50$) is considered as the reference response for accuracy. The computation of the difference will thus be relative to response $T/50$. It is defined as follows.

With y, the displacement response, t the time, and i, the sweep number $i = 7$ corresponding to $T/50$:

$$\varepsilon_{i,rel} = \frac{y_{max,7} - y_{max,i}}{y_{max,7}} \tag{5.34}$$

$$dt_i = \frac{t(y_{max,7}) - t(y_{max,i})}{t(y_{max,7})} \tag{5.35}$$

$$\tag{5.36}$$

	1	2	3	4	5	6	7
	$T/20$	$T/25$	$T/30$	$T/35$	$T/40$	$T/45$	$T/50$
y_{max} [mm]	64.89	75.05	78.98	80.51	81.48	83.97	84.12
$f(y_{max})$ [Hz]	0.5667	0.5692	0.5698	0.5705	0.5708	0.5714	0.5724
ε_{rel}	22.85 %	10.79 %	6.12 %	4.30 %	3.13 %	0.18 %	0.00 %
dt	1.00 %	0.56 %	0.45 %	0.33 %	0.28 %	0.17 %	0.00 %

Table 5.10: Summary of the main values used to compute the relative error of the accuracy of the results.

Table 5.10 shows that the relative difference in displacement is more impactful than the time shift. The time shift relative difference is negligible compared to the amplitude distortion, as it never exceeds 1 %. For this reason, it will not be taken into account in the computation of the final relative difference, as it would only contribute to a significant reduction of the global relative difference of all time steps without bringing any useful insight on the ideal time step. The relative difference in the amplitude is bigger than 20 % for $T/20$, although it is the most used time step in linear analysis, proving the importance of the sensitivity analysis on the time step in non-linear computations.

The computation time can be taken into account as well, as it can play a major role in simulations. To this end, the relative computation durations can be calculated, using again $T/50$ as the reference. Subsequently, the relative error and the relative simulation time can be summed, with or without a ponderation factor. In this analysis, accuracy has been preferred over computation time, and thus, an 85 - 15% of ponderation has been assigned to the results.

$$\tau_{t,i} = 1 - \frac{t_{tot,7} - t_{tot,i}}{t_{tot,7}} \tag{5.37}$$

$$\epsilon_i = 0.85 \cdot \varepsilon_{rel,i} + 0.15 \cdot \tau_{t,i} \tag{5.38}$$

	1	2	3	4	5	6	7
	$T/20$	$T/25$	$T/30$	$T/35$	$T/40$	$T/45$	$T/50$
t_{tot} [s]	1210	1380	1520	1735	2000	2325	2475
τ_t	48.91 %	55.87 %	61.66 %	70.28 %	81.05 %	94.05 %	100.00 %
ε_{rel}	22.85 %	10.79 %	6.12 %	4.30 %	3.13 %	0.18 %	0.00 %
ϵ_i	**26.76 %**	**17.55 %**	**14.45 %**	**14.20%**	**14.82 %**	**14.26 %**	**15.00 %**

Table 5.11: Summary of the main values used to compute the relative time of computation and result of the sensitivity analysis.

As Table 5.11 and Figure 5.34 show, the optimal time step for the model oscillates around $T/35$, depending on the importance given to the computation time. Time step $T/45$ is the second best choice, as the relative difference in amplitude is really small. In this case, a period of **$T/35$** is selected for all subsequent computations, as it is small enough to prevent major accuracy mistakes, while maintaining a reasonable computation time. The time step $T/40$, despite being close to $T/35$ in the overall results ϵ, requires 13 % of additional computation time but only increases accuracy by 1 %. Time step $T/35$ is thus preferred for all further computations.

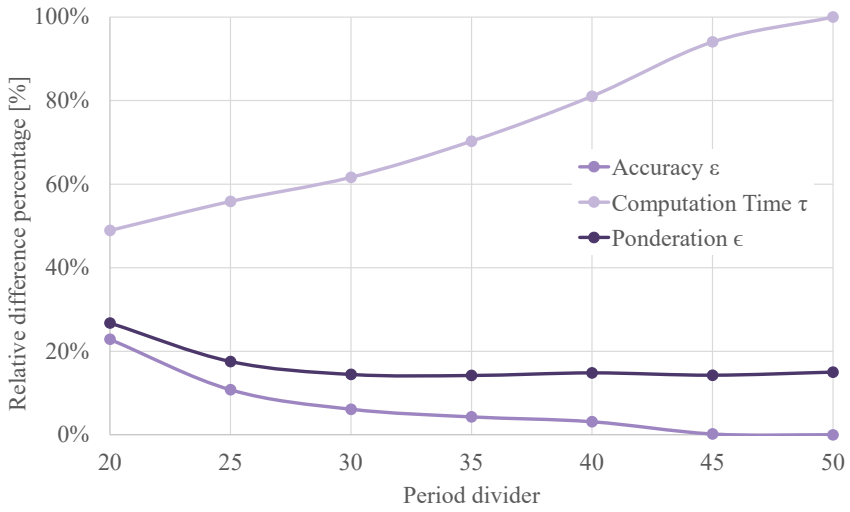

Figure 5.34: Sensitivity analysis - Evolution of the relative difference ϵ based on the period divider.

Sweep rate sensitivity

The sweep rate is very important when exciting a structure with a sine sweep. If the sine is too fast, a steady state regime will not settle, and transient effects could cloud the results. Transient effects increase the risks of inaccuracy of the results and can cause frequency jumps as represented in Figure 5.35. In order to avoid overly long simulations, the sensitivity analysis is performed on a simply supported beam with a first eigenfrequency close to the one of the bridge i.e. 0.575 Hz. The characteristics of the beam are listed in table 5.12.

b [mm]	h [mm]	ℓ[mm]	E [MPa]	ρ [kg/m^3]
50	50	15,000	210,000	7850

Table 5.12: Characteristics of the simply supported beam used to perform the sensitivity analysis.

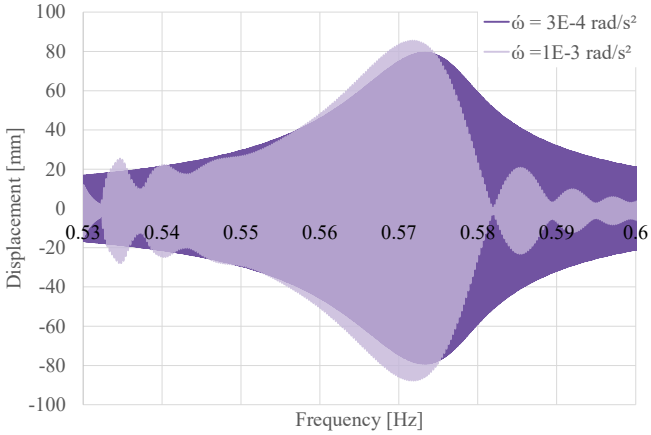

Figure 5.35: Comparison between the response of the structure for two sweep rates: 1E-3 and 3E-4 rad/s².

The first eigenfrequency of a simply supported beam is computed as follows:

$$f = \frac{1}{2 \cdot \pi} \cdot \left(\frac{\pi}{\ell}\right)^2 \cdot \sqrt{\frac{EI}{\rho}} = \frac{1}{2 \cdot \pi} \cdot \left(\frac{\pi}{10}\right)^2 \cdot \sqrt{\frac{109375}{19.625}} = 0.521 \text{ Hz} \tag{5.39}$$

Two configurations were tested: a beam with $\alpha = \beta = 0.3$ % and another with a $\alpha = \beta = 1$ % to compute the damping ratio, with 2 different criteria. Those values give a damping ratio value, for the first mode at 0.51 Hz of:

$$\xi_1 = \frac{\alpha}{2 \cdot \omega} + \frac{\beta \cdot \omega}{2} = 0.54\ \% \tag{5.40}$$

$$\xi_2 = \frac{0.01}{2 \cdot \omega} + \frac{0.01 \cdot \omega}{2} = 1.80\ \% \tag{5.41}$$

- Criterion for 1.8 % damping ratio [10]

$$\dot{\omega} \ll 2 \cdot \xi \cdot \omega^2 \tag{5.42}$$

- Criterion for the 0.54 % damping ratio [11]

$$\dot{\omega}_{max} < 7.2 \cdot \pi \cdot f^2 \cdot \xi^2 \tag{5.43}$$

These criteria result in the following minimal values for the sweeping rates:

A: 1 % damping ratio	B: 3 % damping ratio
0.385 rad/s²	$1.8 \cdot 10^{-4}$ rad/s²

Table 5.13: minimum sweep rate based on the criterion per damping.

Table 5.13 shows that the two criteria give very different sweep rates. The aim of the analysis is to perform multiple simulations of sweep with Criterion A, divided by different values and sweeping between 0.48 and 0.6Hz. Then, a simulation is run with Criterion B to compare the two limits on the sweep rate.

Sweep n°	Divider	$\dot{\omega}$ [rad/s²]	Nb iterations
1	200	$2.00 \cdot 10^{-3}$	4525
2	300	$1.28 \cdot 10^{3}$	7075
3	380	$1.00 \cdot 10^{-3}$	9050
4	450	$0.85 \cdot 10^{-3}$	10,650
5	500	$0.75 \cdot 10^{-3}$	12,070
6	600	$0.64 \cdot 10^{-3}$	14,142
7	1200	$0.32 \cdot 10^{-3}$	28,281
8	2400	$0.16 \cdot 10^{-3}$	45,000
9	crit.B	$0.05 \cdot 10^{-3}$	76,132

Table 5.14: Characteristics of the simulations for the sensitivity of the sweep rate.

As shown in Table 5.14, Criterion B leads to a significantly higher number of time steps, increasing computational cost. The purpose of this analysis is to assess whether similar levels of precision can be achieved using Criterion A instead, by adjusting the damping ratio. To do so, the bridge model is simulated using Criterion A, and the resulting response is evaluated. If the dynamic response is smooth and free of artificial oscillations, as illustrated in Figure 5.35, then the sweep rate criterion can be based on a $\alpha = \beta = 1$ % instead of 0.3 %. This higher damping level may be justified by the presence of friction between structural elements or numerical dissipation effects, both of which are common in such models. Using a higher damping ratio allows for slightly faster sweep rates, which in turn help to reduce overall

computation time without compromising accuracy. The objective is to define a sweep rate that is slow enough to minimize transient effects, while also ensuring alignment between the ramp-up and ramp-down sweeps. If the sweep rate is too high, there is a risk of peak misalignment in the system response, even if transient effects are negligible. Figure 5.36 illustrates this issue: although the response appears smooth, the peaks are shifted, indicating that the sweep rate is too high. For this reason, the simulations include a sine sweep of type ramp up, as well as a sine of type ramp down.

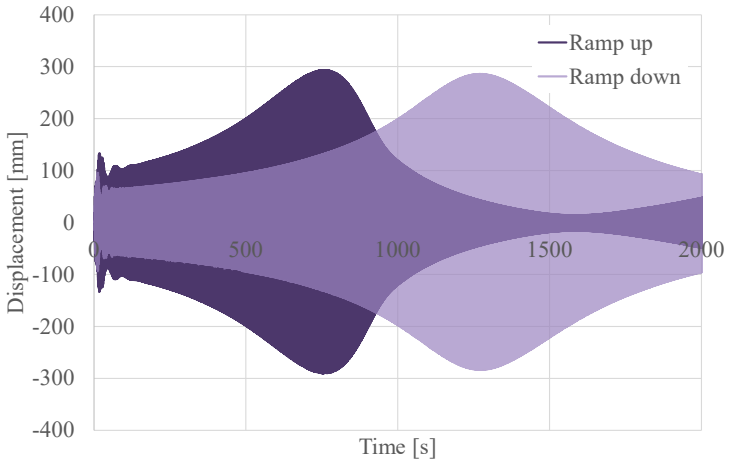

Figure 5.36: Result of a ramp up and a ramp down, performed with a sine sweep slow enough to avoid transient effects, but to not enough to reach steady state conditions.

The sine sweep is applied with an amplitude of 10 N. The expected response for the first mode can be computed as follows :

$$k_b = \frac{48 \cdot E \cdot I}{L^3} = \frac{48 \cdot 210{,}000 \cdot \frac{50^3 \cdot 50}{12}}{15{,}000^3} = 1.55 \text{ N/mm} \tag{5.44}$$

$$d_{static} = \frac{F}{k_b} = \frac{10}{1.55} = 6.42 \text{ mm} \tag{5.45}$$

$$d_{amp,\xi_1} = d_{static} \cdot \frac{1}{2 \cdot \xi} = 0.5 \cdot 6.42 \cdot \frac{1}{2 \cdot 0.018} \simeq 180 \text{ mm} \tag{5.46}$$

$$d_{amp,\xi_2} = \cdot d_{static} \cdot \frac{1}{2 \cdot \xi} = 0.5 \cdot 6.42 \cdot \frac{1}{2 \cdot 0.0054} \simeq 600 \text{ mm} \tag{5.47}$$

The simulation results, available in Figure 5.37, show that the response is smooth, with no artificial oscillations. In addition, the ramp up and ramp down produce about the same displacement. For the slower sweeping rates, the locations of the peaks are close to one another. These parameters indicate that the lower sweep rates seem to induce a steady state-like environment for the excitation of the structure. In order to determine the ideal sweeping rate, an analysis is performed based on several criteria:

1. the relative difference for $\dot{\omega}/2400$ and the other sweeping rates
2. the relative difference of the peak position compared the 0.3 % damping
3. the relative difference between the peak position of the ramp up and ramp down for each sweeping rate, as shown in Figure 5.39.

Figures 5.37 and 5.38 show that the sweep rate significantly impacts the peak displacement, with deviations up to 20 % for the fastest rates. In contrast, the peak positions vary by less than 2 % — even between

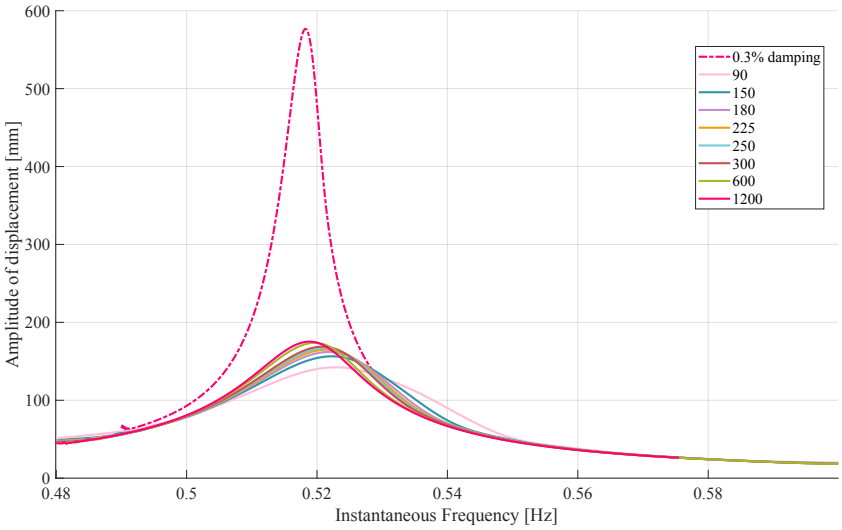

Figure 5.38: Envelope of the displacement based on the instantaneous frequency sweeped - Ramp down.

ramp-up and ramp-down, and relative to the 0.3 % damping case. This suggests that while faster sweeps maintain frequency alignment, they compromise amplitude accuracy. Figure 5.40 (a) shows that the relative difference in amplitude compared to $\dot{\omega}/2400$ decreases exponentially with decreasing sweep rate. The gain in precision from $\dot{\omega}/2400$ to $\dot{\omega}/1200$ is only 1 %, yet it nearly doubles the computational cost. Both amplitude and frequency shift metrics remain below 1 % at $\dot{\omega}/1200$, making it a reasonable trade-off for accuracy and efficiency.

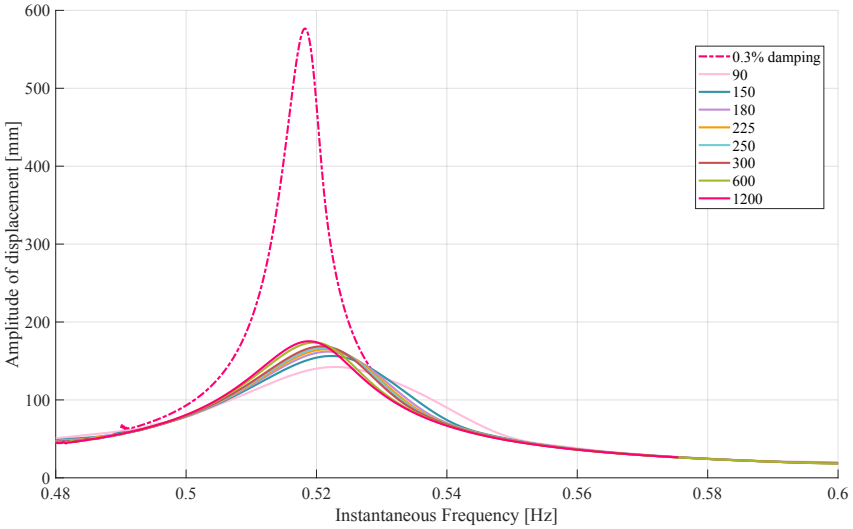

Figure 5.37: Envelope of the displacement based on the instantaneous frequency sweeped - Ramp up.

Figure 5.36 is the result of a test simulation on the bridge. It is excited with a sine sweep with a sweep rate computed with a criterion of type A, around $\dot{\omega}/100$ with an $\alpha = \beta = 1$ % for the damping ratio considered to compute the criterion. The sweep is smooth, even though the maximal values are not aligned. The absence of artificial oscillations proves that it is possible to consider a $\alpha = \beta = 1$ % when computing the sweep rate either with Criterion A or B. Nevertheless, the value of the divider has to be larger, around 1200, as determined earlier. However, the actual α and β in the model cannot be changed

to 1 %. These simulations only prove that external damping can be considered in the simulation of the bridge, that allows to sweep at a higher rate without compromising the data.

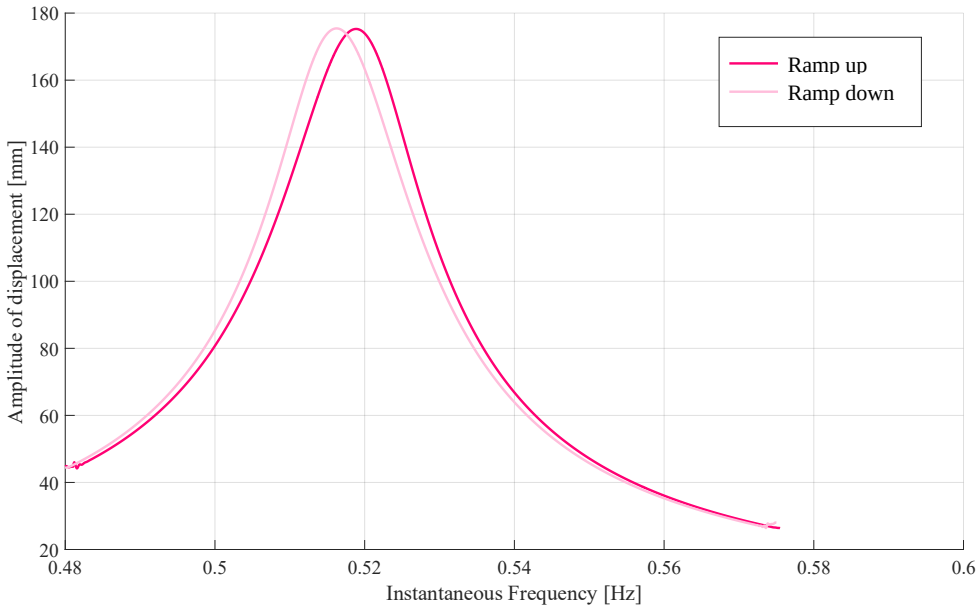

Figure 5.39: Comparison between the ramp up and ramp down for $\dot{\omega}/1200$.

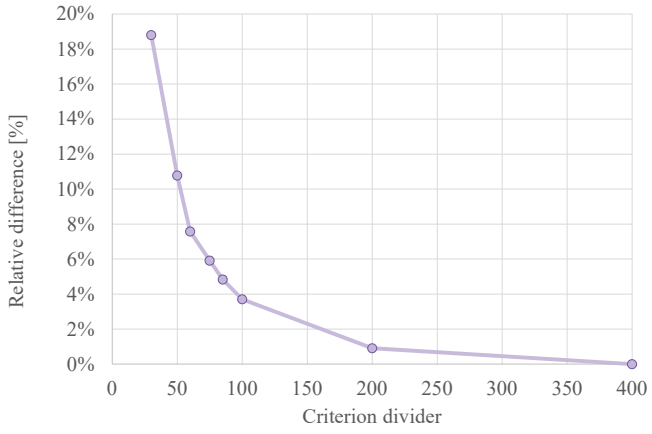

(a) Relative difference between the maximal value of the $\dot{\omega}/1200$ sweep and the other sweep rates.

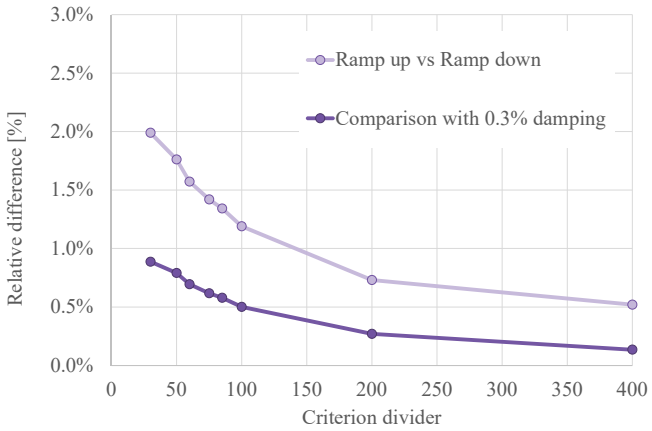

(b) Relative difference between the peak position of the ramp up and down and between the ramp up and the 0.3 % damping value.

Figure 5.40: Envelope of the displacement based on the instantaneous frequency sweeped - Ramp up and down.

Sine sweeps

Now that the model has been calibrated, that eigenfrequencies and mode shapes are known, and sensitivity analyses have been completed, it is possible to proceed with non-linear step-by-step simulations on the bridge. The goal of this phase is to apply sine sweep excitations to the bridge deck, where the amplitude increases progressively with each sweep. These sine sweeps are centered around one eigenfrequency of the structure. Their purpose is to compare the non-linear structural response to the

linear response, in order to quantify the extent of non-linearities in the bridge's behaviour. To fully characterize the system, both ramp-up and ramp-down sine sweeps are used, allowing the reconstruction of the Frequency Response Functions (FRFs), which are then compared to the linear FRFs.
The first vertical mode is selected for this analysis because it has the highest modal participation factor and is supposed to be damped by the TMDs. They are thus modelled in the simulation in order to assess their effectiveness in reducing displacements. In addition, alternative damper configurations are explored to determine the most efficient setup.

The first mode occurs at a frequency of 0.575 Hz, so the sine sweep ranges from 0.525 Hz to 0.62 Hz, to ensure the sweep captures the peak response region. The full set of parameters used for the sine sweeps and the simulations is summarized in Table 5.15. The sweep rate can be decided for, based on the criteria used for the sensitivity analysis, and considering a damping of 1 %:

$$\text{Citerion A :} \quad \dot{\omega}_{max,1} < \frac{2\cdot\xi\cdot\omega^2}{1200} = \frac{2\cdot 0.02\cdot(0.575\cdot 2\cdot\pi)^2}{2400} = 4.35\cdot 10^{-4}\ \text{rad/s}^2 \quad (5.48)$$

$$\text{And :} \quad \dot{\omega}_{min} > \frac{2\cdot\xi\cdot\omega^2}{1200} = \frac{2\cdot 0.02\cdot(0.575\cdot 2\cdot\pi)^2}{1200} = 2.18\cdot 10^{-4}\ \text{rad/s}^2 \quad (5.49)$$

$$\text{Criterion B :} \quad \dot{\omega}_{max,2} < 7.2\cdot\pi\cdot\omega^2\cdot\xi^2 = 7.2\cdot\pi\cdot(0.575\cdot 2\cdot\pi)^2\cdot 0.02^2 = 3.0\cdot 10^{-4}\ \text{rad/s}^2 \quad (5.50)$$

$$\Rightarrow \dot{\omega} \in [2.18\cdot 10^{-4}\ ;\ 4.35\cdot 10^{-4}] \Rightarrow \dot{\omega} = 2.9\cdot 10^{-4}\ \text{rad/s}^2 \quad (5.51)$$

Nb. sweeps	Range [Hz]	$\dot{\omega}$ [rad/s²]	Amplitude ranged [N]	Time step [s]	Nb steps	Duration
8	[0.525 ; 0.62]	$2.9\cdot 10^{-4}$	500 to 10,000	$\frac{1}{0.65\cdot 35} = 0.044$	46,828	8000 s ≃ 2h15

Table 5.15: Sine sweeps and simulation characteristics.

NB: The results of these simulations will be analyzed in the next chapter.

5.4 Conclusion

Although the objective was to keep the characteristics as close as possible to reality, some adjustments and simplifications were necessary to facilitate the modelling process. In particular, the cross-beams and longitudinal section had to be simplified. To enable linear numerical computations on the bridge, the hangers were layered with 3-D springs, providing lateral stiffness to the main suspension cables. Regarding the non-linear computation, residual forces were introduced in the main cables to simulate the cable return effect. Residual forces were also applied to the hangers to replicate the tension distribution pattern identified during the analysis of experimental data. The modal behaviour of the bridge aligns with the experimental data within a margin of 10 % difference, and even more closely for the higher modes. However, an issue was identified with the support conditions, particularly in the limitation of horizontal displacements. This constraint introduces excessive lateral stiffness in the deck, resulting in higher modal frequencies than those observed using the *COV-SSI* method.

Additionally, a preliminary design of the TMD was carried out, and its effectiveness was tested with a linear analysis. Finally, a sensitivity analysis on both the time step and sweep rates was conducted, leading to a set of criteria and limitations established to ensure the accuracy and reliability of the numerical model. All these computations and sensitivity analyses eventually lead to a set of non-linear step-by-step analyses. Their purpose is to excite the bridge at different amplitude level, from 500 to 15,000 N, in order to study the response and quantify the level of non-linearity of the bridge. Three other simulations are conducted as well with the objective of examining the effect of the non-linearity on the efficiency of the TMDs.

6 Results

This section presents the results from a series of **non-linear step-by-step analyses under harmonic excitation**. A total of nine non-linear simulations were performed using a sine sweep load with an increasing force amplitude, ranging from 500 N to 15,000 N. This force range was selected to determine the threshold beyond which the bridge deviates from linear behaviour and exhibits signs of non-linearities. The transition from linear to non-linear dynamics is evaluated by comparing the displacement and amplification levels obtained from the non-linear simulations against those predicted by an equivalent linear analysis. Moreover, particular attention is paid to the eigenfrequency shift with the increase of the amplitude of the excitation. Subsequently, the performance of the TMD under harmonic load of 10,000 N is assessed. Three different TMD configurations are analysed to evaluate their influence on the dynamic response and damping performance of the bridge:

- the original TMD design, as proposed by *Ruscheweyh Consult*, with a mass ratio μ of 3 %
- a TMD tuned on the frequency identified in the sine sweep analysis, with a mass ratio μ of 3 %
- the original TMD design, as proposed by *Ruscheweyh Consult*, with a mass ratio μ of 1 %

These analyses allow for an assessment of both the effectiveness of the TMD tuning strategy and the influence of the mass ratio on the damping of the vibration. The results emphasize the importance of conducting non-linear analyses when designing damping systems. Moreover, the comparison provides insight into the potential benefits or limitations of downsizing control devices in the context of non-linear structural dynamics.

NB: In this section, sine sweeps going from low to high frequencies will be referred to as "sine sweeps", whereas sine sweeps going from high to low frequencies will be referred to as "inverted sine sweeps"

6.1 Analysis of the non-linearities

All results are extracted at a single representative point on the structure, i.e. the anti-node of the first vertical mode at 0.575 Hz, as this location exhibits the maximum displacement amplitude of the entire bridge during dynamic excitation.The results obtained from `Finelg` are post-processed using the Hilbert Transform to extract the envelope of the oscillatory response.

Equivalent Linear analysis

The linear equivalent structure (structure with an initial deformation, corresponding to the deformed shape under self-weight from the non-linear analysis) is slightly different from the non-linear one. As computed earlier with the modal analysis, the first eigenfrequency is higher for this structure (0.62 Hz). The expected displacement for an excitation of 500 N in a linear analysis can also be estimated in order to

validate the numerical model:

$$q_s = \frac{F}{k} = \frac{500}{581{,}464} = 0.85 \text{ mm} \tag{6.1}$$

$$q_{amp} = \frac{q_s}{2 \cdot \xi} = \frac{1.19}{2 \cdot 0.0062} = 69 \text{ mm} \tag{6.2}$$

The linear analysis on the linear equivalent structure results in a maximal displacement of 65 mm, close to the computed value. The response is not exactly identical, as that quick estimate is mainly used to have an order of magnitude to validate the model, rather than an exact solution for the displacement. Figure 6.1 (a) illustrates the result of the numerical analysis. The displacement is maximal around 0.615 Hz, close to the value identified in the modal analysis. It is possible, through the computation of the quality factor, to verify the value of the damping ratio. The approximate half-power points are identified in Figure 6.1 (b). Equations (6.3) to (6.6) show that the damping ratio computed through the result of the sine sweep is around 0.65 %, close to the 0.62 % implemented in the model. That slight variation can be caused by numerical damping.

$$q_{\sqrt{2}} = \frac{q_{max}}{\sqrt{2}} = 45.5 \text{ mm} \tag{6.3}$$

$$f_a = 0.609 \text{ Hz} \;\; \& \;\; f_b = 0.617 \text{ Hz} \tag{6.4}$$

$$Q_{lin} = \frac{\omega_s}{\omega_b - \omega_a} = \frac{3.058}{3.877 - 3.826} = 76.75 \tag{6.5}$$

$$\xi_{lin} = 0.65 \text{ \%} \tag{6.6}$$

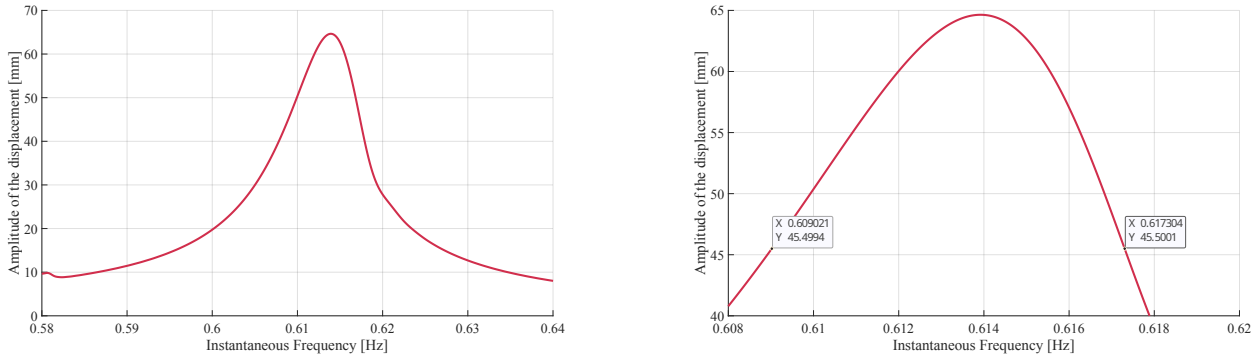

(a) Envelope of the linear response of the structure excited by a sine sweep of 500 N.

(b) Zoom on the peak of the linear response to determine the quality factor.

Figure 6.1: Envelope of the linear response of the structure excited by a sine sweep of 500 N.

As the performed analysis is linear, the results from the sine sweep and inverted sine sweep are expected to be similar. Indeed, the response of a linear structure does not depend on the way the excitation is applied. In the case of the sine sweep, the response under a sine sweep and an inverted sine sweep should be exactly the same. Therefore, the FRF of the linear structure is symmetrical. For that reason, the relative difference of the misalignment of the peaks between the response of the sine sweep and inverted sine sweep is computed. This difference quantifies the numerical error of the model which can be subsequently subtracted from the non-linear results. Henceforth, any misalignment remaining in the non-linear analysis is the consequence of the non-linearities developed in the bridge, and not the result of a numerical error.

$$\varepsilon_{num} = f_2 - f_1 = 0.6139 - 0.6118 = 2.1 \cdot 10^{-3} \text{ Hz} \tag{6.7}$$

$$\epsilon_{rel} = \frac{\varepsilon}{f_1} = \frac{2.1 \cdot 10^{-3}}{0.6118} = 0.34 \text{ \%} \tag{6.8}$$

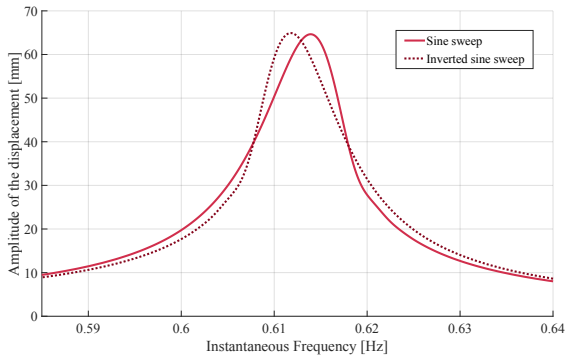

(a) Envelopes of the structure linear response, excited by a sine sweep and inverted sine sweep of 500 N.

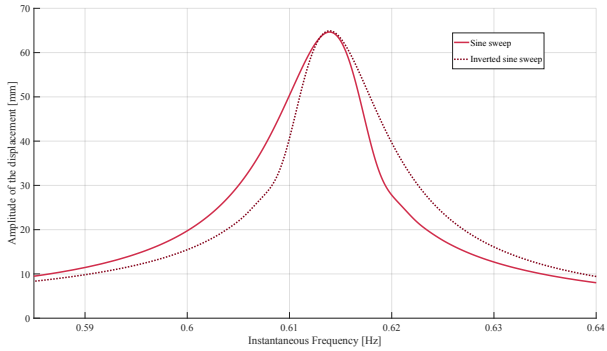

(b) Realigned envelopes of the structure linear response, excited by a sine sweep and inverted sine sweep of 500 N

Figure 6.2: Aligned envelopes of the linear response of the structure excited by a sine sweep and inverted sine sweep of 500 N.

Non-linear analyses

As the linear response is known, and the numerical error is quantified, it is now possible to study the responses of the non-linear analyses. To this end, nine sine sweep and nine inverted sine sweep simulations were prepared, with the exact same characteristics, except for the amplitude of the force applied to the deck. This way, the non-linear behaviour can be highlighted, as all other characteristics remain identical between the simulations. In linear analyses, superposition of displacements, forces and stresses is applicable. This is not the case in non-linear analysis, as the forces are not linearly related to displacements, as shown in equation (6.10). Therefore, the self-weight and the sine sweep have to be applied in the same simulation. As a matter of fact, the displacement caused by the self-weight induces stresses in the cables that contribute to the stiffness of the bridge, and overlooking those stresses is not representative of the real behaviour of the bridge.

$$\text{Linear analysis:} \quad F = k \cdot x \Rightarrow F(x_1 + x_2) = F(x_1) + F(x_2) \tag{6.9}$$

$$\text{Non linear analysis:} \quad F = k_1 \cdot x(t) + k_2 \cdot x^2(t) + k_3 \cdot x^3(t) \Rightarrow F(x_1 + x_2) \neq F(x_1) + F(x_2) \tag{6.10}$$

The loading sequence in the software `Finelg` must be taken into consideration. In dynamic step-by-step analyses, the self-weight is applied as an instantaneous force. Therefore, the model has to stabilize under the self-weight force before applying the sine sweep force. Otherwise, the forces will interfere and distort the results. A period of settlement has to be planned before starting the sine sweep, but a very precise time step is not required, as this is not the important part of the simulation. The additional computation time is equal to the time of settlement, computed in equation (6.11).

$$t_R = \frac{T}{2 \cdot \xi} = \frac{\frac{1}{0.575}}{2 \cdot 0.0058} \simeq 150 \text{ s} \tag{6.11}$$

The decaying response of the self-weight tends toward the deformed configuration computed earlier in the static analysis. Thus, the reference node used in the analysis to extract the response of the sine sweep has an initial displacement. To be able to use the Hilbert Transform, that initial displacement has to be removed from the displacement response to realign the signals to zero and, hence return to a symmetrical displacement configuration. This modification is essential to correctly assess the value of the amplification between two different force amplitudes for example. Equations (6.13) to (6.14) illustrate that concept.

Indeed, the amplification ratio with unmodified results is completely different from the same ratio with modified results. A_0 overlooks the linear behaviour of the model and could lead to wrong conclusions. Removing the initial displacement of the deck highlights the displacement due to the vibrations and isolate the part that can bring forth possible non-linear behaviour.

$$d_0 = 150 \text{ mm} \ ; \ d_{500} = 160 \text{ mm} \ ; \ d_{1000} = 170 \text{ mm} \tag{6.12}$$

$$A_0 = \frac{d_{1000}}{d_{500}} = \frac{170}{160} = 1.06 \tag{6.13}$$

$$A_1 = \frac{d_{1000} - d_0}{d_{500} - d_0} = \frac{170 - 150}{160 - 150} = \frac{20}{10} = 2 \tag{6.14}$$

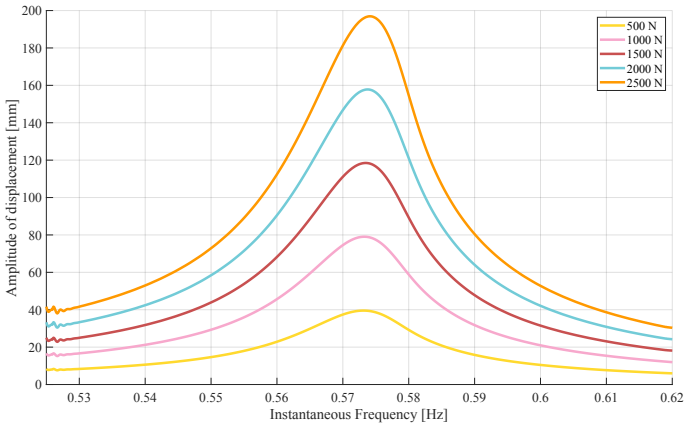

(a) Zoom on the envelope of the response of the structure excited by sine sweeps for lower amplitudes.

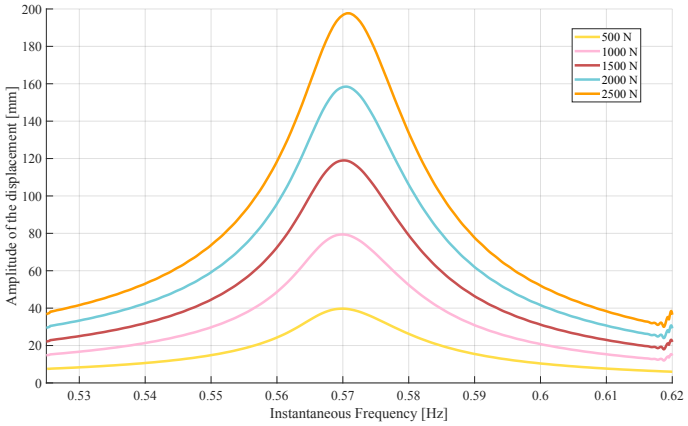

(b) Zoom on the envelope of the response of the structure excited by inverted sine sweeps for lower amplitudes.

Figure 6.3: Results of time-displacement relation of the structure excited by sine sweeps at low amplitudes.

Figure 6.3 represents the envelope of the realigned results of the sine sweeps (a) and inverted sine sweeps (b) at a low amplitude, i.e. between 500 and 2500 N. The higher amplitude responses are not represented to avoid a flattening effect of the smaller responses. Those results seem fairly similar and symmetrical in shape. Moreover, the maxima of each curve seem to be relatively proportional and the peak frequency does not seem to shift from one envelope to another.

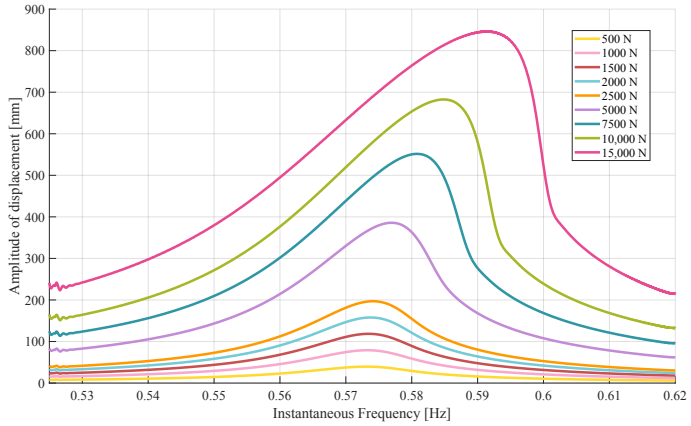

(a) Envelope of the response of the structure excited by sine sweeps at different amplitudes.

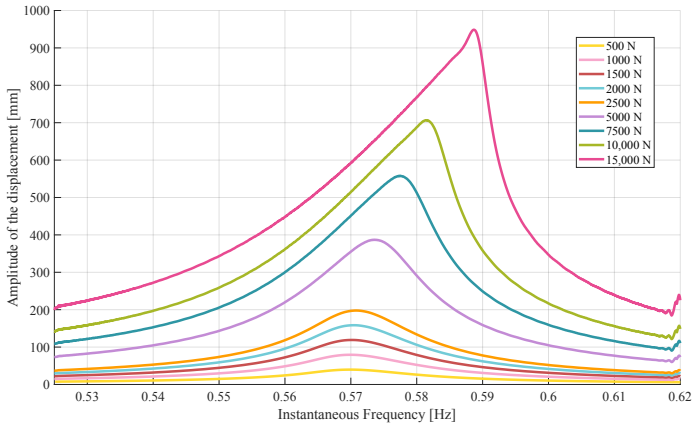

(b) Envelope of the response of the structure excited by sine sweeps at different amplitudes as a function of frequency.

Figure 6.4: Envelope of the response of the structure excited by a sine sweep and an inverted sine sweep at different amplitudes as a function of frequency.

When adding the higher amplitude results, as represented in Figure 6.4, it appears that non-linearities are starting to develop. First of all, the envelope shapes of the sine sweep and inverted sine sweep are different, as opposed to what is expected with a linear behaviour. The inverted sine sweep has a sharper shape, with a noticeable peak for the higher force amplitudes.
Second, in both Figure 6.4 (a) and (b), the peak position of the envelopes shifts towards higher frequencies with the increase of the force, as highlighted in red in Figure 6.5. That behaviour is no surprise, as the increase of tension in the cables due to higher forces tends to an overall stiffening of the bridge. This hardening effect leads to higher resonant frequencies and thus, a discrepancy between the peak frequency at low amplitude and at high amplitude. This proves that high forces are needed to trigger a non-linear behaviour, but they could occur in the lifetime of a bridge, and could be triggered in higher class footbridges, such as class I. This gap evolves with the force and is computed in Figure 6.6, which represents the relative difference between the frequency identified at the peak value of the envelope and the frequency associated with the 500 N envelope. The maximal relative deviation does not exceed 3.5 %. Nevertheless, such deviation could be sufficient to affect the efficiency of a TMD. It seems to be noticeable around 5000-7500 N whereas the differences between the envelope shapes are noteworthy around 7500 N. The non-linearity threshold is probably located between 5000 and 7500 N.

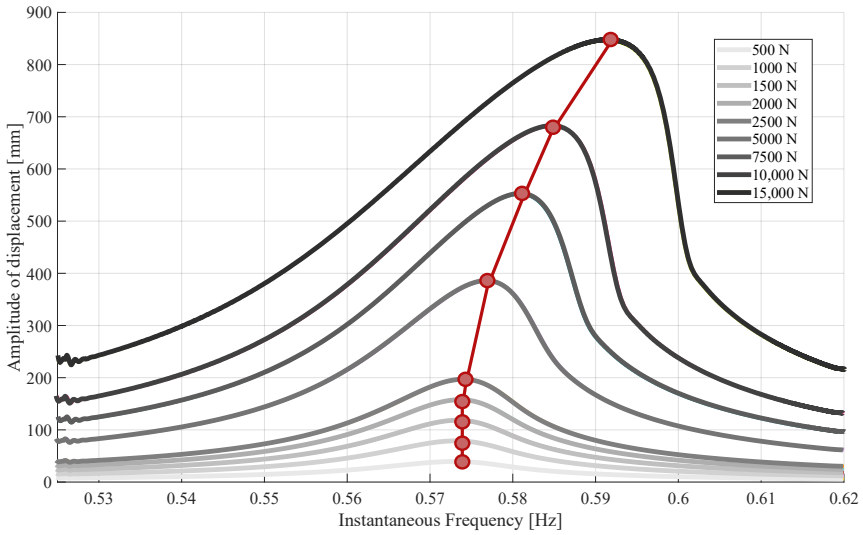

Figure 6.5: Highlight of the frequency deviation with the increase of the amplitude of the force imposed on the structure.

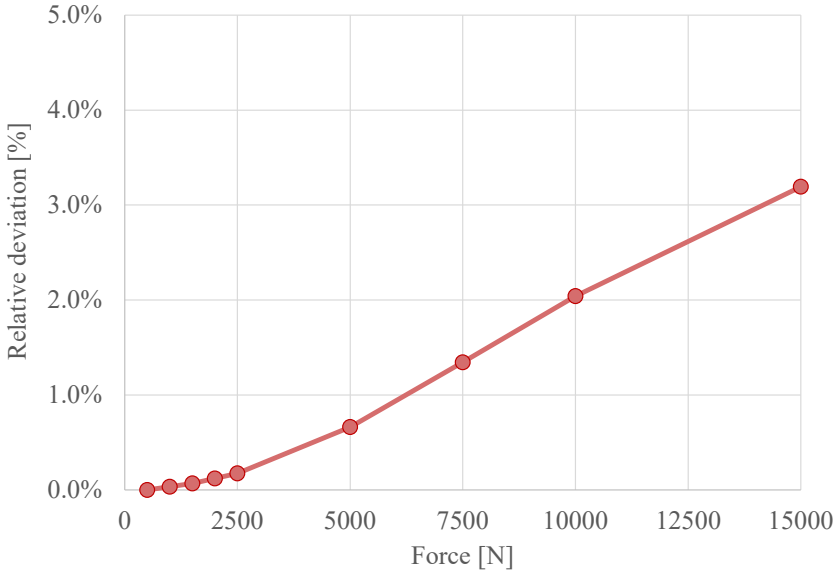

Figure 6.6: Relative deviation of the frequency based on the frequency associated to the peak displacement value at 500 N.

To substantiate this assumption, the maximum value of each response is normalized by the maximum value obtained under a 500 N amplitude, as defined in Equation (6.15). The amplification ratios are summarized in Table 6.1 and visualized in Figure 6.7.

$$R_{d,i} = \frac{\max(d_i)}{\max(d_1)} \text{ [mm]/[mm]} \tag{6.15}$$

$$R_{F,i} = \frac{F_i}{F_1} = \frac{F_i}{500} \text{ [N]/[N]} \tag{6.16}$$

$$\text{Linear behaviour} : R_{d,i} = R_{F,i} \tag{6.17}$$

In Figure 6.7, the global shape of the non-linear curve appears to follow a cube root trend. This is consistent with the fact that the restoring force is modelled by a third-degree equation. This behaviour aligns with the expected dynamic response: as stiffness increases, the displacement increases more slowly than the force. This reflects a physical limitation of the system: cables cannot accumulate stiffness indefinitely. Past the linear threshold, stiffness grows rapidly, then gradually levels off, as the material structure becomes fully engaged and can no longer significantly resist additional deformation. Eventually, the system approaches its maximum stiffness before failure.

On the contrary, in Figure 6.8, the relative difference between the non-linear amplification ratio and the linear amplification ratio (R_{d_i}) for the same force level increases progressively faster. This divergence follows an approximately cubic trend, representing the delay of the non-linear response and, once that threshold is overcome, the stabilization of the amplification ratio, opposed to the linear amplification ratio, that keeps increasing. That relative difference in computed as follows:

$$\Delta_{amp,i} = \frac{R_{d,i,lin} - R_{d,i,non-lin}}{R_{d,i,lin}} \tag{6.18}$$

	Applied Force [N]	Ratio [N/N]	Peak displacement [mm]	Ratio [mm/mm]
1	500 N	1	39.50	1
2	1000 N	2	78.98	1.99
3	1500 N	3	118.39	2.99
4	2000 N	4	157.67	3.99
5	2500 N	5	196.77	4.98
6	5000 N	10	380.50	9.75
7	7500 N	15	551.28	13.95
8	10,000 N	20	682.27	17.27
9	15,000 N	30	846.14	21.42

Table 6.1: Results of the computation of the amplification ratios.

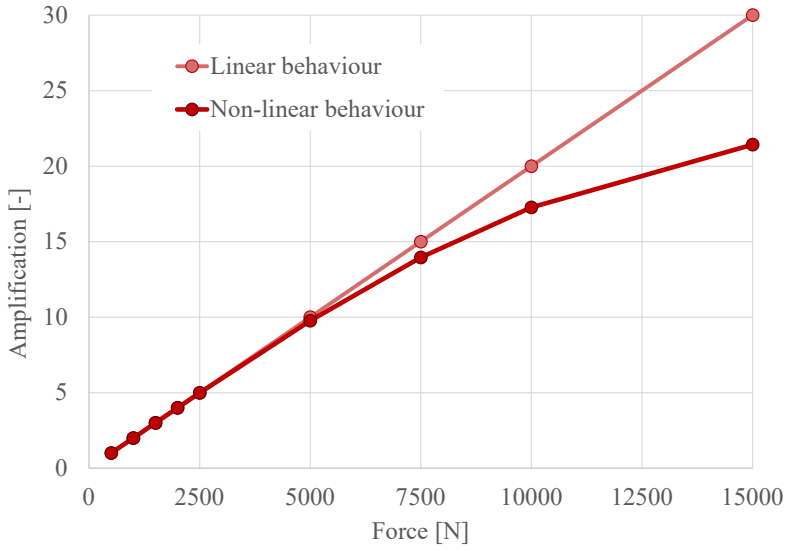

Figure 6.7: Results of the computation of the amplification ratios.

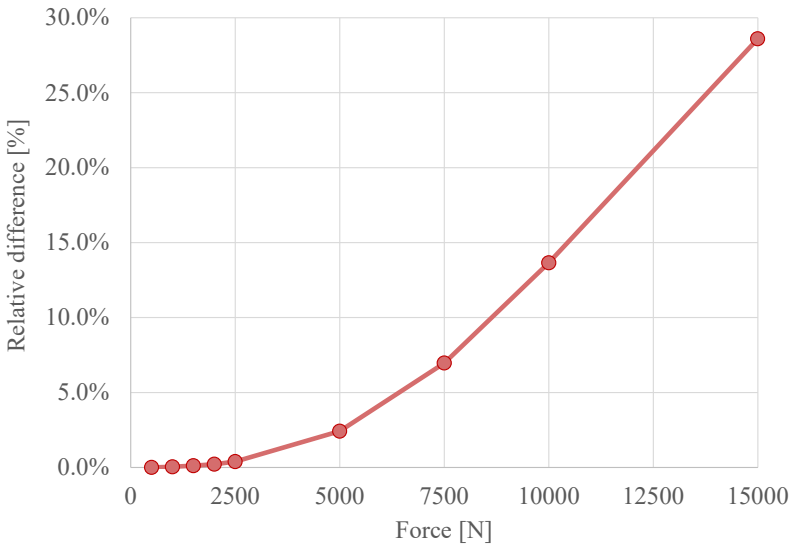

Figure 6.8: Relative difference between a linear amplitude ratio and the non-linear amplitude ratio at the same force level.

Another point of interest of these results is the difference between the displacement under a force of 500 N in linear versus non-linear analysis. Where the linear analysis predicts a displacement of 64 mm, the non-linear one computes a displacement of only 39.5 mm. As seen in Figure 6.9, the linear analyses have a tendency to overestimate the results, as well as the amplification ratios. It can be really misleading at high amplitude, where the displacement can be overestimated up to 5.5 times. That difference can be explained by the fact that the non-linear model is stiffer than the linear model, as the evolution of stiffness is taken into account. At low amplitudes, the behaviour of the non-linear model remains effectively linear-like. The variation in stiffness across force levels is not sufficient to disrupt the proportional relationship between the amplification ratios. Nevertheless, the non-linear model exhibits slightly greater stiffness than the linear model even at low amplitudes, resulting in reduced displacements.

The damping ratio can be computed with the quality factor methods, as in equations (6.3) to (6.6). Results in Table 6.2 gives the impression that the damping is widely increased by the non-linearity, as it almost reaches 2.7 % for a force of 15,000 N. However, this is not a realistic computation of the damping ratio. As the applied force varies, the stiffness of the structure evolves accordingly, leading to a real-time change in its eigenfrequency. Specifically, the eigenfrequency increases with increasing stiffness. At higher force levels, the stiffness undergoes more significant variation, resulting in a broader range of eigenfrequencies being excited with notable amplitudes. Consequently, this behaviour causes an expansion of the resonance peak in the system frequency response. When performing a quality factor analysis on the response, the damping ratio seems higher than it actually is. This technique should not be applied to non-linear frequency responses, as it results in spurious results.

	500 N	15,000 N
Half-power value [mm]	28.280	598.000
f_a [Hz]	0.564	0.567
f_b [Hz]	0.580	0.599
Q [-]	35.812	18.593
ξ [-]	1.340 %	2.690 %

Table 6.2: Step-by-step values for the computation of the damping ratio based on the quality factor.

*NB: In `Finelg`, the damping ratio of the model remains constant and does not evolve with changes in stiffness, as it is computed solely from the **initial** stiffness matrix and is not updated during the analysis. Consequently, the defined damping ratio remains fixed throughout the entire computation process.*

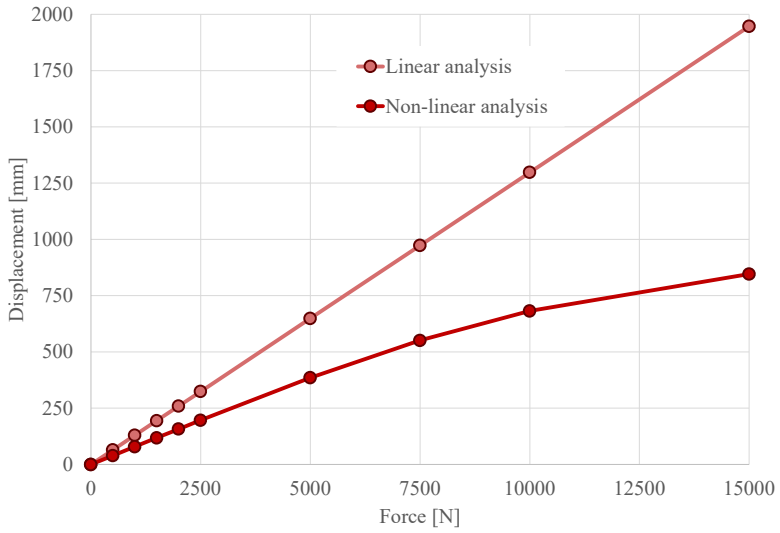

Figure 6.9: Comparison of the displacement under sine sweeps with varying amplitudes in linear analysis and non-linear analysis.

By dividing the response envelopes by the corresponding applied forces, the resulting normalized responses approximate the shape of the FRF. Plotting the normalized envelopes from both the sine sweep and the inverted sine sweep provides insights on the qualitative shape of the FRF as well as the structure stiffness characteristics, as the displacement divided by the force indicates the value of the flexibility (inverse of the stiffness).

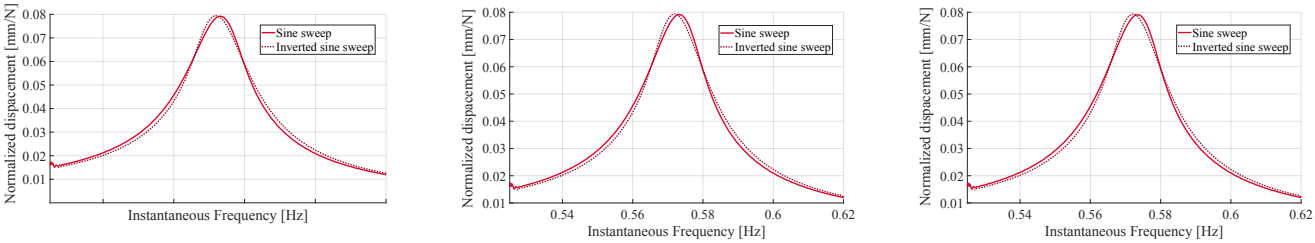

(a) Amplitude = 500 N. (b) Amplitude = 1000 N. (c) Amplitude = 1500 N.

Figure 6.10: Normalized displacements for a sine sweep and inverted sine sweep at different amplitudes

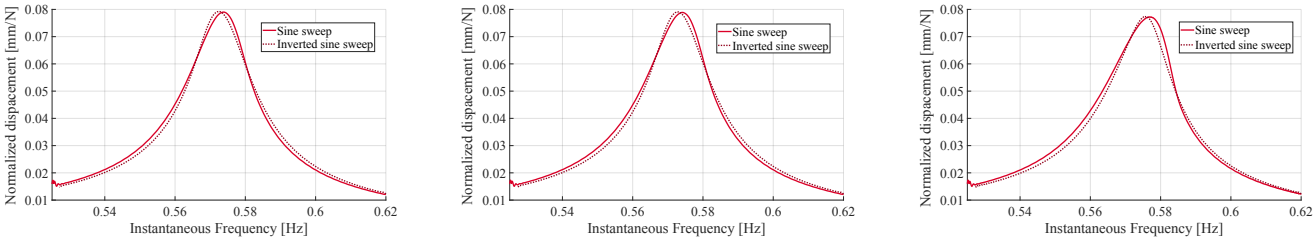

(a) Amplitude = 2000 N. (b) Amplitude = 2500 N. (c) Amplitude = 5000 N.

Figure 6.11: Normalized displacements for a sine sweep and inverted sine sweep at different amplitudes.

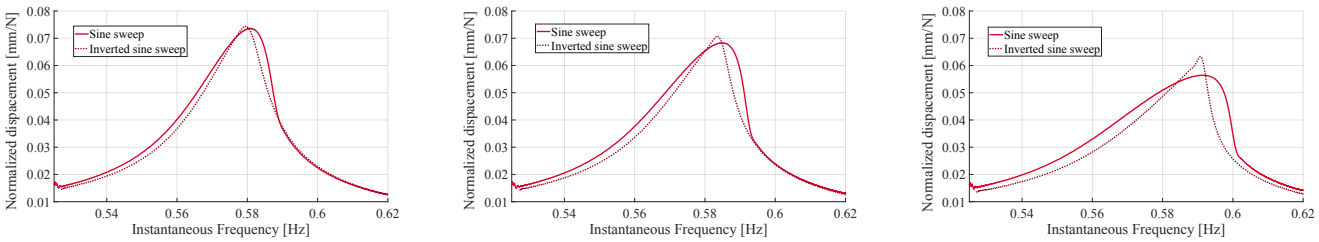

(a) Amplitude = 7500 N. (b) Amplitude = 10,000 N. (c) Amplitude = 15,000 N.

Figure 6.12: Normalized displacements for a sine sweep and inverted sine sweep at different amplitudes.

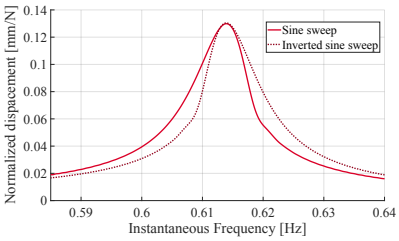

Figure 6.13: Normalized displacements for linear sine sweep and linear inverted sine sweep at 500 N.

Figures 6.10 to 6.13, show that the 5 first FRFs are very similar, and then the inverted sine sweep starts to disassociate from the sine sweep, leading to a different shape for the reconstructed FRF. In addition, it is possible to associate a stiffness to the maximal value of the FRF, by taking the inverse of the peak value. As expected, Figure 6.14 shows that 15,000 N is associated with the highest stiffness and the first low amplitude result in a constant stiffness, sign of linearity. In addition, the stiffness of the linear model is lower than the one of the non-linear model, explaining the difference in displacement in amplitude at 500 N between the linear and non-linear models. The FRFs can be reconstructed from Figures 6.10 to 6.12. Figure 6.15 shows that the first low-amplitude envelopes result in a very similar FRF whereas,

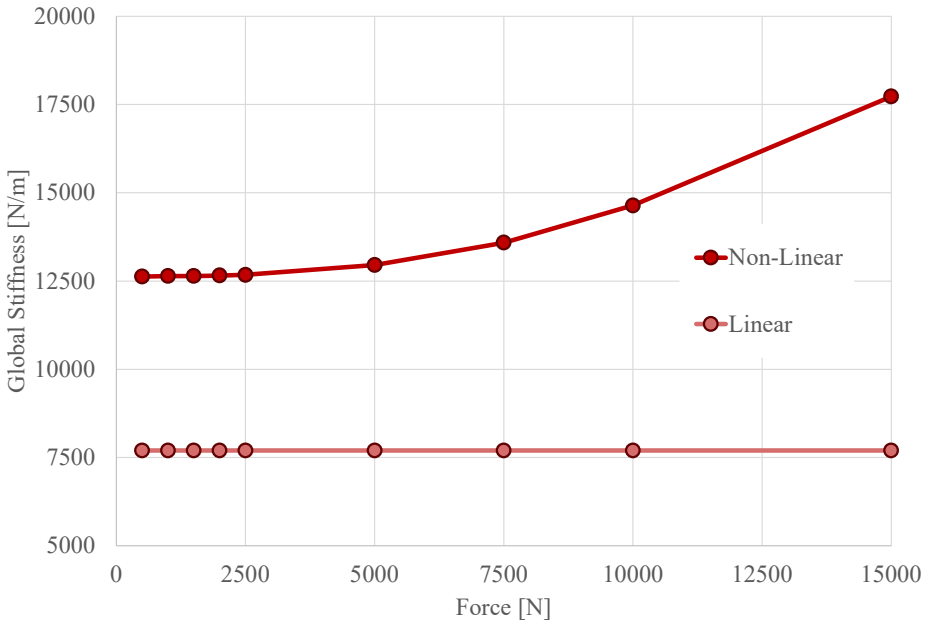

Figure 6.14: Evolution of the stiffness base on the amplitude of the force applied in a linear analysis versus a non-linear analysis

with the increase in non-linearity, the FRF tends to get broader and flatter, representing respectively the multiple frequencies respondent with high displacement and the decrease in amplification due to the stiffness increase.

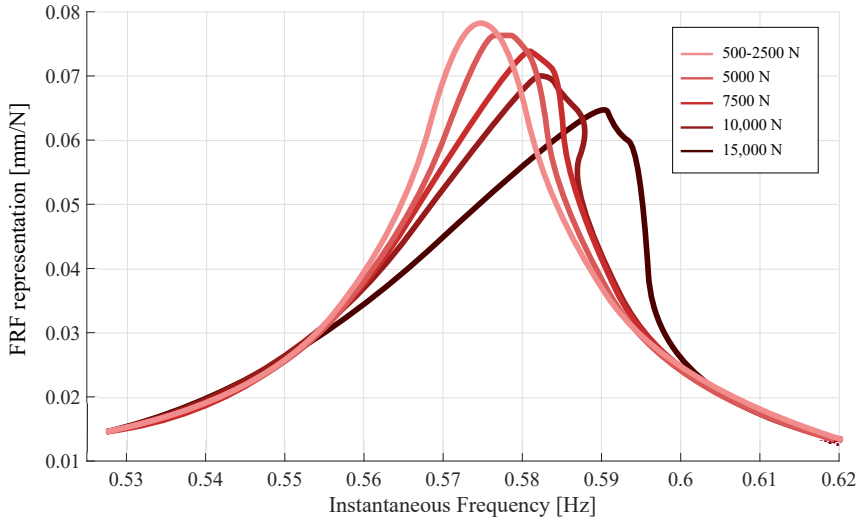

Figure 6.15: Reconstructions of the FRFs based on the amplification levels.

Acceleration levels

The linear analysis tends to overestimate the displacements of the bridge when it is subjected to resonance. Since the acceleration levels are directly proportional to the square of the resonance frequency and the displacement amplitude, the acceleration is overestimated as well. As TMD design is highly sensitive to predicted resonance amplitudes, relying on linear analysis may lead to oversized or unnecessarily deployed dampers. Consequently, a non-linear analysis may significantly alter the strategy for implementing TMDs. In practice, the decision to install a TMD is primarily based on two criteria:

- the estimated potential number of pedestrians synchronized at the eigenfrequency of the bridge and triggering resonance
- the acceleration levels to damp

These criteria are defined according to the classification of the bridge. The Victor-Neels footbridge is categorized as a Class III structure, for which minimal comfort requirements apply. For the eigenfrequency under consideration, 0.575 Hz, the SETRA guidelines recommend limiting peak accelerations within the range of 1 m/s² to 2.5 m/s². The previously computed displacements can be converted into equivalent accelerations, and the applied force amplitude from the sine sweep can be expressed in terms of an equivalent number of pedestrians.

NB: the SETRA guidelines recommend an average dynamic weight for a pedestrian of $G_{dyn} = 0.4 \cdot G = 0.4 \cdot 75 \cdot 9.81 \simeq 295\ N$.

Table 6.3 shows that, as expected, the linear acceleration levels are larger than those resulting from the non-linear analysis. Based solely on the linear results, the comfort limit is exceeded at a force amplitude of 1500 N, corresponding to approximately 5 equivalent pedestrians. However, the non-linear analysis indicates that this limit is only reached at 2500 N, or about 9 equivalent pedestrians. The equivalent number of pedestrians can be interpreted in terms of pedestrian flow crossing the bridge by squaring the

value. The pedestrian flow x^2 represents the total number of people needed on the bridge simultaneously so that x pedestrians are randomly synchronized at the targeted frequency. However, in this case, the probability that pedestrians synchronize themselves at 0.575 Hz while walking is highly improbable, as typical walking frequencies range from 1.7 to 2.1 Hz.

	Applied Force [N]	Eq. pedestrian	Lin. acceleration [m/s²]	Non-lin. acceleration [m/s²]
1	500 N	1.7 ≃2	0.97	0.52
2	1000 N	3.4 ≃4	1.95	1.04
3	1500 N	5	2.93	1.54
4	2000 N	6.8 ≃ 2	3.90	2.06
5	2500 N	8.5 ≃ 9	4.88	2.57
6	5000 N	17.0	9.77	5.03
7	7500 N	25.4 ≃ 26	14.65	7.19
8	10,000 N	33.9 ≃ 34	19.54	8.90
9	15,000 N	50.8 ≃ 51	29.31	11.04

Table 6.3: Acceleration levels for the linear and non-linear analysis based on the equivalent pedestrian number.

Vertical frequencies below 1 Hz correspond more to intentional movements, such as rhythmic bouncing or vandalism, rather than natural walking [12]. Therefore, the design concern here relates more to potential deliberate synchronization than spontaneous pedestrian activity. In such a context, the number of equivalent synchronized pedestrians becomes the relevant criterion — not the equivalent pedestrian flow. This distinction is important: if decisions regarding the installation of a TMD (tuned mass damper) were based on the linear analysis, damping might appear necessary to mitigate accelerations caused by just 5 synchronized pedestrians. However, the non-linear response shows that such acceleration levels are not reached until 9 pedestrians are synchronized, making resonance less likely under realistic conditions.

Similarly, if the fundamental mode had been within the natural walking frequency range, the non-linear results might have shown that damping was not required after all, since the comfort thresholds would not be exceeded even under typical pedestrian flows. Hence, the use of a non-linear model could significantly influence the decision of whether a damper is necessary.

6.2 Efficiency of the TMD

Three different TMD configurations were tested to evaluate the influence of non-linear behaviour in the bridge structure. A constant force of 10,000 N was applied to the deck, an amplitude previously identified as sufficient to induce significant non-linear effects. The target frequency for damping, identified through modal analysis, is 0.575 Hz. However, under a sine sweep excitation, the observed peak response frequency shifted to 0.585 Hz. The main characteristics of the tested TMD configurations are summarized in Table 6.4.

Moreover, the damping force in the non-linear analysis is defined differently compared to the linear model. In the linear model, damping is represented by a linear force, as expressed in Equation (6.19). In contrast, the non-linear model for a TMD characterizes the damping force using an exponential formulation, as shown in Equation (6.20).

$$F_{lin} = \quad c_d \cdot V \tag{6.19}$$

$$F_{nl} = \quad c_d \cdot V^{\alpha} \tag{6.20}$$

	f = 0.575 Hz - μ = 3 %	f = 0.585 Hz - μ = 3 %	f = 0.575 Hz - μ = 1 %
Number of dampers	2	2	2
m_{gen} [kg]	32,870	32,870	32,870
μ [-]	3 %	3 %	1 %
ω [rad/s]	$0.575 \cdot 2 \cdot \pi = 3.61$	$0.585 \cdot 2 \cdot \pi = 3.67$	$0.575 \cdot 2 \cdot \pi = 3.61$
ω_d [rad/s]	$0.557 \cdot 2 \cdot \pi = 3.50$	$0.567 \cdot 2 \cdot \pi = 3.56$	$0.569 \cdot 2 \cdot \pi = 3.57$
m_d [kg]	513.65	513.65	328.7
k_d [N/m]	6304.21	6525.4	4268.4
ξ_{ideal} [-]	10.6 %	10.6 %	8.4 %
c_{crit} [Ns/m]	3598.9	3661.5	2369.0
c_d [Ns/m]	381.7	388.3	201.0

Table 6.4: Characteristics of the various TMDs for the non-linear analysis

F is the damping force, c_d is the damping coefficient and V is the velocity. To compare the damping efficiency between linear and non-linear analyses, the exponential coefficient α in the non-linear damping model is set to 1. This choice effectively replicates a linear damping behaviour within the non-linear analysis. For values of $\alpha > 1$, the damping becomes more effective at higher velocities, introducing a velocity-dependent non-linearity that can significantly alter the system response.

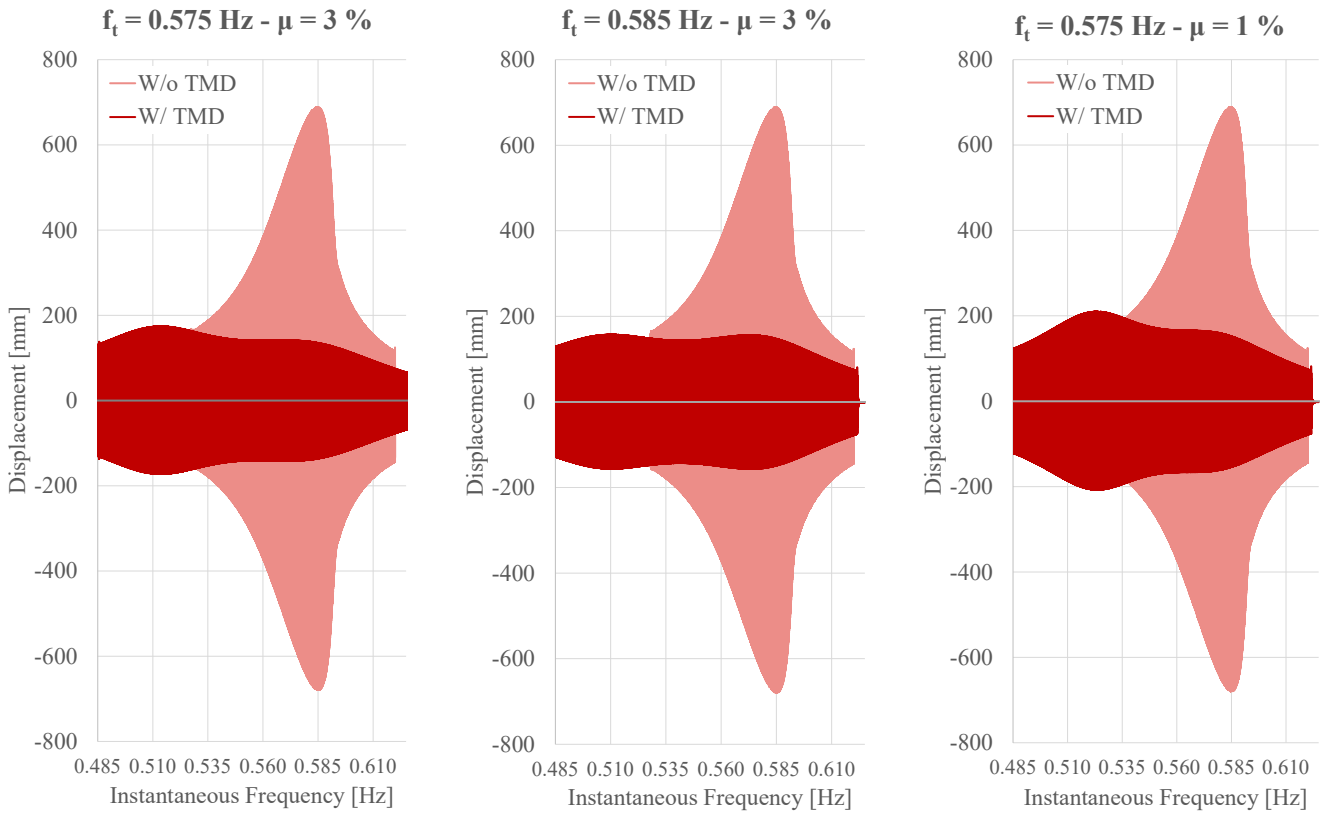

(a) f_t = 0.575 Hz - μ = 3 %. (b) f_t = 0.585 Hz - μ = 3 %. (c) f_t = 0.575 Hz - μ = 1 %.

Figure 6.16: Comparison between the response with no TMD and responses with various configuration of TMDs under a sine excitation of 10,000 N.

Figure 6.16 demonstrates that all three TMDs configurations seem to be effective at reducing the amplitude of vibrations. The damped response exhibits a typical double-peak shape, similar to the linear response previously analysed. The TMDs tuned to 0.575 Hz, shown in Figure 6.16 (a) and (c), display uneven peak amplitudes which is an indication of slight detuning. In contrast, the TMD presented in Figure 6.16 (b) does not exhibit this unevenness and shows the lowest peak amplitudes among the three damped responses. This suggests that this TMD has the most accurate tuning, by considering the frequency peak in the sine sweep response, instead of the results of the modal analysis.

However, all three TMDs are less efficient than the linear TMD in the linear analysis. While the best-performing TMD in non-linear analysis reduces vibration amplitudes to approximately 150 mm, the same reduction was achieved in the linear analysis case, but from a larger undamped amplitude of 1380 mm, compared to only 690 mm in the non-linear system. This indicates that the relative efficiency of TMDs in non-linear analysis is lower. Table 6.5 quantifies this difference, showing an average efficiency gap for the TMD of approximately 15 % between linear and non-linear analysis. The linear analysis tends to overestimate the TMD performance.

The noteworthy observations to draw from Table 6.5 are that the adjusted tuning contributes to a better efficiency of about 3 % and that the TMD with a 1 %-mass ratio achieves an efficiency of 69.5 %, compared to 74.5 % for a TMD with the same tuning frequency. The gain in efficiency is probably not worth the amount of additional material used to build the TMD. This marginal gain may not justify the increased material cost. With improved tuning, the 1 %-mass ratio TMD could potentially perform even better, making it a promising alternative to the well-tuned, but heavier, 3 %-mass ratio TMD.

	f_t = 0.575 Hz - μ = 3 %	f_t = 0.575 Hz - μ = 3 %	f_t = 0.575 Hz - μ = 3 %
Undamped amplitude [mm]	690		
Damped amplitude [mm]	174	157	210
Efficiency η	74.7 %	77.2 %	69.5 %

Table 6.5: Efficiency of the various TMDs.

Although the TMD appears to be less effective in the non-linear case, it is important to assess whether this reduced efficiency has a significant impact. Since the overall vibration amplitudes in the non-linear response are smaller, the need for damping may be less critical than initially expected based on the linear analysis. As previously noted, the TMD may not even be necessary under these conditions, particularly if the primary goal is to limit accelerations within acceptable levels. However, if greater efficiency is required—especially in reducing peak displacements, there is potential in exploring non-linear TMD designs with damping forces increasing exponentially with velocity, that could provide stronger energy dissipation. This velocity-dependent behaviour could enhance performance specifically at the peaks of displacement, where linear TMDs do not work as well. Therefore, carefully designed non-linear TMDs may offer a more effective solution for mitigating vibrations in systems exhibiting strong non-linear characteristics.

7 Conclusions and Perspectives

This thesis was initially conceived as an experimental study aimed at characterizing the dynamic behaviour of the Victor-Neels footbridge under controlled, machinery-induced excitation. The experimental campaign, based on the use of a shaker system, was designed to investigate potential non-linearities in the structure, particularly those related to damping mechanisms.

The initial plan involved a classical modal analysis to identify the bridge eigenfrequencies and mode shapes, followed by a series of sine sweep tests at varying amplitude levels to reconstruct the Frequency Response Function (FRF). Additionally, free-vibration tests were to be conducted to observe the decay of the structural response across different excitation levels, allowing for the estimation of damping ratios and the assessment of their possible amplitude dependence, a key indicator of non-linear behaviour.

However, the original thesis plan could not be executed as intended. Prolonged and time-consuming administrative exchanges with the district authority responsible for the bridge ultimately resulted in a formal refusal to authorize the test campaign, notified in mid-April. As a consequence, the focus of the thesis significantly shifted: the project evolved into a numerically driven study, complemented by a more limited experimental campaign carried out under constrained conditions. On a positive note, the delay caused by the administrative process provided additional time to further develop the numerical model. As a result, the model evolved into a detailed and robust representation of the structure, capable of supporting more advanced analyses than initially planned. This shift in focus enabled an in-depth investigation of the bridge non-linear dynamic behaviour and the effectiveness of vibration mitigation strategies such as tuned mass dampers.

The numerical model of the Victor-Neels bridge was developed in software `Finelg`. Its accuracy was assessed and improved based on the results of the experimental campaign, performed with pedestrian-induced vibrations. A modal analysis of the collected data was performed using an identification method tailored for random signals: the *SSI-COV* method (Covariance Driven Stochastic Subspace Identification method). From this analysis, mode shapes, eigenfrequencies and damping ratios were estimated, providing a reference for the numerical results. Additionally, tension measurements were taken on the hangers. This information was incorporated into the numerical model to enhance its representativeness and alignment with the actual structural conditions.

Following validation, the numerical model was used to perform static and modal analyses, which demonstrated a good correlation to the experimental modal analysis, showing an average accuracy of approximately 94 %, with accuracy increasing for higher modes. However, the comparison also highlighted a flaw in the model related to overly constrained horizontal support conditions. In the current configuration, both ends of the bridge were fully restrained against lateral displacement, resulting in excessive horizontal stiffness and overestimated eigenfrequencies. This issue could be addressed by incorporating a dilatation joint at one end of the bridge.

Prior to conducting sine sweep simulations with and without TMDs, a set of tests was carried out on the

model. They evaluated the effectiveness of the linear TMD and the influence of numerical parameters such as time step size and sweep rate on the accuracy of the numerical results. The TMD was found to be of high efficiency, as it reduces the response amplitude by approximately 90 %. Furthermore, the results showed that non-linear time-domain analyses require smaller time steps than for a linear analysis to maintain numerical stability and accuracy. To ensure steady-state conditions during sine sweeps, the sweep rate must remain below the threshold defined by $\frac{2 \cdot \xi \cdot \omega^2}{1200}$.

The objectives of this thesis were successfully met, as the non-linear analyses conducted through sine sweep and inverted sine sweep tests at varying amplitudes revealed a clear threshold for non-linear behaviour in the bridge, approximately at a load level of 5000 N. Beyond this threshold, the stiffness of the bridge significantly increases, resulting in reduced amplification ratios compared to linear ones.

Additionally, the displacement envelope shape differs between the sine sweep and inverted sine sweep tests, providing further evidence of non-linear structural behaviour. The FRFs reconstructed from these envelopes exhibited a decrease in peak amplitude, reflecting the reduction in the displacement-to-force ratio as the excitation amplitude increases. Moreover, the peak frequency shifted toward higher values, consistent with the observed increase in structural stiffness. At higher force amplitudes, the FRFs also displayed broader peaks, indicating that multiple frequencies contribute to the structural response under such excitation levels.

The linear model underestimated the actual stiffness of the bridge, resulting in displacement predictions up to 5.5 times greater than those observed in the non-linear analysis at the highest excitation amplitudes. This overestimation could lead to the unnecessary installation of TMDs, as the displacements and accelerations computed linearly may not occur in real-life conditions. It is therefore important to carefully consider the context and purpose for which a TMD is designed. In cases involving pedestrian-induced vibrations, the number of users required to reach critical acceleration levels is relatively high. However, in scenarios such as vandalism or targeted excitations, the same response levels can be triggered with significantly fewer individuals, as the excitation depends on the square root of the pedestrian flow. This highlights the need for a cautious and case-specific approach when determining the necessity and type of TMD to implement.

The efficiency of linear TMD was demonstrated to be lower in non-linear analysis, where performances dropped from a 90 % vibration amplitude reduction to 77 % vibration amplitude reduction for the best performing TMD. The importance of tuning was highlighted as well, where the efficiency could be increased by about 3 % by considering the peak frequency extracted from the non-linear sine sweep analysis, rather than the frequency from the modal analysis. Another strong point of interest was that the efficiency of a TMD with a mass ratio 3 times smaller than the original TMD was only reduced by 5 % and could be further improved by appropriate tuning.

Although the non-linear TMDs demonstrated lower efficiency compared to the linear case, this may not be a critical issue, as the displacements observed in the non-linear analysis were smaller than initially expected. It is therefore important to assess whether TMDs are necessary at all, depending on the anticipated pedestrian load and the corresponding vibration levels. Linear TMD designs remain effective and can continue to be used with confidence; however, they also present opportunities for further optimization. Reducing the TMD mass—while maintaining adequate performance—can lead to lower material consumption, resulting in both cost savings and improved environmental sustainability. Moreover, incorporating non-linear damping strategies, particularly those that are velocity-dependent, may further enhance TMD efficiency in targeted conditions. This represents a promising direction for future development aimed at more efficient and adaptive vibration mitigation solutions in suspended bridges.

In conclusion, these findings highlight the importance of carefully assessing whether installing a TMD is necessary at all, especially when considering pedestrian traffic levels or specific cases like vandalism, which can induce significant vibrations with fewer people. In the case of the Victor-Neels bridge, those applications are less problematic, as a class III footbridge with low pedestrian flux, despite the vandalism risk still being present. These conclusions are particularly relevant for Class I footbridges, which are typically located in dense urban environments and subjected to high pedestrian flows. In such contexts, accurate vibration assessments and efficient damping strategies are essential to ensure user comfort and structural performance. The same methodology could also be extended to European-style suspended footbridges, which often feature thinner and more flexible decks compared to their American or Japanese counterparts. These lighter structures are more sensitive to dynamic excitations from wind, and therefore, might benefit from refined modelling approaches that account for non-linear behaviour and optimized damping solutions.

Future optimization opportunities in the numerical model could lie in developing non-linear TMDs with velocity-dependent damping forces. Such devices can dissipate energy more effectively during peak vibrations, enabling lighter, more cost-effective, and environmentally friendly solutions that better address the complex dynamic behaviour of suspended bridges or implement active TMDs: long-term structural monitoring to track changes in the bridge dynamic properties over time. For example, cable relaxation and other factors may cause shifts in eigenfrequencies and mode shapes, which could reduce the effectiveness of TMDs designed with fixed parameters. To address this, TMD systems could be coupled with sensors that measure phase and frequency responses in real time, allowing the devices to adapt their tuning dynamically. Such active adaptive control could help maintain optimal vibration mitigation despite changes in structural stiffness, ultimately enhancing the longevity and performance of both the bridge and the damping system.

Bibliography

[1] JC. Golinval G. Kerchen. *Experimental Modal Analysis.* Centrale des Cours, Liège.

[2] V. de Ville de Goyet. *Problèmes non-linéaires en génie civil.* Greisch, Liège, 2010.

[3] E. Habtour. *Chapter 2 Analytical Methods in Nonlinear Dynamics.* 06 2022.

[4] "TJ. Ulrich". "envelope calculation from the hilbert transform". "2006".

[5] "B. Peeters". "stochastic system identification for operational modal analysis: A review". *"Journal of Dynamic Systems, Measurement, and Control"*, "2001".

[6] M. Geuzaine F. Foti and V. Denoël. On the identification of the axial force and bending stiffness of stay cables anchored to flexible supports. *Applied Mathematical Modelling*, 92, 2020.

[7] Sétra, Bagneux Cedex, France. *Passerelles piétonnes : Évaluation du comportement vibratoire sous l'action des piétons*, 2006.

[8] E. Zäll. Human-structure interaction. Master's thesis, KTH ROYAL INSTITUTE OF TECHNOLOGY SCHOOL OF ARCHITECTURE AND THE BUILT ENVIRONMENT, 2018.

[9] V.Denoël A. Mayou. Sine-sweep response of a structure equipped with a tuned-mass damper. unpublished, 2025.

[10] V.Denoël" "A. Mayou. "asymptotic analysis of multiple mode structures equipped with mulitple tuned-mass dampers". *"Journal of Sound and Vibration"*, "2022".

[11] D.J. Ewins. *Modal Testing : theory, practice and application.* Research studies press LTD, Hertfordshire, 2000.

[12] O. Brüls J.L. Croisier B. Forthomme V.Denoël C.Shwartz, A. Berger. *Experimental Study of the Human Ability to Deliberately Excite a Flexible Floor.* CRC Press, 2013.

[13] N. Roy M. Violin, E. Cavro. Sine sweep effect on specimen modal characterization. *Advances in Aircraft and Spacecraft Science*, 2018.

[14] Ji Yao, Junfeng Liu, Yujun Hu, and Qing Zhang. Optimal design and analysis of nonlinear tuned mass damper system. *Applied Sciences*, 2023.

[15] V. Denoël. *Analyse des structures II.* Centrale des Cours, Liège, 2017.